Ozone hole impacts on surface temperatures under climate change

Zur Erlangung des akademischen Grades eines
DOKTORS DER NATURWISSENSCHAFTEN (Dr. rer. nat.)
von der KIT-Fakultät für Physik des
Karlsruher Instituts für Technologie (KIT)

genehmigte

DISSERTATION

von

M. Sc. Marleen Braun
aus Landau in der Pfalz

Tag der mündlichen Prüfung:	02.07.2021
Referent:	Prof. Dr. Peter Braesicke
Korreferent:	PD Dr. Michael Höpfner

Abstract

The Antarctic ozone hole, caused by human releases of chlorofluorocarbons, plays a major role in driving climate change in the southern hemisphere. Atmospheric temperatures and circulation are affected by the severe ozone loss due to a coupling of atmospheric composition, radiation, and dynamics. The ozone hole leads to a springtime stratospheric cooling and a prolonged persistence of the stratospheric polar vortex. Further, it affects surface climate where changes are characterized by a shift of the midlatitude jet towards higher latitudes that is commonly referred to as a shift of the Southern Annular Mode (SAM) towards its positive phase. This shift is associated with warming and cooling patterns in the southern hemisphere, particularly a cooling of large parts of Antarctica and a warming of the Antarctic Peninsula and Patagonia.

With stratospheric ozone in the path to recovery, the climate impacts associated with the ozone hole are expected to reverse in the future. The concentration of greenhouse gases will, however, continue to increase. Similarly to the ozone hole, rising greenhouse gas concentrations are associated with a shift of the SAM towards its positive phase. Thus the effects of increased greenhouse gases and ozone recovery are predicted to counteract in the future. For meaningful climate projections, a detailed characterization of ozone hole induced climate change signals is, therefore, essential. However, a precise attribution of climate change signals to the Antarctic ozone hole is complicated due to simultaneous atmospheric composition changes and natural climate variability. In this thesis, idealized timeslice simulations were performed with the ICOsahedral Non-hydrostatic model with Aerosols and Reactive Trace gases (ICON-ART) to investigate ozone hole induced climate change signals isolated from other perturbations of the climate system. Further, the impact of natural climate variability is assessed. Our model results show robust summertime near-surface temperature changes caused by the ozone hole that are characterized by more complex warming and cooling patterns than previous studies suggest. While those studies attributed a large fraction of the detected signal to a shift in the SAM, the ICON-ART results indicate near-surface temperature changes that are not entirely caused by changes of the SAM. The decreased impact of the SAM in the ICON-ART model could result from a weaker, more realistic response of the SAM to external forcing that is commonly overestimated in other chemistry-climate models. Analysis of the SAMs variability shows more persistent SAM anomalies due to the ozone hole and a decreased persistence for future climate. As persistent stratospheric SAM anomalies have a potential impact on tropospheric SAM characteristics and thus near surface meteorology, a prediction metric was calculated to investigate the skill of SAM anomalies at different altitudes in predicting the averaged near-surface SAM one month in advance. Our calculations show that there is a strong decrease in stratospheric predictability for future simulations, regardless of the ozone recovery. The decreased stratospheric influence on the tropospheric SAM will likely affect the quality of extended range weather forecasts in the future.

Contents

1 Introduction

Stratospheric ozone plays an important role in the Earth's atmosphere. As a strong absorber of incoming solar radiation, it determines the thermal structure of the atmosphere and shields the surface from ultraviolet radiation that is harmful to life on Earth. Since the early 1980s, anthropogenic emissions of ozone-depleting substances have led to severe ozone depletion in the Antarctic spring stratosphere - the Antarctic ozone hole. This decrease in ozone concentrations results in an increase in ultraviolet radiation reaching the surface and can affect human health and natural ecosystems (e.g. van der Leun et al., 1998).

Additionally, changes in ozone interact with the climate system and influence atmospheric temperatures and circulation (e.g. Braesicke et al., 2013). The reduced ozone concentrations lead to a decreased temperatures in the springtime polar stratosphere, and thus a prolonged persistence of the polar vortex. The stratospheric circulation changes are coupled to the troposphere and affect southern hemisphere tropospheric circulation and surface climate as well (e.g. Previdi and Polvani, 2014). Circulation changes in the troposphere are characterized by a poleward shift of the midlatitude jet, corresponding with a trend towards the positive phase of the Southern Annular Mode (SAM), which is the leading mode of variability of the SH extratropical circulation (Thompson and Wallace, 2000). It is characterized by approximately zonally symmetric alterations of atmospheric pressure between mid and high latitudes. The positive phase of the SAM is associated with characteristic temperature anomalies for large parts of the southern hemisphere. Due to its influence on the SAM, polar stratospheric ozone depletion plays a major role in driving climate change in the southern hemisphere (Li et al., 2016).

Ozone-depleting substances are decreasing in the atmosphere, following the implementation of the Montreal protocol (Montreal Protocol, 1987). With this decrease, stratospheric ozone is expected to recover until the mid-21st century (e.g. Karpechko et al., 2010). With the recovery of stratospheric ozone, a reversal of its associated climate impacts is expected (e.g. Son et al., 2009).

Atmospheric composition changes are not limited to the emission of ozone-depleting substances but are also strongly affected by anthropogenic emission of greenhouse gases (e.g. Müller, 2012). Increased greenhouse gases influence surface climate and, like polar ozone depletion, are associated with a trend towards the positive phase of the SAM (e.g. Karpechko et al., 2010). While the concentration of greenhouse gases in the atmosphere

will continue to increase in the future, stratospheric ozone is expected to recover until the mid-21st century. Consequently, the effects of increased greenhouse gases and ozone recovery will be counteracting, with greenhouse gases continuing to shift the SAM towards its positive phase and ozone recovery leading to negative SAM trends (e.g. Arblaster et al., 2011). Therefore a detailed characterization of ozone hole induced climate change signals is important for meaningful future climate projections.

Even though it is now widely accepted that the Antarctic ozone hole has influenced the surface climate of the southern hemisphere, estimating the strength of the impact as well as its seasonal evolution, particularly at the surface, remains challenging. Concentrations of ozone-depleting substances and greenhouse gases change simultaneously, and thus observed climate change signals cannot be attributed to the chemistry-climate interactions of ozone depletion alone. Further, atmospheric circulation shows a natural year-to-year variability that additionally complicates the isolation of ozone affected climate change signals in observations (e.g. Shindell, 2004).

Chemistry-climate modeling offers the possibility to investigate the interaction of past and future atmospheric composition changes with temperature and circulation changes and their influence on surface climate. Idealized experimental setups further allow to isolate ozone induced climate change signals from other perturbations of the climate system. Further, to establish a causal link between stratospheric ozone changes and tropospheric climate changes, large ensemble simulations are required to exclude the effects of internal variability (Canziani et al., 2014).

A correct representation of the internal variability of the SAM in climate models is particularly important, as it can influence the model system's response to external forcings (e.g. Kim and Reichler, 2016). A shorter than observed persistence of the state of the SAM could result in a weaker response of the system to ozone changes, while a longer persistence could overestimate the climate feedbacks.

In this work, model experiments are designed and performed to investigate the ozone hole induced climate change signals from the stratosphere to the troposphere, separated from other perturbations of the climate system. The experimental design allows for a detailed analysis of internal variability. This includes estimates of model uncertainties, the robustness of climate change signals, and a detailed analysis of the model's representation of atmospheric variability patterns. In addition to the effects induced by ozone changes, climate change signals caused by increasing greenhouse gases and the interactions of greenhouse gas changes and ozone recovery are analyzed.

After providing the theoretical background of the thesis in Chapter 2, a description of the ICON-ART model and the experimental setup is given in the following chapter. Chapter 4 introduces the methods used to analyze significance, uncertainties, and internal variability. In the following chapter, the model's ability to represent climatological ozone distributions is evaluated. Chapter 6 focuses on the analysis of southern hemispheric

climate change signals induced by changes in GHGs and ozone depletion and recovery. In chapter 7, the model's representation of atmospheric variability patterns and their response to climate change are investigated. Finally, in chapter 8, a summary and outlook are provided.

2 Theoretical Background

2.1 Structure of the atmosphere

The Earth's atmosphere can be divided into several vertical layers that are characterized by the mean vertical temperature profile (Figure 2.1).

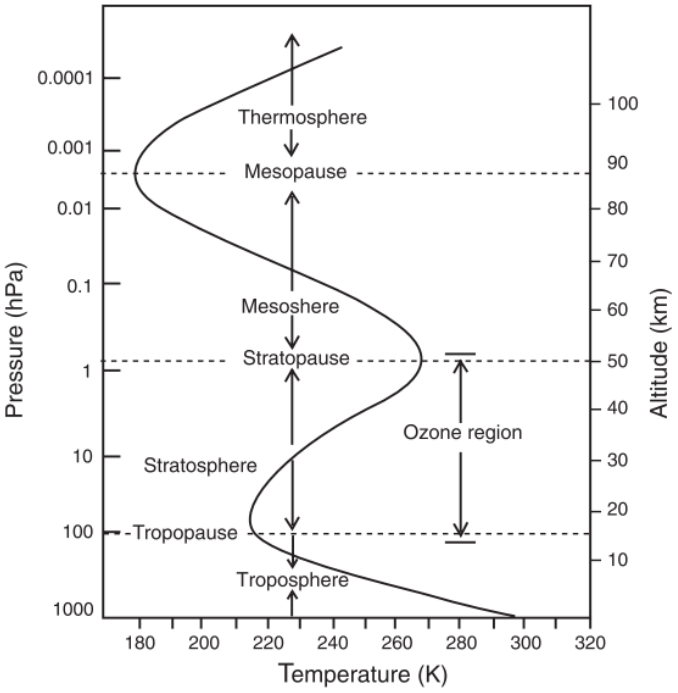

Figure 2.1: Vertical layers of the atmosphere characterized by the temperature profile as a function of pressure (left axis) and approximate altitude (right axis). (Mohanakumar, 2008).

The lowest layer, the troposphere, is characterized by decreasing temperature with altitude. It accounts for about 85 % of the atmospheric mass. Further, virtually all atmospheric water vapor is trapped in the troposphere. Therefore, weather and climate variability are largely governed by tropospheric processes and changes. However, changes in the layer above, the stratosphere, can affect the troposphere by radiative and dynamical interactions. The troposphere is separated from the stratosphere by the tropopause that is typically located at altitudes between 10 and 16 km, depending on latitude and season.
The stratosphere reaches from the tropopause to about 50 km altitude. In this layer, temperatures are increasing with height resulting in large static stability. This inversion inhibits vertical mixing with the troposphere. The stratospheric temperature emerges from the abundance of ozone and its absorption of solar ultraviolet radiation.

Above the stratopause, in the mesosphere, the temperature decreases due to reduced solar heating by ozone. In the thermosphere, an increase in temperature is visible that is caused by the absorption of incoming solar radiation mainly by molecular oxygen.
The vertical temperature profiles differ with latitude and season. Therefore, the climatological meridional distribution of zonal mean temperatures for southern hemispheric winter is shown in Figure 2.2. The climatological meridional distribution of zonal mean zonal wind for southern hemispheric winter is given in Figure 2.3. As this study focuses on the southern hemisphere, the designation of seasons in the following refers to the southern hemisphere unless otherwise stated.

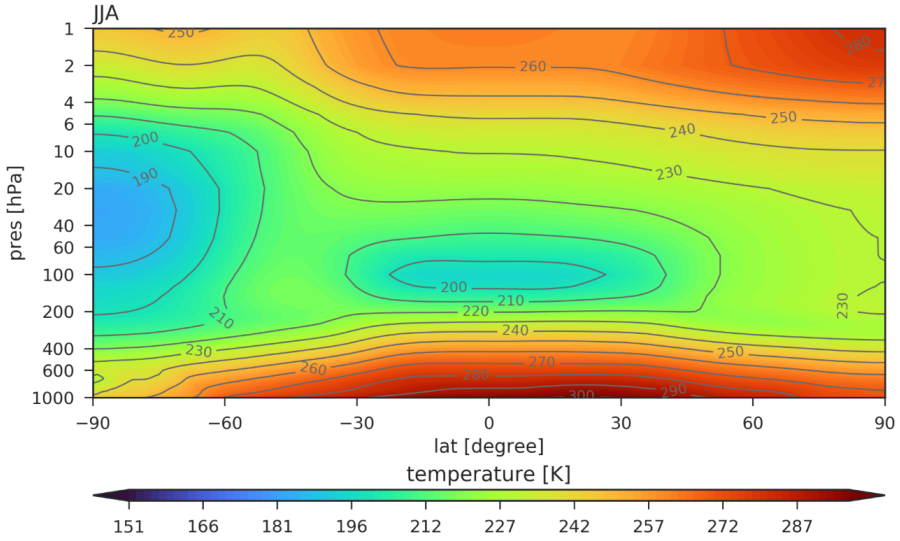

Figure 2.2: Zonal mean temperature climatology (1979 - 2019) for southern hemisphere winter (June - August) derived from the ERA5 reanalysis.

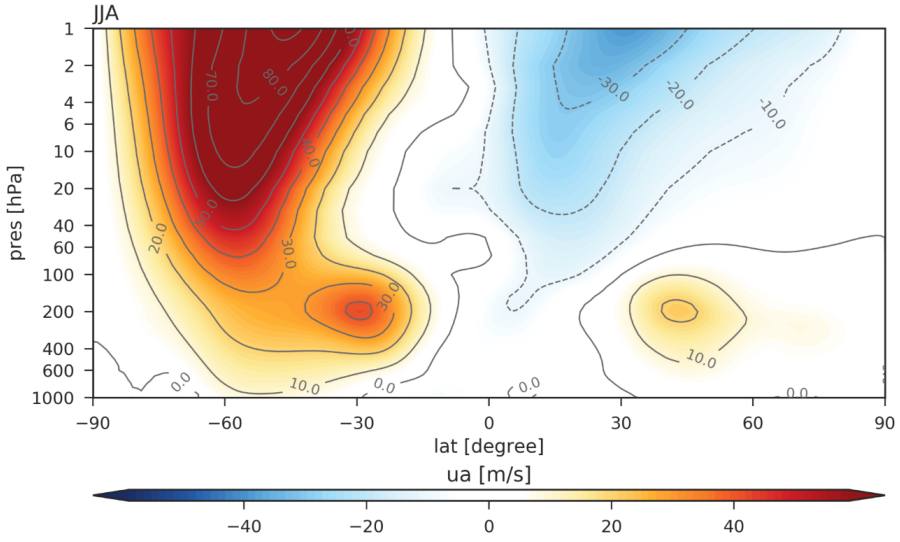

Figure 2.3: Zonal mean zonal wind climatology (1979 - 2019) for southern hemisphere winter (June - August) derived from the ERA5 reanalysis.

At the tropical tropopause, a temperature minimum is present. A temperature maximum is visible at the summer pole and the midlatitudes of the winter hemisphere in the lower stratosphere. Further, a temperature minimum is observed at the winter pole resulting from the absence of incoming solar radiation. In the upper stratosphere, above approximately 30 hPa, the temperature decreases from winter to the summer pole, consistent with the radiative equilibrium.
The wind climatology is consistent with the observed temperature climatology according to the thermal wind balance. The winter hemisphere is characterized by a strong westerly jet in the stratosphere, referred to as polar night jet or polar vortex, and a weaker westerly jet in the troposphere.
The vortex starts to develop in autumn with the beginning of the absence of sunlight and strengthens throughout the winter. The absence of incoming solar radiation leads to a thermal cooling of the air at high latitudes and results in very low temperatures in the winter polar regions. As a result, an increased temperature gradient between the pole and the equator is observed. Due to the temperature difference, strong westerly winds develop. This dynamical structure inhibits mixing from the midlatitudes and isolates the air inside the vortex. The polar vortex decays from late winter to spring when the temperature gradients become less strong. In summer, weaker easterly winds are present.
Large differences can be observed between the Arctic and Antarctic polar vortex. The Antarctic vortex is larger, stronger, and persists longer than the northern polar vortex. These differences are caused by stronger wave activity in the northern hemisphere due to differences in topography and land-sea distribution.
A more detailed description of the atmospheric structure and circulation is given by e.g. Holton (2004) and Andrews et al. (1987).

2.2 Stratospheric ozone

The stratospheric ozone layer was first discovered in the 1920s. Its existence originates mainly from photochemical reactions as proposed by Chapman (1930). The predominant part of atmospheric ozone is situated in a layer between 15 and 30 km altitude with a maximum volume mixing ratio at about 25 km altitude (e.g. Dameris et al., 2007).
According to Chapman, atmospheric O_2 is photolyzed by sunlight with a wavelength less than $\lambda < 240$ nm resulting in two radicals. Those radicals are rapidly combining with O_2 to form ozone [R1].

$$O_2 + h\nu \longrightarrow 2\,O \qquad (\lambda{<}240\,\text{nm}) \qquad \text{[R 1a]}$$

$$O + O_2 + M \longrightarrow O_3 + M^* \qquad \text{[R 1b]}$$

where M is a third body.

The produced ozone molecules are photolyzed by lower-energy photons with wavelengths less than $\lambda < 320\,\text{nm}$. The lower energy is sufficient as the bonds in the ozone molecule are weaker than those in the oxygen molecule. The produced oxygen atoms react with ozone resulting in a competing ozone loss [R2].

$$O_3 + h\nu \longrightarrow O_2 + O \qquad (\lambda{<}320\,\text{nm}) \qquad \text{[R 2a]}$$

$$O_3 + O \longrightarrow 2\,O_2 \qquad \text{[R 2b]}$$

Consequently, a photochemical steady-state develops between the ozone formation and loss reactions of the Chapman cycle. This explains the observed vertical profile of ozone concentration with a maximum at 25 km. Above 35 km, the formation of ozone is limited by low O_2 concentrations. At altitudes below 20 km, the number of photons that can photolyze O_2 is small. In addition to the photolytic destruction of ozone, the presence of hydrogen oxides, nitrogen oxides, or halogens enables the destruction of ozone in catalytic cycles. Especially catalytic cycles associated with halogens are very effective. Here, chlorofluorocarbons (CFCs) are particularly important, as they are not soluble in water and can solely be removed from the atmosphere by photolysis. The photolysis of CFCs releases chlorine radicals that are potentially initiating catalytic cycles [R3].

$$Cl + O_3 \longrightarrow ClO + O_2 \qquad \text{[R 3a]}$$

$$ClO + O \longrightarrow Cl + O_2 \qquad \text{[R 3b]}$$

$$\text{Net:} \quad O_3 + O \longrightarrow 2\,O_2 \qquad \text{[R 3c]}$$

Due to anthropogenic emissions and thus an increase in the concentration of CFCs, ozone destruction was observed globally. Because of the long lifetimes of CFCs the ozone loss will last for several decades. Molina and Rowland (1974) warned that a continuing increase of CFCs could be a serious threat to the ozone layer.

Besides the globally observed ozone loss, Farman et al. (1985) discovered the so-called ozone hole in 1985. They documented a strong springtime ozone loss limited to southern polar latitudes that occurred in altitudes between 12 and 25 km. This ozone loss cannot be explained by the processes described above. However, the strong ozone loss was found to be connected to the occurrence of polar stratospheric clouds (PSCs) and regions with highly enhanced ClO values (Solomon et al., 1986). As a consequence of the observed strong ozone depletion, the production of ozone-depleting substances was regulated by the Montreal Protocol (Montreal Protocol, 1987).

Considering the observed high ClO concentration, additional catalytic cycles activating chlorine and bromine reservoirs as proposed by Molina and Molina (1987) [R4] and McElroy et al. (1986) [R 5] are effective and result in enhanced ozone losses.

$$\mathrm{ClO + ClO + M \longrightarrow Cl_2O_2 + M^*} \quad \text{[R 4a]}$$

$$\mathrm{Cl_2O_2 + h\nu \longrightarrow ClOO + Cl} \quad \text{[R 4b]}$$

$$\mathrm{ClOO + M \longrightarrow Cl + O_2 + M^*} \quad \text{[R 4c]}$$

$$\mathrm{(2\,x)\quad Cl + O_3 \longrightarrow ClO + O_2} \quad \text{[R 4d]}$$

$$\mathrm{Net:\quad 2\,O_3 \longrightarrow 3\,O_2} \quad \text{[R 4e]}$$

$$\mathrm{Cl + O_3 \longrightarrow ClO + O_2} \quad \text{[R 5a]}$$

$$\mathrm{Br + O_3 \longrightarrow BrO + O_2} \quad \text{[R 5b]}$$

$$\mathrm{BrO + ClO \longrightarrow Br + Cl + O_2} \quad \text{[R 5c]}$$

$$\mathrm{Net:\quad 2\,O_3 \longrightarrow 3\,O_2} \quad \text{[R 5d]}$$

However, the high ClO concentrations observed over Antarctica cannot be explained by gas-phase chemistry alone but are associated with heterogeneous reactions on the surface of PSCs.

The cold stratospheric temperatures (< 195 K) during polar night enable the formation of PSCs. On the surface of those PSCs, heterogeneous processes occur that activate the reservoir species HCl and $ClONO_2$ [R 6].

$$\mathrm{ClONO_2 + HCl \xrightarrow{het} Cl_2 + HNO_3} \quad \text{[R 6a]}$$

These reactions result in the formation of chlorine molecules that are photolyzed once sunlight returns, thus forming reactive Cl. This increase in reactive chlorine then results in increased ozone depletion.

In addition to the activation of chlorine reservoirs, PSCs can further influence ozone depletion by the uptake of HNO_3 and the sedimentation of HNO_3 containing particles. Photolysis of gaseous HNO_3 can release nitrogen oxides that are involved in the formation of chlorine reservoirs [R 7].

$$\mathrm{HNO_3 + h\nu \longrightarrow OH + NO_2} \quad \text{[R 7a]}$$

$$\mathrm{NO_2 + ClO + M \longrightarrow ClONO_2 + M^*} \quad \text{[R 7b]}$$

Consequently, a low concentration of gaseous HNO_3 inhibits the formation of chlorine reservoirs and thus results in stronger and prolonged ozone depletion.

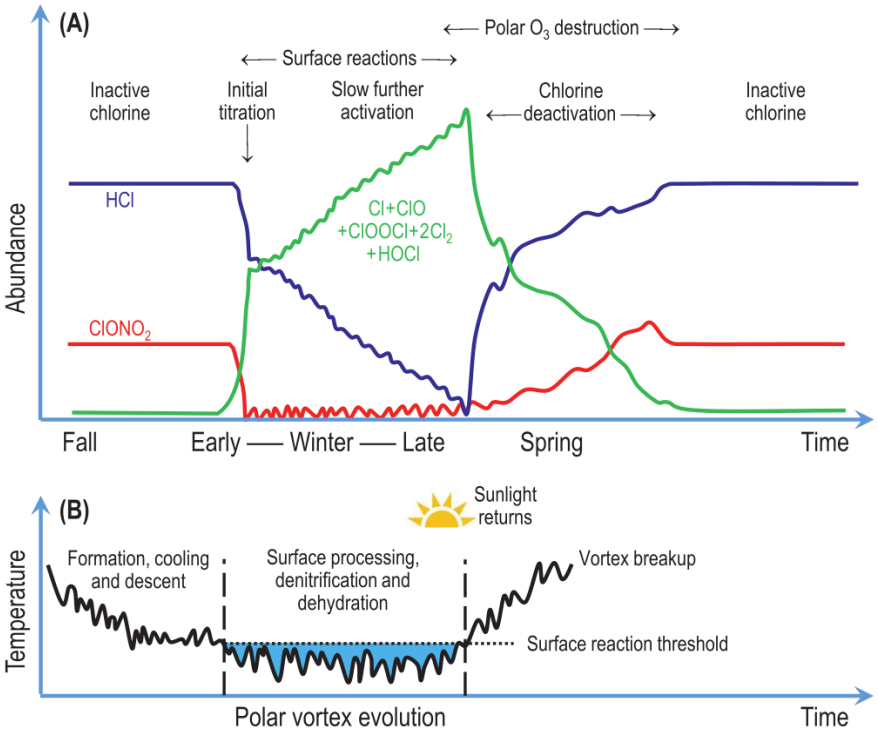

Figure 2.4: Temporal evolution of processes involved in the formation of the Antarctic ozone hole (Tritscher et al., 2021).

An overview of the temporal evolution of the processes involved in the formation of the ozone hole is given in Figure 2.4. A more detailed description of the processes involved in stratospheric ozone depletion can be found in Solomon (1999).

2.3 Climate system response to ozone depletion and recovery

Stratospheric ozone is a strong absorber of incoming solar radiation. Therefore, changes in the abundance of ozone lead to changes in the local radiative balance and thus to changes in temperatures and circulation in spring. Consequently, Antarctic ozone depletion results in decreased temperatures in the polar stratosphere. This temperature decrease changes the meridional temperature gradient in the stratosphere and leads to changes in circulation. Those circulation changes are characterized by a strengthened and prolonged stratospheric polar vortex, consistent with thermal wind balance. Further, circulation changes are observed down to the surface, where they are characterized by a poleward shift of the midlatitude jet. These tropospheric circulation changes are commonly referred to as a shift of the tropospheric SAM towards its positive phase (e.g. Thompson et al., 2011).

The SAM is the leading mode of variability of the southern hemisphere extratropical circulation (Thompson and Wallace, 2000). It is characterized by approximately zonally symmetric alterations of atmospheric pressure between mid and high latitudes and thus describes a seesaw of atmospheric mass. The SAM can be described throughout the atmosphere and can be used as a proxy for the variability of the jets. In the troposphere, the positive phase of the SAM is associated with a poleward shift of the midlatitude jet. In the stratosphere, the positive phase of the SAM is indicating a strengthening of the polar night jet (e.g. Previdi and Polvani, 2014).

Stratospheric changes can influence the troposphere through radiative and dynamical interactions. The stratospheric cooling leads to a reduction of downwelling longwave radiation and thus cools the polar troposphere. This cooling increases the meridional temperature gradient in the troposphere and therefore affects the tropospheric circulation (Grise et al., 2009). Further, the stratosphere and troposphere are dynamically coupled. The strengthening of the polar night jet changes the condition for the propagation of planetary waves and thus the amplitude and location of wave-breaking in the stratosphere. These changes influence atmospheric vertical motion that extend down to the surface. The induced changes in vertical motion can then affect tropospheric temperature gradients through adiabatic expansion and compression. This mechanism is typically referred to as "downward control" (e.g. Haynes et al., 1991; Song and Robinson, 2004). While the tropospheric jet shift is commonly detected in observations and modeling studies, the stratosphere-troposphere coupling mechanisms causing this behavior are not yet fully understood. A more detailed description of the mechanisms likely involved in the coupling is given by Kidston et al. (2015) and Thompson et al. (2011).

The shift of the tropospheric midlatitude jet is resulting in surface temperature changes as well. This shift of the jet is associated with an enhanced temperature gradient between Antarctica and the midlatitudes, and thus, a cooling of Antarctica and a warming of its surroundings (Previdi and Polvani, 2014). A positive SAM index is further associated with a warming of southern South America (Holz et al., 2017), southern Africa (Manatsa et al., 2013), and New Zealand (Renwick and Thompson, 2006) and a cooling of central and eastern subtropical Australia (Hendon et al., 2007). A more detailed overview of climate impacts associated with the positive phase of the SAM is given by Fogt and Marshall (2020). Consequently, while Antarctic ozone depletion is limited to the polar stratosphere, its associated climate impacts affect the entire southern hemisphere.

Stratospheric ozone is expected to recover during the next decades due to the decline in ozone-depleting substances (ODSs). Thus, the climate change signals associated with polar ozone depletion are likely to reverse in the future. Atmospheric composition changes are highly influenced by an increase in GHGs that is cooling the stratosphere. Climate change signals induced by GHG changes also include a shift of the tropospheric SAM towards its positive polarity. Thus the effects of ozone recovery and increasing GHGs will

be counteracting in the future. Therefore, it is essential to realistically capture the magnitude of the expected changes to provide meaningful climate projections, particularly for the southern hemisphere.

3 Model and experimental setup

3.1 The ICON model

The ICOsahedral Non-hydrostatic (ICON) modeling framework is a modeling system designed for unified, seamless modeling across scales and was jointly developed by the German Weather Service and the Max-Planck-Institute for Meteorology. It is highly flexible and allows for applications of large-eddy simulations (Dipankar et al., 2015), numerical weather prediction (Zängl et al., 2015) and climate modeling (Giorgetta et al., 2018). This flexibility is achieved by the development of a dynamical core based on non-hydrostatic equations with local mass conservation (Zängl et al., 2015).

ICON operates on an unstructured horizontal grid, namely an icosahedral-triangular C grid (e.g. Staniforth and Thuburn, 2012). This grid type is well suited for the simulation of polar regions as it overcomes the singularity problem that arises when using e.g. latitude-longitude-grids. The grid is based on an icosahedron consisting of 20 triangles that are successively refined to obtain the desired grid resolution. In the first step, the root division (Rn), the triangle edges are divided into n equal parts. New triangles are constructed by the connection of the division points. The resulting triangles are refined by a bisection division (Bk). The grid is additionally optimized by spring dynamics (Tomita et al., 2001) to achieve an optimal configuration.

With this refinement technique, the total number of grid cells can be computed as follows.

$$n_c = 20n^2 4^k \tag{3.1}$$

The effective grid resolution $\overline{\Delta x}$ is defined as

$$\overline{\Delta x} = \sqrt{\overline{a_c}} = \sqrt{\frac{\pi}{5}} \frac{r_e}{n2^k} \tag{3.2}$$

where $\overline{a_c}$ is the average cell area and r_e is the radius of the earth.

In this study, the R2B4 grid is used for all simulations. The characteristics of this grid are summarized in Table 3.1.

Vertically, ICON uses the terrain following SLEVE (smooth level vertical) coordinate system based on Schär et al. (2002) and Leuenberger et al. (2010). For the ICON climate configuration used in this study, 47 vertical levels up to about 75 km are used. The altitude

Table 3.1: ICON horizontal grid characteristics

grid name	n_{cell}	$\overline{\Delta x}$ [km]	$\overline{a_c}$ [km^2]
R2B4	20480	157.82	24907.28

of the 30 lowest levels at a latitude of 72°S is depicted together with the horizontal R2B4 grid for the southern hemisphere in Fig. 3.1.

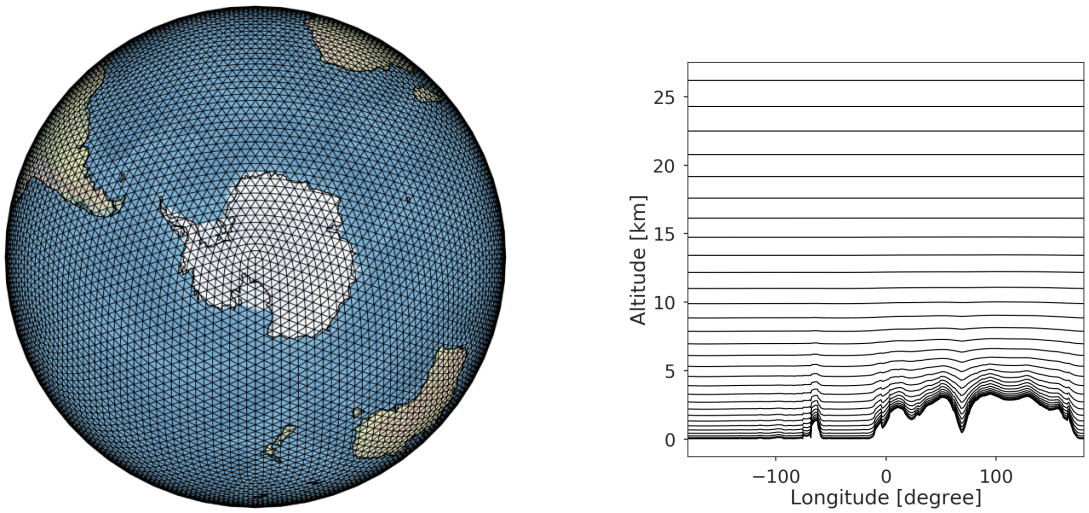

Figure 3.1: Horizontal R2B4 grid for the southern hemisphere and altitude of the 30 lowest vertical levels at a latitude of 72°S.

The dynamical core solves the fluid and thermodynamic equations and is based on Gassmann and Herzog (2008). It consists of a non-hydrostatic formulation and Reynolds-averaged Navier-Stokes equations. This set of basic equations reads as follows:

$$\frac{\partial v_n}{\partial t} + \frac{\partial K_h}{\partial n} + (\zeta + f)v_t + w\frac{\partial v_n}{\partial z} = -c_{pd}\theta_v \frac{\partial \pi}{\partial n} + F(v_n) \tag{3.3}$$

$$\frac{\partial w}{\partial t} + \mathrm{v}_h \cdot \nabla w + w\frac{\partial w}{\partial z} = -c_{pd}\theta_v \frac{\partial \pi}{\partial z} - g \tag{3.4}$$

$$\frac{\partial \rho}{\partial t} + \nabla \cdot (\mathrm{v}\rho) = 0 \tag{3.5}$$

$$\frac{\partial \pi}{\partial t} + \frac{R_d}{c_{vd}}\frac{\pi}{\rho\theta_v}\nabla \cdot (\mathrm{v}\rho\theta_v) = Q \tag{3.6}$$

with π as Exner function:

$$\pi = \left(\frac{R_d}{p_{00}}\rho\theta_v\right)^{\frac{R_d}{c_{vd}}} \tag{3.7}$$

where t is time, z is geometric height, ρ is the air density, θ_v is the virtual potential temperature, and ζ is the vertical vorticity component. v_n denotes the horizontal wind

perpendicular to the triangle edge, v_t is the horizontal wind tangential to the triangle edge, and w is used for the vertical wind. The index h indicates the horizontal component so that K_h denotes the horizontal kinetic energy. c_{vd} and c_{pd} are the specific heat capacities for dry air for constant volume and pressure, respectively. R_d is the gas constant of dry air, g is the gravitational acceleration, f is the Coriolis parameter and $p_{00} = 1000\,\text{hPa}$ is a reference pressure. F and Q are the external source and sink terms that are subject to the physics parameterization. F denotes the source and sink term for momentum, and Q is the diabatic heating that is source and sink term for temperature. A detailed description of the ICON dynamical core can be found in Zängl et al. (2015).

Even though the ICON model is highly flexible and can be used for various applications, different model resolutions and time scales require different physics parameterizations. While some processes are directly resolved for effective resolutions of $\overline{\Delta x} = 100\,\text{m}$, they are not explicitly resolved for $\overline{\Delta x} = 100\,\text{km}$ and need to be parameterized completely. Therefore different physics parameterizations can be chosen in ICON. In this study, we work with the climate physics configuration described by Giorgetta et al. (2018).

3.2 The ART extension

The ICON model is complemented by the Aerosols and Reactive Trace gases (ART) module, developed at the Karlsruhe Institute of Technology. The ART module is specifically designed for the flexible modeling of the interaction between atmospheric chemistry, dynamics, and radiation (Rieger et al., 2015; Schröter et al., 2018). The combined ICON-ART model is therefore well suited for the simulation of interactions between atmospheric composition and circulation. The ART module offers the opportunity to work with different chemistry modes depending on the desired application. In this study, a lifetime-based chemistry where tracers are depleted by a constant lifetime (e.g. Rieger et al., 2015) is used that is complemented by a linearized ozone scheme. Other options are a simplified steady-state OH chemistry (Weimer et al., 2017) or gas-phase chemistry (Schröter et al., 2018).

The simplified linearized ozone (Linoz) scheme used is based on McLinden et al. (2000). Photochemical ozone tendencies are calculated by a first-order Taylor expansion considering local ozone mixing ratio, temperature, and the overhead ozone column density. The expansion is performed over a set of climatological values available for each month at 25 heights from 10 and 58 km and latitudes between 85°S and 85°N. Below 10 km, no climatological ozone values are available and a constant tropospheric lifetime is assumed. According to Young et al. (2013) ozone has a tropospheric lifetime of 22.3 days, while Ehhalt et al. (2001) identified a lifetime between 3.65 and 18.25 days. In this study, a tropospheric lifetime of 20 days is implemented as the default lifetime. In addition,

tropospheric lifetimes of 10 and 30 days were implemented to test the sensitivity of tropospheric ozone.

The change of ozone concentration with time due to the local chemistry is given by:

$$\frac{\partial \xi}{\partial t} = (P-L)^0 + \left.\frac{\partial (P-L)}{\partial \xi}\right|_0 (\xi - \xi^0) + \left.\frac{\partial (P-L)}{\partial T}\right|_0 (T - T^0) + \left.\frac{\partial (P-L)}{\partial c_{O_3}}\right|_0 (c_{O_3} - c^0_{O_3}) \tag{3.8}$$

where $(P-L)$ is the ozone tendency (production and loss term), ξ denotes the ozone volume mixing ratio, T is the temperature and c_{O_3} denotes the overhead ozone column. Climatological values are denoted by the superscript "^{0}". The subscript "$_0$" denotes partial derivatives with evaluation at the climatological value.

An additional loss term was added to the scheme to account for polar ozone chemistry. Following Sinnhuber et al. (2003) a ten-day chemical lifetime of ozone (τ_{PSC}) in the presence of polar stratospheric clouds (T < 195 K: threshold temperature for the formation of NAT particles) and the availability of sunlight (solar zenith angle $\vartheta < 90°$) was implemented. This solar zenith angle (SZA) threshold was determined as a result of a sensitivity study, evaluating the optimal SZA threshold for a realistic representation of the Antarctic ozone hole, which is described in section 5.1.

$$\begin{aligned}\frac{\partial \xi}{\partial t} =& (P-L)^0 + \left.\frac{\partial (P-L)}{\partial \xi}\right|_0 (\xi - \xi^0) + \left.\frac{\partial (P-L)}{\partial T}\right|_0 (T - T^0) \\ &+ \left.\frac{\partial (P-L)}{\partial c_{O_3}}\right|_0 (c_{O_3} - c^0_{O_3}) - \frac{1}{\tau_{PSC}} \cdot \xi\end{aligned} \tag{3.9}$$

with

$$\tau_{PSC} = \begin{cases} 10 \text{ days} & \text{for } \vartheta < 90° \text{ and T} < 195\text{K} \\ \infty \text{ days} & \text{else} \end{cases} \tag{3.10}$$

where ϑ denotes the solar zenith angle and T denotes temperature.

The calculation is performed at each time step at each grid point with climatological values interpolated to the grid points' latitude and altitude.

While the Linoz scheme allows for an interactive calculation of ozone, a few shortcomings arise due to the simplicity of the tendency formulation, which should be kept in mind when interpreting climate simulations. The Linoz scheme works with a climatology that is used for linearization. This climatology is obtained from the atmospheric conditions for the year 2000. Further, the polar ozone lifetime implemented in the model was optimized for conditions of the year 2000 as well and represents ozone-depleting substance (ODS) conditions for 2000. Thus, changes in ODS are not represented explicitly by the model,

making transient climate change simulations difficult. However, a representation of different ODS conditions in the Linoz scheme could be achieved by updated background climatologies and changes in τ_{PSC}.

3.3 Ozone in model simulations

To investigate ozone hole-induced climate change signals, a realistic ozone representation in the model experiments is essential. The most realistic ozone representation used in climate models is a comprehensive and fully interactive ozone calculation, thus enabling direct interaction between ozone concentrations, radiation, and dynamics. However, modeling all essential chemical reactions is computationally expensive. When performing multi-decadal climate simulations, only a certain complexity is feasible concerning the chosen grid resolution, model time-stepping, and the chemistry representation. In climate modeling, ozone is therefore often prescribed with a monthly mean, zonal mean climatology that is used to calculate radiative tendencies. Studies investigating the impact of an interactive ozone calculation compared to zonally mean, monthly mean ozone climatologies, however, indicate a significant influence of the ozone representation on the model climate.

Comparing simulations with prescribed and interactive ozone calculations, Sassi et al. (2005) found colder stratospheric temperatures in the Antarctic lower stratosphere during spring for the interactive simulations. This finding is confirmed by Waugh et al. (2009) and results in an underestimation of Antarctic stratospheric springtime temperature trends when prescribing zonal-mean ozone. Also, the influence of stratospheric ozone changes on the tropospheric circulation is underestimated in those simulations. Further, Li et al. (2016) suggested that the interactive representation of ozone is not only affecting the southern atmosphere but also the Southern Ocean and Antarctic sea ice.

Crook et al. (2008) and Gillett et al. (2009) reported that the neglection of asymmetries in the prescribed ozone climatology can result in biases in the models' climate response, while Neely et al. (2014) showed that rapid temporal changes in ozone concentrations are not sufficiently represented in monthly mean climatologies. Those studies indicate that prescribed ozone fields with a higher spatial and temporal resolution could improve the model performance. Nevertheless, Nowack et al. (2015) and Haase and Matthes (2019) presented indications for a smaller but still significant difference between a fully interactive ozone representation and calculations with prescribed three-dimensional ozone fields.

The studies by Chiodo and Polvani (2017) and Nowack et al. (2015) investigated the response of interactive ozone calculations to an external forcing of an abrupt $4 \times \mathrm{CO}_2$ increase. The results show a damping of surface climate change signals and the response of the midlatitude jet of around 20 % when interactive ozone was included. Those studies

underline the importance of an interactive flow-consistent ozone calculation for climate simulations.

Using the Linoz scheme in our model experiments offers the possibility for interactive simulations where ozone can feedback on temperature and circulation but is still computationally feasible for multi-decadal climate simulations. In chapter 5 the model's performance considering the realistic representation of ozone is investigated with a focus on ozone hole characteristics.

3.4 Experimental design

In this study, we investigate the results of 5 different model experiments conducted with the climate configuration of the ICON-ART modeling framework. Each experiment was simulated in a timeslice setup for a total of 70 years. The first five years are regarded as a spin-up period and are neglected in the analysis of the simulations. The experiments were performed with a global R2B4 grid with a model timestep of 10 minutes for the physics and chemistry calculations and 120 minutes for radiation. Output was written every three days. Ozone is calculated interactively with the simplified Linoz scheme in the simulation and is coupled back with the radiation scheme and can thus influence the circulation.

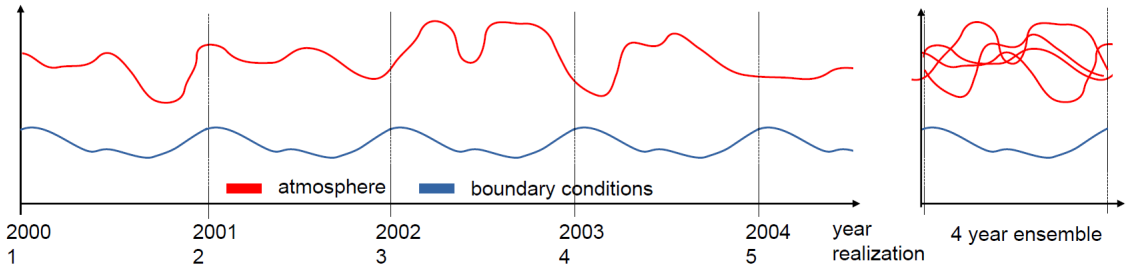

Figure 3.2: Schematic drawing of the experimental timeslice design.

The timeslice setup implies a free-running simulation with yearly repeating boundary conditions for sea surface temperatures (SST), sea ice cover (SIC), greenhouse gases (GHG), solar irradiance, and natural and anthropogenic aerosols. A schematic drawing of the experimental design is shown in Figure 3.2. Each year of the timeslice simulation is forced with the same boundary conditions and can thus be interpreted as one ensemble member. This enables us to mimic an ensemble of atmospheric states for the given boundary conditions and, therefore, gain information about the simulation's internal variability. Internal variability is associated with the natural year-to-year variability of the climate system for fixed boundary conditions without changes in forcing and does not include naturally forced changes in the climate system due to changes in e.g. solar irradiance. In the following, each year of a timeslice simulation is referred to as one ensemble member or one

realization. The term "ensemble mean" refers to the mean calculated from the individual realizations.
Five main model experiments have been performed:

1. "POC 2000": This experiment uses idealized boundary conditions for the year 2000 and includes polar ozone chemistry resulting in the formation of an Antarctic ozone hole. Including polar ozone chemistry in the Linoz scheme is achieved by setting the polar ozone lifetime τ_{PSC} to following values:

$$\tau_{\mathrm{PSC}} = \begin{cases} 10 \text{ days} & \text{for } \vartheta < 90^{\circ} \text{ and T} < 195\text{K} \\ \infty \text{ days} & \text{else} \end{cases}$$

   where ϑ denotes the solar zenith angle and T denotes the temperature.

2. "noPOC 2000": This experiment uses idealized boundary conditions for the year 2000 and neglects polar ozone chemistry resulting in the absence of an Antarctic ozone hole. Here, the polar ozone lifetime is set to:

$$\tau_{\mathrm{PSC}} = \infty \text{ days}$$

3. "noPOC 1980": As experiment 2 for the year 1980.

4. "POC 2060": As experiment 1 for the year 2060 and boundary conditions according to the RCP6.0 scenario (Masui et al., 2011).

5. "noPOC 2060": As experiment 2 for the year 2060 and boundary conditions according to the RCP6.0 scenario (Masui et al., 2011).

An overview of the main model experiments is shown in Table 3.2. In addition, sensitivity studies were performed to investigate the impact of changes in solar zenith angle and tropospheric ozone lifetimes.

Table 3.2: Overview of the main model experiments

experiment	boundary conditions	polar ozone chemistry
POC 2000	2000	included
noPOC 2000	2000	neglected
noPOC 1980	1980	neglected
POC 2060	2060 (RCP 6.0)	included
noPOC 2060	2060 (RCP 6.0)	neglected

Table 3.3: Boundary conditions

Variable	Reference
Spectral solar irradiation	Lean et al. (2005)
SST/SIC	Taylor et al. (2000), Hardiman et al. (2017)
GHG (RCP 6.0)	Masui et al. (2011)
Anthropogenic aerosol	Stevens et al. (2017)
Natural aerosol	Stenchikov et al. (1998, 2004, 2009)

Since the polar ozone lifetime of 10 days that is used in the Linoz scheme for the POC simulation was optimized based on Arctic ozone measurements in 2000, it represents ozone-depleting substance (ODS) conditions for 2000. Changes in ODS are not taken into account with this lifetime-based approach. Therefore the POC 2060 simulation can be interpreted as a "what if" scenario, while the noPOC 2060 is interpreted to be the "realistic" scenario, based on the assumption that the ozone hole has recovered by 2060. Further, the noPOC 1980 scenario is assumed to be a realistic representation of 1980. The POC 2000 and noPOC 1980 experiments are evaluated in chapter 5 by comparison with observational and reanalysis data to obtain insights about the model characteristics and the implications for the other experiments and their interpretation.

The perpetually applied boundary conditions for a given year are part of the experimental design of this study. This allows the investigation of the impact of the ozone changes on climate separate from other perturbations of the climate system and assessing natural variability. To remove a large impact of natural variability in the boundary conditions, five-year averaged boundary conditions were obtained for SST/SIC, spectral solar irradiation, GHG, and anthropogenic aerosols. While slowly varying boundary conditions (GHGs and natural and anthropogenic aerosols) are fixed, faster varying boundary conditions (SST, SIC, and solar irradiance) are defined with an annual cycle.

For the simulations of the year 2000 (POC 2000 and noPOC 2000), the period between 1998 - 2002 was used to calculate mean boundary conditions based on observational data. For natural aerosol, the conditions of the year 1999 were used. For the 1980 experiment, the mean boundary conditions for 1978 - 1982 were used for SST/SIC, spectral solar irradiation, greenhouse gases, and anthropogenic aerosols. For natural aerosol, the conditions of the year 1980 were used.

For the year 2060, boundary condition projections for spectral solar irradiation and greenhouse gases according to the RCP 6.0 scenario were used. To ensure consistent SST and SIC conditions, SST and SIC anomalies were obtained from simulations of the HadGEM models (Hardiman et al., 2017; MOHC (Met Office Hadley Centre) Data, 2020-02-14)

Ref-C2 simulation that was run with a coupled ocean and the RCP 6.0 scenario greenhouse gas forcing. Anomalies were calculated between the mean conditions of the years 1998 - 2002 and 1958 - 2062. Those anomalies were then added to the mean boundary conditions used for the year 2000 simulations.
Since the projection of aerosol concentrations is challenging and at least for volcanic aerosols not feasible, the same aerosol boundary conditions were used for the 2000 and 2060 experiments. An overview of the references for the used boundary conditions is given in Table 3.3.

4 Methods

4.1 Significance calculations

The climate change signals obtained in this study are tested for significance. This implies significance calculations at numerous locations arranged in the model grid. Significance calculations of gridded data are often performed by individual significance tests at every grid point. The resulting patterns of significance are often overinterpreted due to a neglect of accounting for the problems that arise from multiple testing (Wilks, 2016; Livezey and Chen, 1983).

When performing a single hypothesis test, a null hypothesis H_0 is defined that will be rejected if a sufficiently extreme test statistic is observed. A rejection at level α means that the probability (called p-value) of observing this test statistic (or one even less favorable for the null hypothesis), if H_0 is true, is no larger than α. This implies that any true null hypothesis is rejected with a probability of α. Following that, a set of n hypothesis tests with only true null hypotheses will show on average $n \cdot \alpha$ erroneous rejections. Even though this is the average number of erroneous rejections, for a large n, it is very likely, that at least one true null hypothesis is rejected. Considering that the hypothesis tests are not independent of each other, which will be the case for most multiple testing problems of gridded data, the probability for higher numbers of erroneously rejected null hypotheses will be even higher. This assumption is based on the prerequisite that all null hypotheses are actually true. In reality, the analysis of the result of multiple hypothesis tests is additionally complicated by the unknown ratio of true to false null hypotheses and the possibility of false null hypotheses being classified as true (e.g. Wilks, 2016).

In order to account for the problems that arise from multiple testing of gridded data, we use an approach called "Controlling the False discovery rate", which was first described by Benjamini and Hochberg (1995).

A rejection of a local null hypothesis is called a "false discovery" if this hypothesis is actually true. The false discovery rate (FDR) describes the statistically expected fraction of those false discoveries. An upper limit for this rate can be controlled exactly for independent local tests regardless of the unknown fraction of true to false null hypotheses. Wilks (2016) also shows that the FDR procedure is applicable to spatially correlated grid points. However, if the correlation is high, the achieved FDR will be smaller (more strict) than the given threshold.

Controlling the false discovery rate is achieved by first collecting the resulting p-values of all individual N significance tests p_i with $i = 1, ..., N$ and sorting those p-values in ascending order so that $p_{(1)} \leq p_{(2)} \leq ... \leq p_{(N)}$. When applying the FDR procedure, a null hypothesis is rejected if its corresponding p-value is no larger than a threshold p_{FDR}. This threshold depends on the distribution of the sorted p-values and the chosen control level α_{FDR}. The threshold is calculated by finding the largest $p_{(i)}$ that is no larger than the fraction of α_{FDR} specified by i/N.

$$p_{FDR} = \max_{i=1,...,N} [p_{(i)} : p_{(i)} \leq (i/N)\alpha_{FDR}] \tag{4.1}$$

A more detailed description of the procedure can be found in Wilks (2016).
To avoid overinterpretation of the results in this study, a two-sided t-test (Student, 1908) was performed at all individual points, and the FDR was controlled afterward with $\alpha_{FDR} = 0.1$.

4.2 Ensemble based uncertainty quantification

In addition to identifying significant points, it is desirable to obtain uncertainty estimates for the climate change signals detected in this study. The uncertainty of signals depends critically on the models' ability to cover internal variability sufficiently and thus on the number of realizations. Consequently, a large number of ensemble members would be desirable to minimize uncertainties. However, due to computational resources, only a certain number of ensemble members is feasible. Thus, an estimate of how large the uncertainties are compared to the detected signals' strength is applied in this study for near-surface temperature signals. An uncertainty estimate that is distinctly smaller than the detected signal suggests a sufficient sample size. In contrast, uncertainties with the same magnitude as the detected changes indicate an insufficient representation of the internal variability. Therefore, the uncertainties of the climate change signals between two simulations are quantified by the following procedure.
First, the two model experiments (that the climate change signals are calculated for) and the subset size k (indicating the number of realizations used for the analysis) are chosen. Now, k realizations are randomly drawn from the corresponding experiments, resulting in two subsets of years with size k. In the next step, resampling is performed according to the jackknife method (e.g. Efron and Gong, 1983): from each set, one realization is left out. This is done for all possible combinations, thus resulting in k^2 combinations. The mean surface temperature difference is then calculated for each of the k^2 combinations and the complete sets of k chosen realizations. Following, minimum and maximum mean surface temperature differences at each grid point are detected from the k^2 calculations.

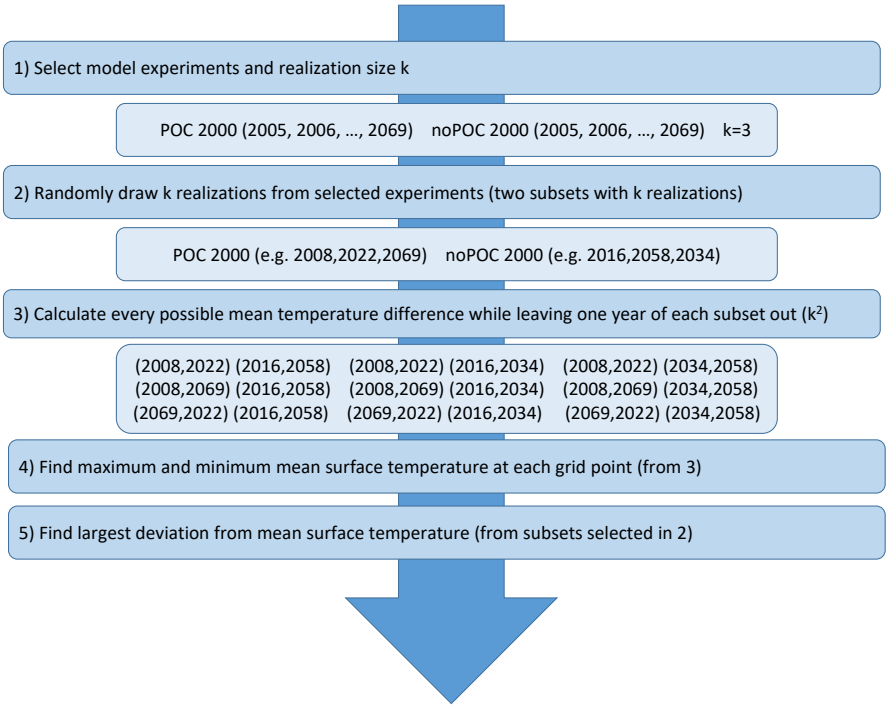

Figure 4.1: Workflow of the ensemble based uncertainty calculation procedure

The uncertainty estimate is then given by the largest anomalies of the mean difference calculated from the full sets of k chosen realizations. This approach quantifies the influence of individual realizations on the overall result for a given sample size.

An example workflow for the POC 2000 and noPOC 2000 experiments with a realization size of k=3 is shown in Figure 4.1. Here, from each experiment with 65 realizations, three years are randomly chosen that are further analyzed. A realization size of k=3 was chosen for a simplified explanation of the procedure. To analyze the actual uncertainties between two model experiments, the full realization size of 65 years is chosen. To further investigate the impact of the realization size, values between 20 and 65 have been chosen for k. The results are discussed in section 6.2.2.

4.3 Principal component analysis

Variability in the climate system and the coupling between the stratosphere and the troposphere are analyzed based on the characteristics of the Southern Annular Mode (SAM). The SAM is typically defined as the first empirical orthogonal function (EOF) of the southern hemisphere. Therefore, in the next section, the principles of principal component analysis (PCA) and its applications to climate data are introduced. This introduction is mainly based on Wilks (2006) and Navarra and Simoncini (2010).

PCA is used to calculate a new set of variables (principal components, PCs) from linear combinations (empirical orthogonal functions, EOFs) of the original variables. The selection of linear combinations is driven by a redistribution of the total variance on the new variables so that the first PCs explain the most variance any variables can explain while the last variables explain the least variance any variables can explain. The redistribution is subject to the condition that the resulting PCs are mutually uncorrelated. This leads to a new set of variables that contain the same amount of information as the original data, and the original dataset can be rebuild from those new variables.

Mathematically this is done by calculating the eigenvectors (that are equivalent to the linear combination loadings) and eigenvalues of the dataset's covariance matrix.

Consider a dataset organized in a two dimensional matrix X:

$$X = \begin{bmatrix} x_{11} & x_{12} & \cdots & x_{1n} \\ x_{21} & x_{22} & \cdots & x_{2n} \\ \vdots & \vdots & \vdots & \vdots \\ x_{m1} & x_{m2} & \cdots & x_{mn} \end{bmatrix} \quad X \in \mathbb{R}^{m \times n} \tag{4.2}$$

where m is the number of variables and n is the number of observations.

In a first step, the dataset is centered to obtain an anomaly matrix X′:

$$X' = x'_{ij} = x_{ij} - \frac{\sum_{j=1}^{n} x_{ij}}{n} \quad X' \in \mathbb{R}^{m \times n} \tag{4.3}$$

The covariance matrix S is then calculated by:

$$S = \frac{1}{n-1} X' X'^{T} \quad S \in \mathbb{R}^{m \times m} \tag{4.4}$$

Applying singular value decomposition, X′ can be formulated as:

$$X' = U \Lambda V^{T} \tag{4.5}$$

with

$$U \in \mathbb{R}^{m \times m} \quad U^{T} U = I \tag{4.6}$$

$$\Lambda \in \mathbb{R}^{m \times n} \tag{4.7}$$

$$V \in \mathbb{R}^{n \times n} \quad V^{T} V = I \tag{4.8}$$

and I denotes the identity matrix. Following S can be rewritten as:

$$S = \frac{1}{n-1} U \Lambda V^T V \Lambda^T U^T = \frac{1}{n-1} U \Lambda \Lambda^T U^T \tag{4.9}$$

This implies that the matrix U is equivalent to the matrix of eigenvectors of S, while $\Lambda\Lambda^T$ corresponds to the eigenvalues of S:

$$U = [e_1 \quad e_2 \quad \cdots \quad e_m] \quad e_i \in \mathbb{R}^{m \times 1} \tag{4.10}$$

$$\Lambda\Lambda^T = \begin{bmatrix} \lambda_1^2 & & \\ & \ddots & \\ & & \lambda_m^2 \end{bmatrix} \quad \Lambda\Lambda^T \in \mathbb{R}^{m \times m} \tag{4.11}$$

The data matrix X′ can then be rewritten as:

$$X' = UY \tag{4.12}$$

$$Y = [y_1 \quad y_2 \quad \cdots \quad y_m]^T \quad y_i \in \mathbb{R}^{1 \times n} \tag{4.13}$$

or alternatively:

$$y_i = e_i^T X' \tag{4.14}$$

$$e_i = X' y_i^T \tag{4.15}$$

where e are the eigenvectors of S or empirical orthogonal functions (EOFs) and y are the principal components.
The eigenvalues of S can be used to calculate the explained variance R^2 for every PC:

$$R_i^2 = \frac{\lambda_i^2}{\sum_k \lambda_k^2} \tag{4.16}$$

Typically the EOFs and PCs are then sorted by the calculated explained variance with PC1 corresponding to the highest explained variance.

4.3.1 Application of PCA to climate data

While PCA is generally often used for data compression, it is also widely used to analyze the spatial and temporal structure of variations in atmospheric science. Climate data is typically organized in time series of a given variable at various locations. When applying PCA to this kind of data, the dimensions m and n from the previous sections correspond to the number of locations and the time series' length. This implies the possibility to interpret the EOFs as geographic distribution of simultaneous data anomalies or modes of

variability represented by the corresponding PCs. The PCs are corresponding to the time series of the strength of the particular modes.

If PCA is applied to fields, the distribution of grid points needs to be taken into account. Depending on the chosen grid architecture, certain regions can be overrepresented while others are underrepresented. This is the case for non-equal-area grids like a regular latitude-longitude-grid. In this case, a weighting with multiplication by $\sqrt{\cos\varphi}$ with latitude φ is applied to balance the unequal distribution. This weighting is applied for the calculation of PCA for ERA5 data. The triangular ICON grid meets the requirements of an equal-area grid, and therefore no weighting needs to be applied in this case.

The application of PCA in this study is used to calculate the Southern Annular Mode, which is frequently used for climate data analysis. The Southern Annular Mode can be calculated at every pressure level and is defined as the first EOF calculated from geopotential anomalies of monthly data. As an example, the characteristics of the SAM at the 600 hPa level for the POC 2000 simulation are depicted in Fig. 4.2.

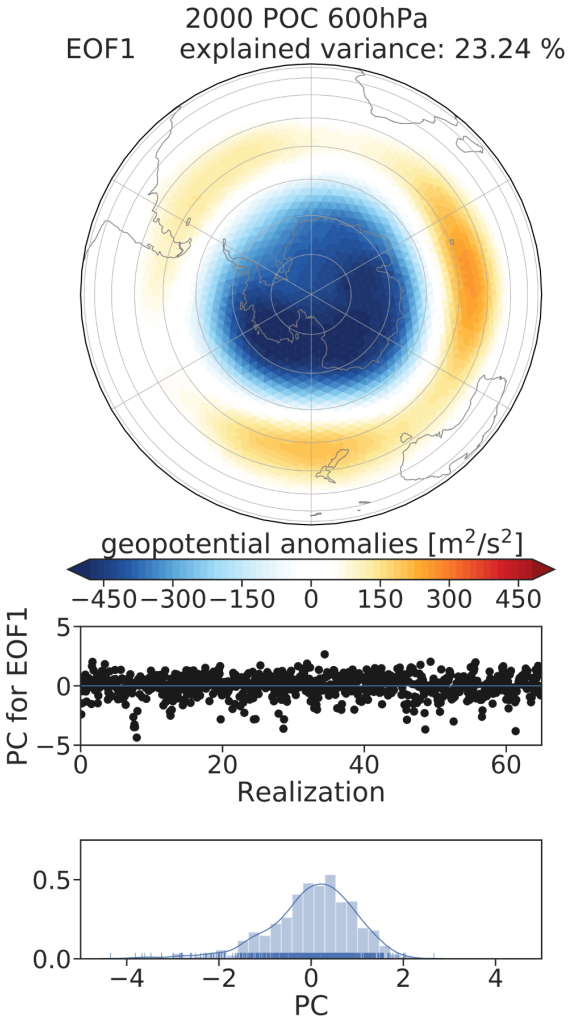

Figure 4.2: Characteristics of the SAM at the 600 hPa level for the POC 2000 simulation

As mentioned previously, each EOF can be interpreted as geographical distribution of simultaneous data anomalies. The pattern for the 600 hPa SAM calculation of the POC 2000 simulation is characterized by negative anomalies south of 60°S and weaker positive anomalies between 60°S and 40°S. In conclusion, positive SAM indices are associated with a weaker than usual geopotential in the polar region and an increased geopotential for the band between 60°S and 40°S, while a negative index results in stronger than usual geopotential in the polar region and a decreased geopotential between 60°S and 40°S. At 600 hPa, this is the leading mode of variability that accounts for 23.24 % of the variance. The corresponding principal component forms a time series indicating the observed anomaly pattern's strength at each month of the input dataset. Due to the timeslice approach explained in section 3.4, each year of the time series can be interpreted as one possible realization of the year 2000. Therefore, the SAM indices' statistical distribution is of particular interest, as it indicates the climatological occurrence of high or low SAM indices for the different ICON-ART simulations.

4.3.2 Deseasonalization of ICON-ART data

In order to apply PCA, anomalies of the datasets need to be generated. This is realized by subtracting a mean annular cycle from the geopotential values at every grid point used for the southern hemispheric PCA calculation. For monthly mean data, the mean annular cycle is obtained by calculating the mean of all monthly means for the corresponding month.

Generating a mean annular cycle is more difficult when working with the ICON-ART output available every three days. Consequently, not every day of the year is represented by every ensemble member. Further, certain days of the year are less often represented than others. Therefore a mean annular cycle cannot just be obtained by averaging all years but was obtained by a moving average approach.

In the first step, the mean value is calculated for every day of the year at every grid point. Due to the output availability, a different number of years is used to calculate the mean of different days of the year. Therefore, the number of days used for the mean calculation of a given day is identified.

$$\overline{x}_i = \frac{\sum_{k=1}^{n_i} x_{ik}}{n_i} \tag{4.17}$$

with n_i as the number of ensembles that contain day i.

The moving average was then calculated with a lag of 5 days:

$$MAV_{5,i} = \frac{\sum_{j=-5}^{5} \bar{x}_{i+j}\, n_{i+j}}{\sum_{j=-5}^{5} n_{i+j}} \tag{4.18}$$

The anomalies were then calculated by subtraction of the generated mean annular cycle:

$$\bar{x}'_i = x_i - MAV_{5,i} \tag{4.19}$$

The same procedure was applied for daily ERA5 data for a consistent calculation of the anomalies.

4.3.3 Projection of data to obtain new time series or spatial patterns

In this study, we apply PCA to monthly geopotential anomalies for southern hemispheric grid points at individual pressure levels to calculate the SAM with a monthly time resolution from the ICON-ART simulations. However, it is sometimes desirable to obtain a higher time resolution, particularly to investigate coupling processes between different atmospheric levels. Therefore, a new SAM index time series with a temporal resolution of 3 days was generated by the projection of deseasonalized data with the initial resolution of 3 days on the EOF pattern obtained from the monthly calculation.

Generally, it is possible to obtain a new time series $y_{i,new}$ (or spatial pattern $e_{i,new}$) by projecting a given dataset W onto a given spatial pattern e_i (or PC time series y_i) if the corresponding time or location dimensions are the same (e.g. Baldwin et al., 2009).

Consider the data matrix $W \in \mathbb{R}^{pxq}$. A new time series can be obtained if p=m, where p is the number of locations of the matrix W and m is the number of locations of the initial matrix X used for the PCA calculation:

$$y_{i,new} = \frac{e_i^T W}{e_i e_i^T} \tag{4.20}$$

with $y_{i,new} \in \mathbb{R}^{1xq}$.

In Fig. 4.3 an example for the generation of a new SAM index time series is depicted for the first five years of the POC simulation (top panels). While the overall temporal evolution of both time series is similar, the SAM index for the ICON-ART data with an output every three days shows a significantly higher spread. This behavior is also mirrored in the SAM index's climatological distribution calculated from all realizations depicted in the bottom panel.

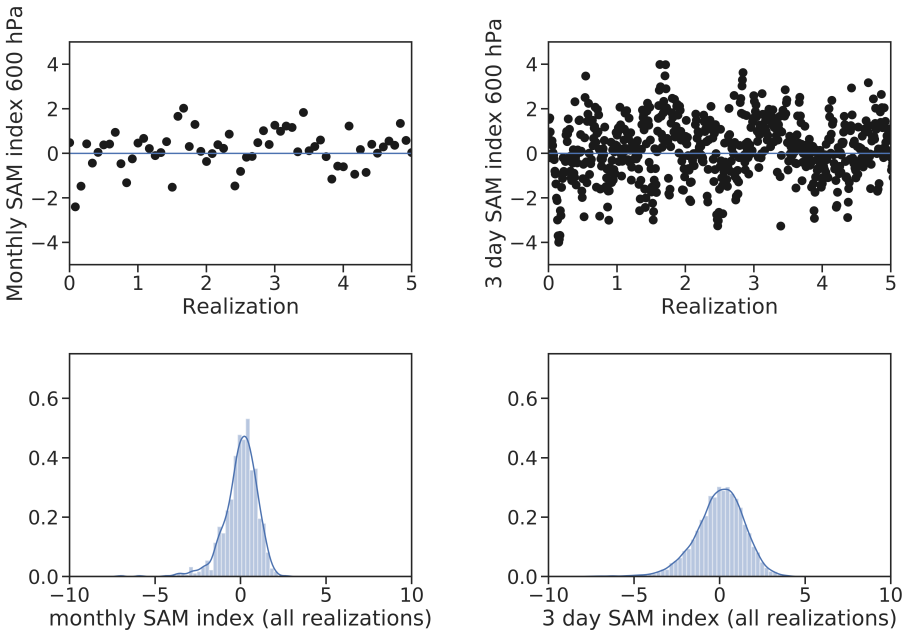

Figure 4.3: Comparison of the SAM time series with a monthly resolution and the generated SAM time series with a resolution of 3 days.

Similarly, it is possible to obtain new spatial patterns when projecting a dataset on the SAM index time series. This is used to analyze how the SAM (that indicates deviations in geopotential) is reflected in other variable fields (e.g. temperature).

A new spatial pattern can be generated if q=n where q is the size of the time dimension of the matrix W and m is the time dimension size of the initial matrix X used for the PCA calculation:

$$e_{i,new} = \frac{W y_i^T}{y_i y_i^T} \tag{4.21}$$

with $e_{i,new} \in \mathbb{R}^{px1}$.

An example of the generation of a new anomaly pattern is shown in Fig. 4.4. This pattern was obtained by the projection of the SAM index time series at 600 hPa on the temperature anomalies detected during the same time. This pattern indicates that negative temperature anomalies in the polar region are associated with a positive annular mode index, while a negative index results in higher than usual temperatures in the polar region.

4.3.4 Comparability of annular mode calculations

Various changes in the climate system are associated with trends in the Southern Annular Mode time series. To reconstruct the observed changes from the timeslice simulations used in this study, it is desirable to calculate an annular mode pattern and indices that are comparable between different experiments.

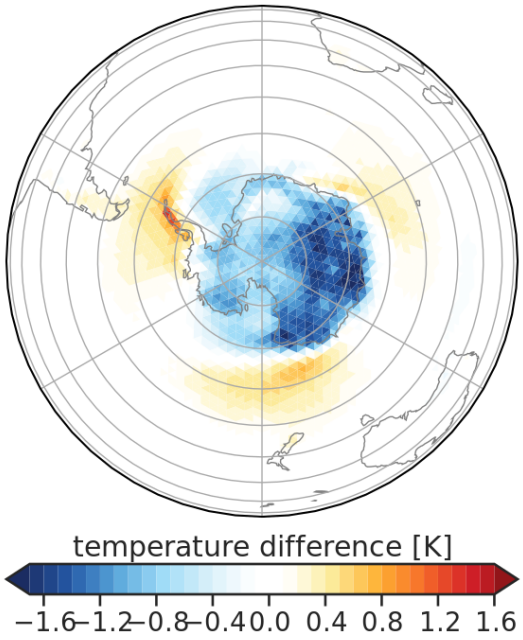

Figure 4.4: Temperature pattern obtained from the regression of temperature anomalies on the SAM time series.

The annular mode pattern calculation for a single run is based on monthly anomalies in geopotential and results in distinct patterns and time series for the various simulations. The SAM characteristics at 600 hPa for the POC 2000, noPOC 2000, and POC 2060 simulations are shown in Fig. 4.5.

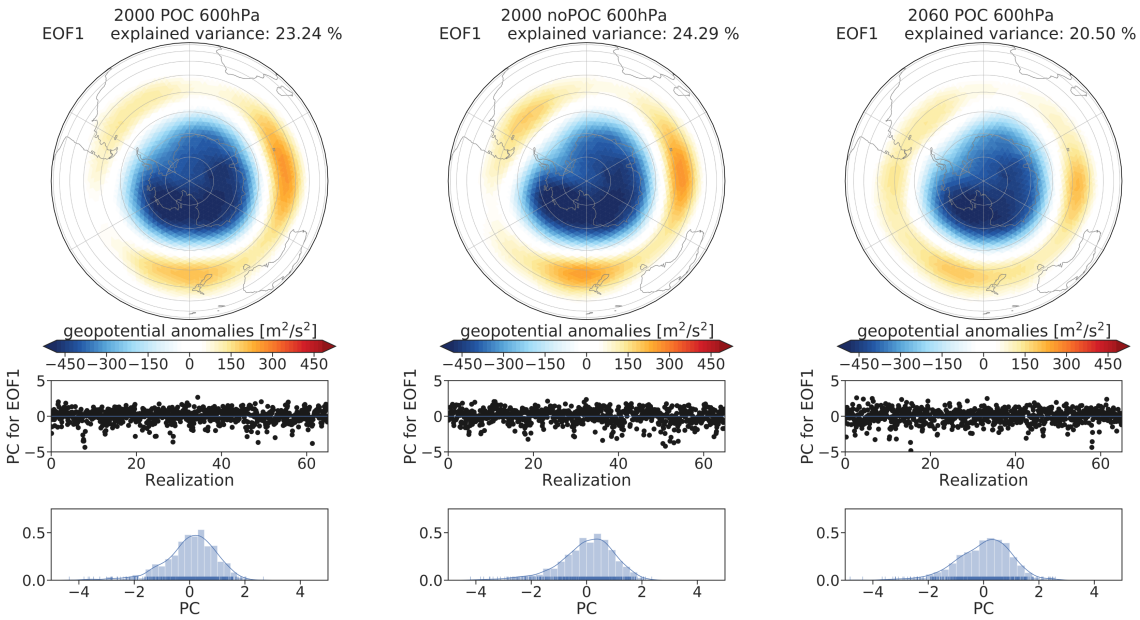

Figure 4.5: SAM characteristics at 600 hPa for the POC 2000, noPOC 2000, and POC 2060 simulations

The different simulations show a similar annular mode pattern, with slight changes in the zonal character of negative geopotential anomalies associated with a positive SAM index. The distribution of occurring annular mode indices is centered around zero due to the annular modes' definition as the pattern of temperature anomalies deviating from the mean state. So far, an individual climatological mean was calculated for every ICON-ART simulation that was used to obtain the monthly anomalies. However, these climatologies vary between different runs. To compare the distribution of the annular mode indices, it is desirable to calculate one common annular mode pattern from the simulations that are compared. This mutual annular mode pattern is calculated by monthly anomalies from both runs based on one mean climatological state for both runs together. The results of a common annular mode calculation for the POC 2000 and noPOC 2000, as well as the POC 2060 and POC 2000 simulations, are shown in Fig. 4.6.

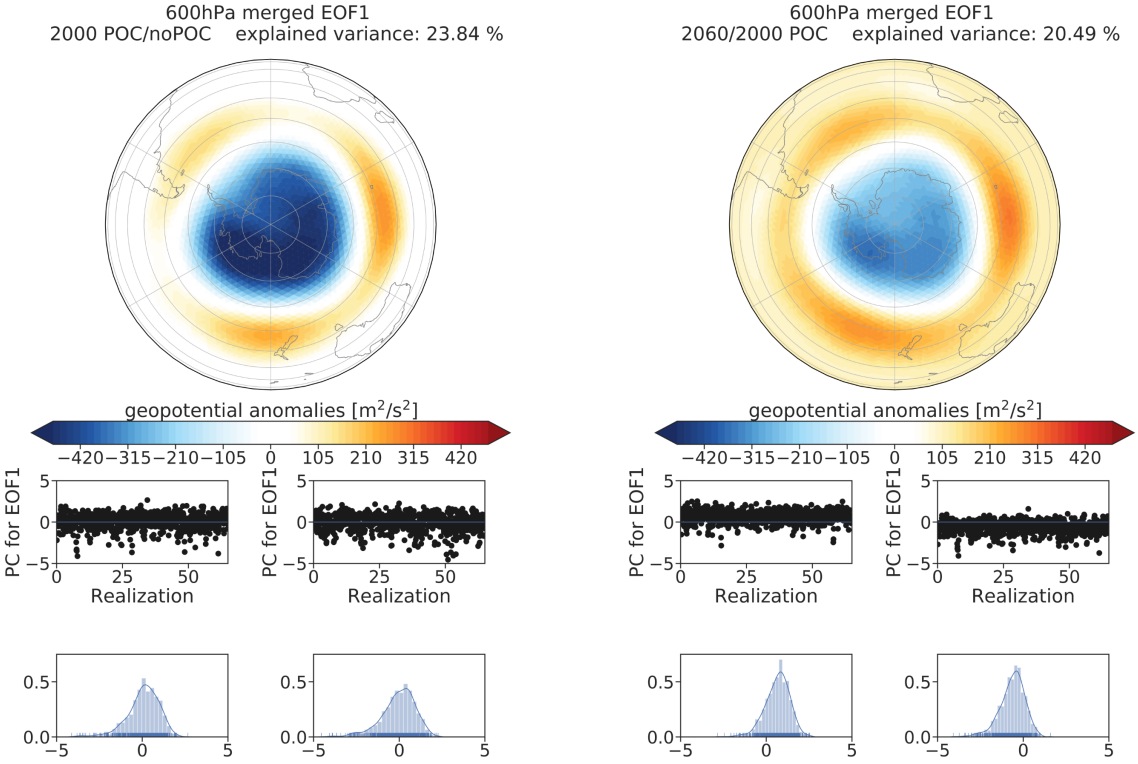

Figure 4.6: SAM characteristics at 600 hPa for the merged calulation of the POC 2000 and noPOC 2000 simulations as well as the POC 2060 and POC 2000 simulations.

For the POC 2000 and noPOC 2000 calculation, the calculated pattern is very similar to the individual simulations' patterns shown in Figure 4.5. The annular mode index time series are also comparable to the individual calculations. Looking at the mutual calculation for the POC 2060 and POC 2000 simulations, the picture is different. Here, the pattern is altered, with an additional increase in geopotential anomalies north of 40°S. Consequently, due to the normalization of the EOF, the initial pattern is weakened. The SAM indices corresponding to the POC 2060 simulation are significantly shifted towards

positive values for this calculation. The indices of the POC 2000 simulation are shifted towards negative values, thus resulting in two distinct populations.

The modulation of SAM pattern and indices for common calculations of two different simulations is therefore dependent on the differences of the climatological means of the individual simulations. In the case of similar individual climatologies, as is the case for the POC 2000 and noPOC 2000 simulations, the common climatology is close to the initial climatologies. Therefore the pattern and index are not strongly altered. Suppose the initial climatologies show a larger discrepancy, as for the POC 2060 and POC 2000 simulations. In that case, the calculated anomalies from the common climatology are significantly higher, with a tendency towards positive anomalies for one experiment and negative anomalies for the other. As a result, a significant shift in annular mode indices is observed.

Particular challenges are posed when the differences between the individual climatologies are not mainly induced by climatological changes of the Southern Annular Mode, as is the case for the POC 2060 and POC 2000 calculation. Here, climatological changes are globally induced due to GHG forcing changes, resulting in higher geopotential values. In this case, the calculation of a mutual climatology results in characteristic positive or negative anomalies in the regions not affected by the annular mode. Consequently, these regions show high variability between the two simulations and are thus interpreted as a part of the annular mode pattern when using EOF calculations to define the annular mode pattern and index. This behavior is apparent for the grid points north of 40°S. Due to the blurring of the initial SAM pattern, the SAM indices are affected as well. Depending on the strength of the superimposed climate change pattern, the indices can be intensified or weakened. Therefore, scenarios with large changes between the individual climatologies should be interpreted with caution. A possible approach to improve results might be limiting the annular mode calculation to grid points south of 40°S or an advanced detrending approach for non annular mode affected grid points. However, a general detrending approach, which is a calculation of anomalies from individual climatologies, and a subsequent mutual pattern calculation from those anomalies result in the disregard of climatological annular mode changes as well and is therefore not suitable to identify changes in annular mode indices.

Due to the challenges of a common annular mode calculation, we use individual calculation for most of the analysis workflows in this study. Here, it should be noted for interpretation that the annular mode patterns and individual climatologies can vary. In contrast, for certain applications, a common calculation is desirable to detect climatological changes in annular mode indices. The challenges presented in this section should be kept in mind for the analysis of the resulting findings.

4.4 PCA based analysis methods: Temporal structure of annular modes

The vertical coupling between the stratosphere and troposphere and the temporal structure of annular modes is analyzed in chapter 7. The methods used for this analysis are described in this section. All methods are based on daily SAM indices at the different vertical pressure levels. Daily indices were obtained by the projection of daily geopotential anomalies onto the pattern obtained from the monthly EOF calculation. The daily anomalies were generated by linear interpolation of the anomalies generated for the output available every three days. An overview of the procedure is given in Figure 4.7.

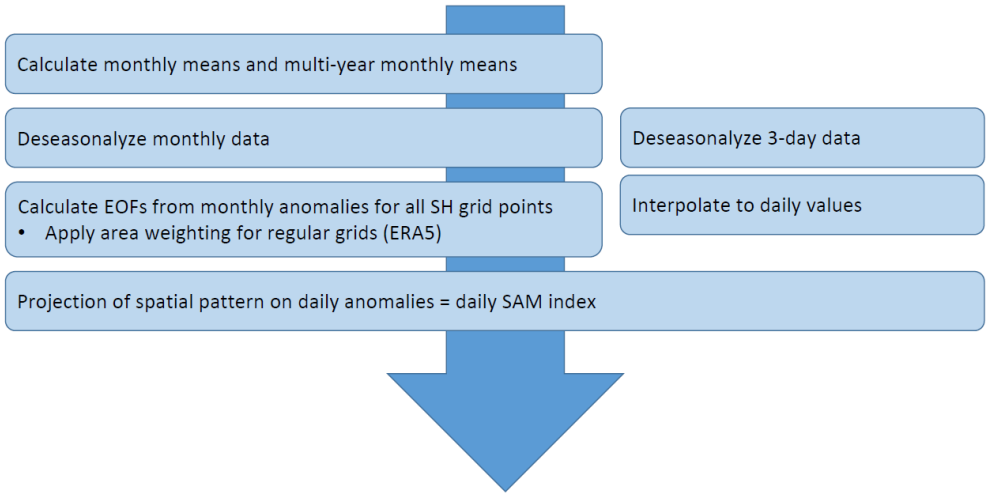

Figure 4.7: Workflow for the generation of daily SAM indices at a given level

4.4.1 E-folding timescale

To analyze the persistence of annular modes, a measure called e-folding timescale as described by Baldwin et al. (2003) is calculated. An overview of the procedure is given in Figure 4.8.

Based on the daily SAM time series at a given level, 365 new time series are generated. One new time series is obtained for every day of the year by multiplicating the initial daily SAM time series with a yearly periodical weighting. The weighting is characterized by a gaussian kernel with a standard deviation of $\sigma = 25$ days centered around the given day under consideration. The autocorrelation function is then obtained by correlating the time series for a given day with all time series with a lag of up to 150 days. The e-folding timescale is then defined as the time where the autocorrelation function decreases to $1/e$.

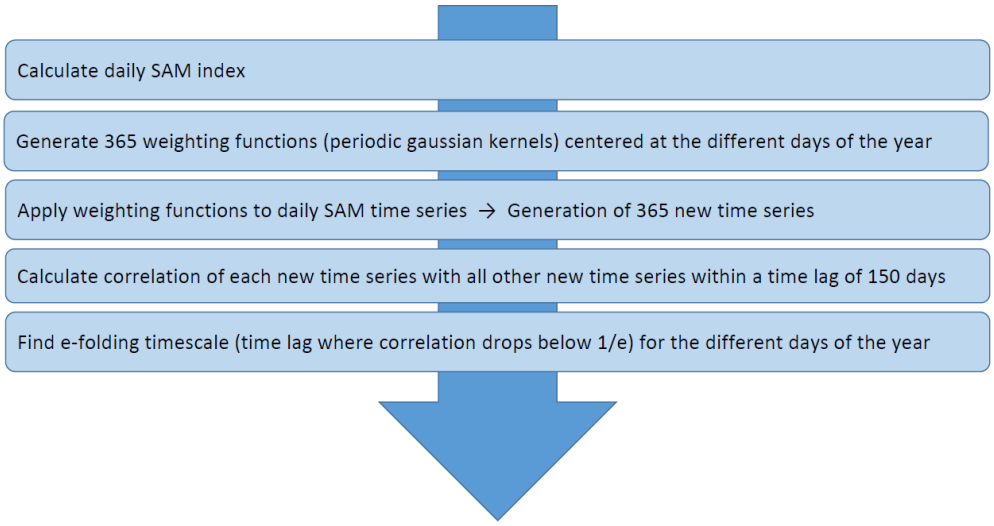

Figure 4.8: Workflow for the e-folding timescale calculation

4.4.2 Predictability

Further, the SAM index's prediction skill for a given month and level is calculated based on the procedure by Baldwin et al. (2003). The prediction skill indicates how good the SAM index at a given level is suited to estimate the mean near-surface SAM index with a lead time L of 25 days. An overview of the procedure is given in Figure 4.9.

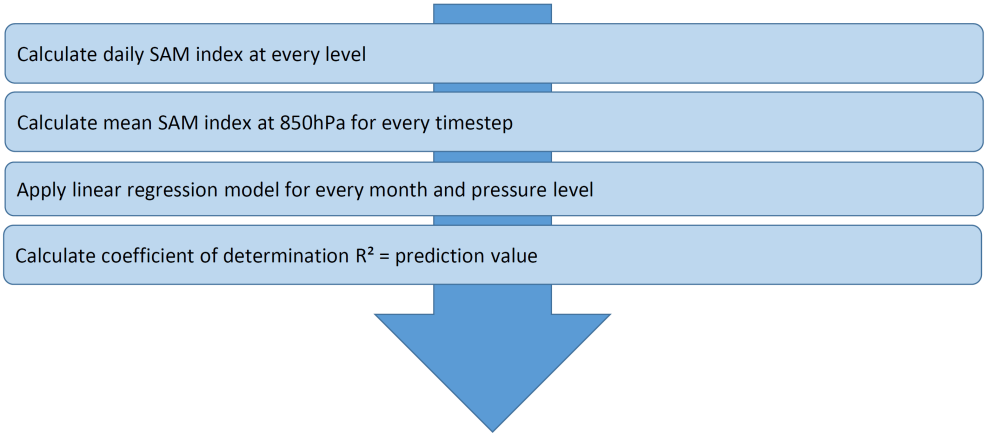

Figure 4.9: Workflow for the prediction calculation

For the calculation of this measure, the daily SAM time series at every level is calculated in the first step. Afterwards, the mean near-surface SAM index is calculated. This mean SAM index is calculated at 850 hPa for every timestep by the 30-day mean with a lead time of 25 days:

$$\overline{SAM}(t+L) = \frac{\sum_{i=10}^{39} SAM_{850}(t+i)}{30} \tag{4.22}$$

$$\tag{4.23}$$

Following, a linear regression model for every month and pressure level is applied:

$$\overline{SAM}(t+L) = \beta_0 + \beta_1 \mathrm{SAM}_{lev}(t) + \varepsilon \tag{4.24}$$

where $\beta_{0,1}$ are the regression parameters and ε are the residuals. $\beta_{0,1}$ are estimated with a least squares estimation. The prediction value for a given month and level is then characterized by the coefficient of determination R^2 of the corresponding linear regression.

5 Model evaluation

In this chapter, the model's ability to reproduce ozone characteristics is analyzed, focusing on the southern hemisphere. For a meaningful interpretation of ozone hole induced climate change signals, a realistic representation of ozone in the model simulations is fundamental. The usage of the linearized ozone scheme Linoz (as described in section 3.2) offers a possibility to study interactions between atmospheric chemistry, dynamics, and radiation while requiring only limited computational resources compared to a full chemistry scheme. However, the scheme's simplicity limits the opportunities to cover all aspects of chemistry-climate interactions, particularly the role of changing ozone-depleting substances. In combination with the timeslice approach (as described in section 3.4), this shortcoming becomes less critical, as only fixed boundary conditions are used in the individual simulations. However, the timeslice approach complicates the comparison with observational data and reanalysis datasets, as a direct comparison is not feasible.

To investigate the model's performance, we compared the noPOC 1980 simulation with data for 1979 - 1982 and the POC 2000 simulation with data for 1998 - 2002. These comparisons allow evaluating the Linoz scheme's suitability for a realistic representation of ozone concentrations for time horizons with and without the development of the ozone hole. When interpreting the results, it should be noted that this is no direct comparison but an opportunity to test if the ICON-ART climate simulations can reproduce the climatological characteristics.

First, the Antarctic ozone hole characteristics are investigated for the POC 2000 simulation, focusing on the optimal choice of the solar zenith angle threshold in the polar ozone chemistry representation of the Linoz scheme. This is further investigated by the comparison of total column ozone (TCO) distributions for different SZA choices, followed by the comparison of global TCO climatologies for the noPOC 1980 and POC 2000 simulations with observational and reanalysis data. Afterwards, the simulated vertical profiles of ozone and temperature are compared with ozonesonde measurements at multiple stations in the southern hemisphere.

5.1 The Antarctic ozone hole: influence of the solar zenith angle threshold

Polar ozone destruction starts with the availability of sunlight. At stratospheric altitudes where the ozone layer is located, sunlight is available even at solar zenith angels higher than 90°. However, ozone depletion is stronger if more sunlight is available. In the simplified Linoz ozone chemistry scheme used by this study, ozone is depleted if a given solar zenith threshold is exceeded. The depletion then occurs with a fixed strength. Therefore, the choice of the SZA threshold is critical for a realistic representation of ozone depletion. This is particularly the case for the onset of ozone depletion in spring. A high threshold would lead to ozone depletion earlier in the year, while a low threshold would postpone the onset of ozone depletion.
In this sensitivity study, we investigate the optimal solar zenith angle threshold for the Linoz scheme to achieve an optimal representation of the southern hemispheric ozone hole. Four sensitivity runs have been performed with SZA thresholds of 92.5°, 90°, 87.5°, and 85° for the boundary conditions of the year 2000 and a tropospheric ozone lifetime of 30 days with 15 ensemble members after a 5-year spin-up period.
Various metrics can characterize the state of Antarctic ozone depletion. In this study, we compared the following metrics obtained from the four sensitivity simulations and observational data between 1979 - 2019 to find the optimal SZA threshold.

- ozone hole area: the area where the total ozone column is lower than 220 Dobson Units (DU). This is calculated by the number of grid points that show a value lower than 220 DU multiplied by the average grid cell area for the ICON-ART data.
- minimum total ozone column: the value of the lowest total ozone column observed.
- O_3 deficit: the total amount of mass that is lost compared to the amount of mass that would be present for a value of 220 DU.

The dataset used to compare the evolution of the Antarctic ozone hole is provided by the NASA ozone watch program. It consists of observational data from the TOMS (Total Ozone Mapping Spectrometer, McPeters et al., 1998), OMI (Ozone Monitoring Instrument, Levelt et al., 2006) and OMPS (Ozone Mapping and Profiler Suite, Flynn et al., 2014) instruments on different satellites for the period from 1979 onwards. Additionally, modeled data from MERRA (Modern-Era Retrospective Analysis for Research and Applications, Rienecker et al., 2011), MERRA-2 (Gelaro et al., 2017) and GEOS-FP (Rienecker et al., 2008) are used to fill missing satellite data and obtain the ozone hole characteristics. The data can be downloaded from the NASA ozone watch website (`https://ozonewatch.gsfc.nasa.gov`).

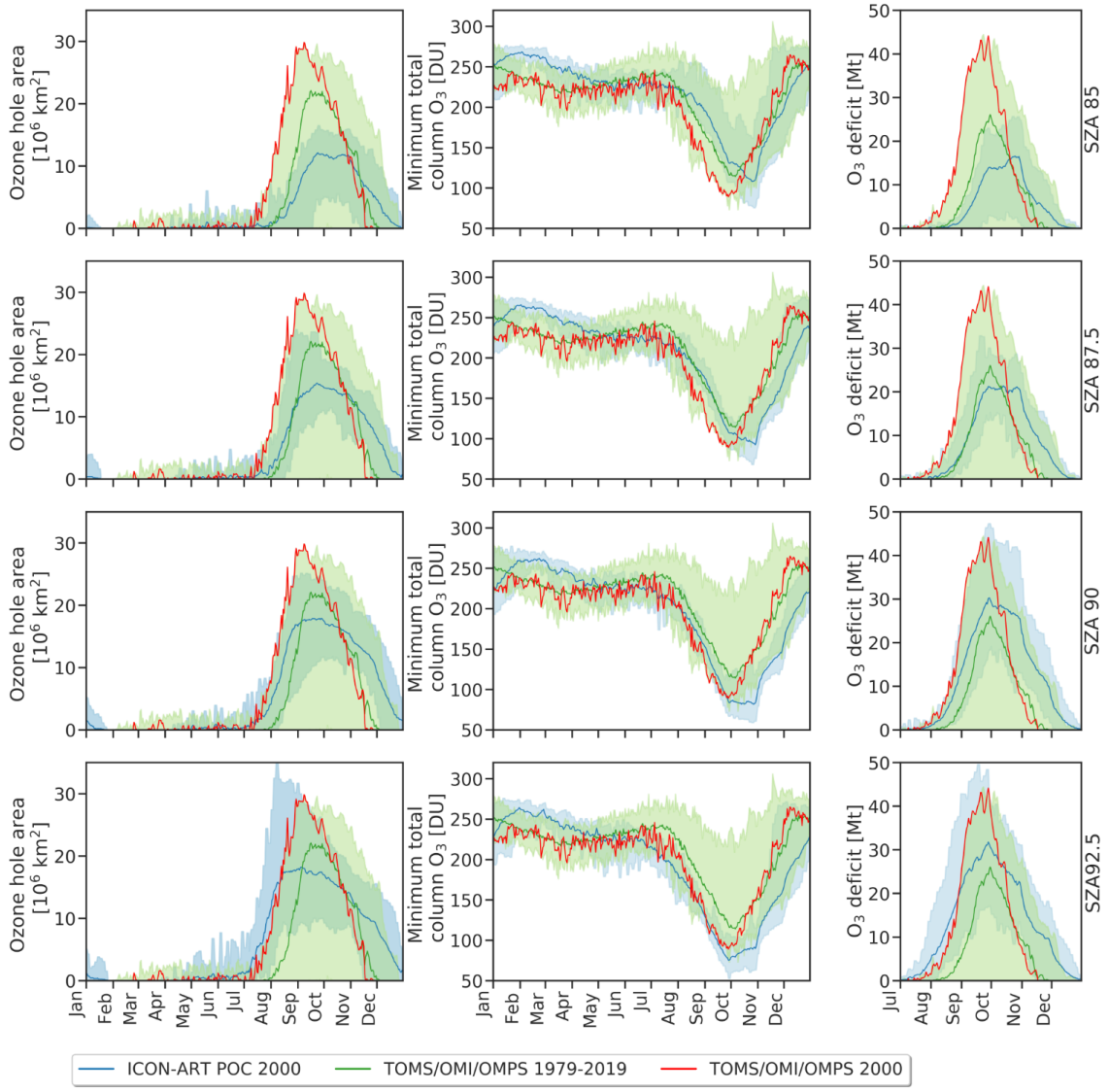

Figure 5.1: Ozone hole area, minimum column ozone and O_3 deficit for ICON-ART sensitivity simulations with a SZA threshold of 92.5°, 90°, 87.5° and 85° compared with satellite observations. red: observations from year 2000, green: mean values for observations between 1979 and 2019, blue: ensemble mean from ICON-ART simulation, light green shaded: range of observed values, light blue shaded: range of simulated values.

The development of the ozone hole area, minimum column ozone, and O_3 deficit is shown over the course of the year in Figure 5.1 for the ICON-ART simulations together with observational data. For each sensitivity run, the ensemble mean (blue line) and the model spread between minimum and maximum (light blue area) are used for comparison. The sensitivity runs are compared with the observations of the year 2000 (red line).

The observed ozone hole area for the year 2000 starts to increase in July, reaching a maximum by September and decreases until December. In accordance with this, the minimum total column O_3 is beginning to decline by July, reaching a minimum in early October and increases until December. This development of the ozone hole is also evident in the observed ozone deficit increasing from July to October and decreasing until December. The

year 2000 shows the largest ozone hole area ever observed between July and September, including the maximum ever observed value in late August. This corresponds with one of the lowest minimum total column ozone values during the same period resulting in an unprecedented ozone deficit between July and September.
Even though the potential for ozone depletion is assumed to be highest around the year 2000 (e.g. Dhomse et al., 2018), it is reasonable to assume that the year 2000 was stronger than the average case in terms of internal variability. Therefore the ensemble member means should not necessarily fit perfectly to the observed curve to identify the best SZA threshold. However, the observed curve should optimally be located within the bounds of the model spread. To determine the most realistic model setup, the multi-year mean of observational data from 1979 to 2019 (green line) and the spread (light green area) observed during that period are used for comparison. It should be noted that the first years in this period are showing little ozone depletion. However, they are included in the analysis to represent internal variability better. Even though the potential for ozone depletion is high around the year 2000, a weak ozone hole is still possible due to year-to-year variations in the dynamics. For example, in 2002, a sudden stratospheric warming occurred, leading to a vortex breakup in late September (e.g. Feng et al., 2005). Therefore in the analyzed metrics, particularly low values occurred during that year. The observed multi-year mean should therefore be interpreted as a lower boundary for the model ensemble mean.
The "SZA 85" and "SZA 87.5" simulations result in a weaker than observed ozone hole. This is reflected by the model spread not covering the range of observed values of the ozone hole area, minimum column ozone, and the ozone deficit for the year 2000. The "SZA 85" simulation is further characterized by a later than the usual onset of ozone depletion.
The "SZA 90" simulation shows a realistic onset of ozone depletion in July with the ensemble mean between the year 2000 observations and the multi-year during the depletion phase. For the ozone hole area, the maximum values observed in September 2000 are not covered by the model spread. The ensemble minimum/maximum for the minimum total column and the ozone deficit reach the observed values for 2000. The "SZA 92.5" simulation shows a wider ensemble spread for the ozone hole area and ozone deficit. Maximum values exceed the observed range, especially between July and September, indicating an ozone depletion onset too early in the year. The early onset is also represented by the ensemble mean showing more extreme values for the ozone hole area and deficit than the year 2000 observations between July and September. This behavior is also detected for the minimum total ozone column.
Overall, the ICON-ART simulations show a similar development of the characteristics for all sensitivity runs compared with observational data. However, they differ in strength and sub-seasonal development. Compared with observational data, all sensitivity simulations show a prolonged persistence of the Antarctic ozone hole, indicating an unusual

late vortex breakup date in the model. A higher SZA threshold is generally reflected by a larger and deeper ozone hole and, thus, a larger ozone deficit. This result is reasonable as the period of ozone depletion is prolonged with this change in the SZA threshold. The metrics further reflect this change with a shift in the ozone depletion onset.

To further evaluate the impact of different solar zenith angle thresholds, the multi-year monthly mean total column ozone climatology from the NIWA-BS (The National Institute of Water and Atmospheric Research - Bodeker Scientific) total column ozone database and the ERA5 (European Reanalysis, Version 5) reanalysis for the years 1998 - 2002 (Figure 5.2; upper panel) were compared with the ensemble mean climatology for each sensitivity simulation (middle and lower panels).

The NIWA-BS total column ozone database (Bodeker et al., 2020) is a near-global daily dataset for TCO generated from multiple satellite-based measurements. TCO values are available for the period from 31 October 1978 to 31 December 2016 with a resolution of 1.25° longitude by 1° latitude. Satellite measurements are compared with the ground-based Dobson and Brewer spectrometer networks to identify and remove biases and drifts in the satellite data. Afterward, the different satellite measurements are homogenized to obtain a single dataset. In addition, a gap-free dataset was created: the BS-filled dataset. This dataset uses a machine-learning algorithm to fill gaps in the initial dataset. Even though this algorithm allows for a gap-free dataset, the uncertainties are significantly higher for the interpolated regions due to a shortage of measurements. This is particularly the case for polar night, as the satellite measurements are only available during sunlight hours. A detailed description of the database is given by Bodeker et al. (2020).

The ERA5 reanalysis is the current reanalysis dataset produced by the European Centre for Medium-Range Weather Forecasts (ECMWF). ERA5 combines a forecast model (the Integrated Forecasting System (IFS) model) with observational data to generate a complete dataset. It spans the period from 1950 to the present with an hourly output available. Compared to the previous ERA-Interim reanalysis, it has an increased resolution of 31 km horizontally and 137 vertical levels up to 1 hPa. A detailed description is given by Hersbach et al. (2020). The ERA5 reanalysis dataset will be used for various comparisons in this study. For the evaluation of the TCO distribution, monthly mean data were used.

The BS-filled dataset and ERA5 show the same overall structure with low TCO values in the tropics throughout the year and seasonally more variations at higher latitudes. In the Arctic, a winter-spring (December-April) maximum is observed, while in the Antarctic, a minimum is observed between August and December. Further, in the southern hemisphere, a region of high TCO values is observed between 40°S and 60°S that is weakest in summer and shows a maximum strength in spring. While the overall structure is very similar, ERA5 shows higher values in the tropics. Additionally, there are differences in the ozone distribution at high southern latitudes, with the BS-filled dataset showing sig-

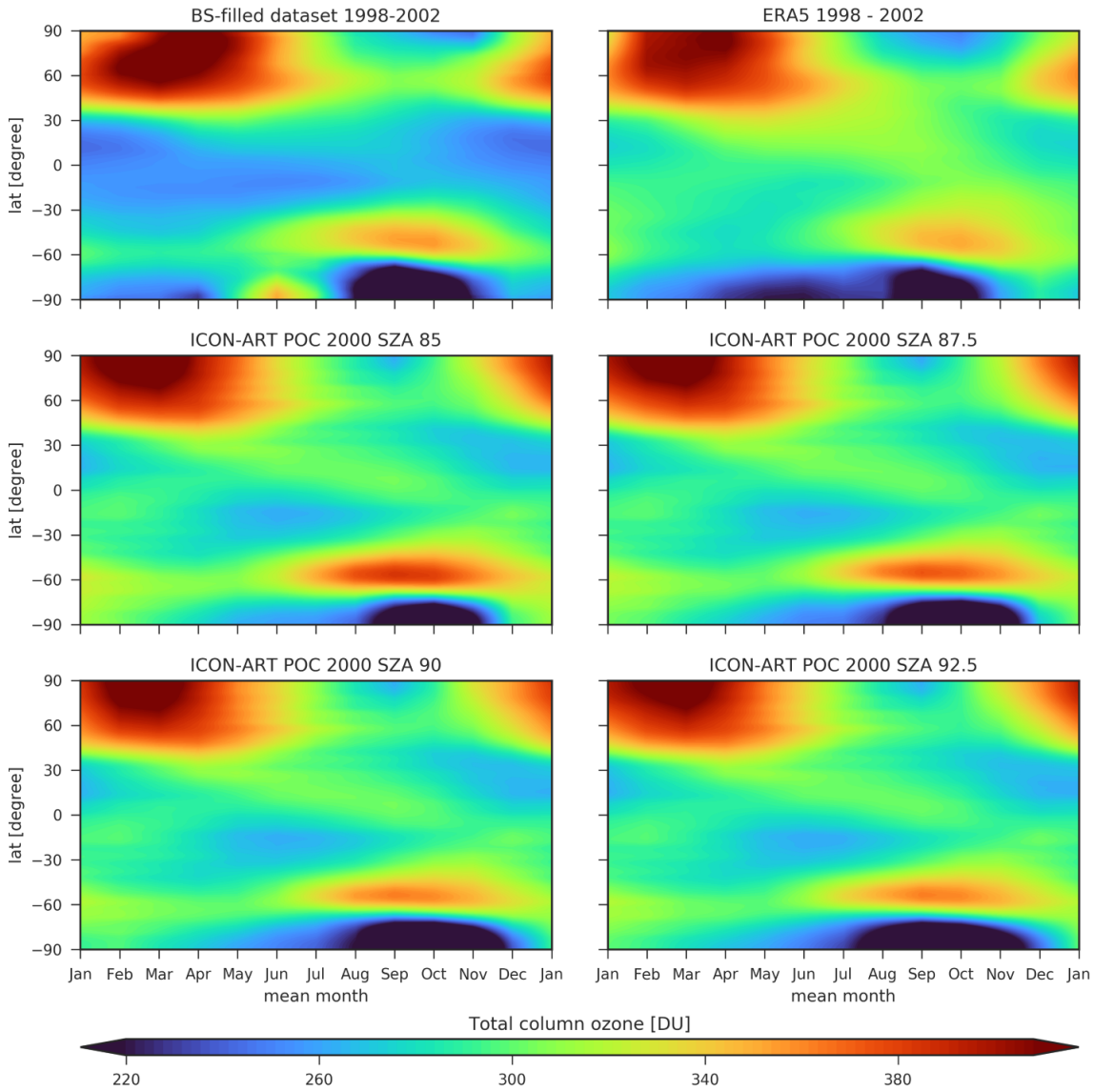

Figure 5.2: Monthly mean zonal mean total column ozone distribution [DU]. Top left panel: BS-filled TCO dataset (1998 - 2002); top right panel: ERA5 (1998 - 2002); middle and lower panels: ICON-ART POC 2000 ensemble mean (25 members) for solar zenith angle thresholds of 85°, 87.5°, 90° and 92.5°

nificantly higher values between May and July. However, uncertainties in those regions in winter are large due to a small number of polar night measurements.

The different ICON-ART sensitivity runs agree well with the overall structure described by the BS-filled dataset and ERA5. The main differences between the runs are found at high southern latitudes regarding the development of the Antarctic ozone hole. For the "SZA 85" and "SZA 87.5" simulations, the development of the ozone hole is limited to high southern latitudes higher than 80°S along with the maximum region in middle latitudes reaching further south with stronger than usual maximum values. The "SZA 90" and "SZA 92.5" simulations show a similar northward extend of the ozone hole reaching approximately 75°S corresponding with a similar strength of the maximum in mid-latitudes

that is comparable with the observations. The two simulations differ in the timing of the ozone hole development, with the "SZA 92.5" simulation showing a depletion onset about one week earlier in late July. The "SZA 90" simulation shows a more realistic ozone depletion onset. However, in this simulation, the ozone hole simulation also persists longer in summer.
With the results from the comparison of ozone hole characteristics and the TCO climatologies, the "SZA 90" simulation was identified as the most realistic simulation, and the SZA threshold was set to 90° for the subsequent studies. While this simulation shows the most realistic representation, the vortex breakup in the ICON-ART simulations is later than observed.

5.2 Climatological total column ozone distributions for the years 1980 and 2000

In the previous section, the ICON-ART simulations with different SZA thresholds were compared with multi-year monthly means of the BS-filled and ERA5 TCO datasets and typical ozone hole characteristics to find the most realistic model setup. The simulations with an SZA threshold of 90° were identified as the best setup and are used subsequently with simulations including 65 ensemble members. Besides the realistic representation of the Antarctic ozone hole, the model's global distribution of TCO is evaluated in this section. The ICON-ART noPOC 1980 ensemble mean is compared to the mean of 1978 - 1982 NIWA-BS, and 1979 - 1982 ERA5 data, while the POC 2000 ensemble mean is compared to the years 1998 - 2002.
The overall structure of the TCO distribution, as described in section 5.1 with minimum values in the tropics and seasonally varying values at higher latitudes, is visible in all datasets and for both time frames (see Figure 5.3). The year 2000 climatology shows globally slightly lower TCO values for all datasets throughout the year. Besides this general ozone reduction, the changes between the years 1980 and 2000 are greatest in high southern latitudes during spring. Here, characteristically low values develop for the year 2000 data: the Antarctic ozone hole. While the datasets' overall structure and development are similar, a few differences can be detected: The ERA5 dataset shows higher TCO values in the tropics. Further, the TCO maximum during June, visible in the BS-filled dataset, cannot be observed here. The ICON-ART simulations show tropical TCO values within the range of the BS-filled dataset and ERA5 values with slightly lower values than ERA5. The minimum at high northern latitudes between August and November is less pronounced in the ICON-ART simulations compared to the BS-filled and ERA5 datasets. Further, for the noPOC 1980 simulation, the southern hemispheric maximum between 40 and 60°S is stronger than in the BS-filled and ERA5 datasets between July and January. Additionally, as already described in section 5.1, the Antarctic ozone hole persists longer

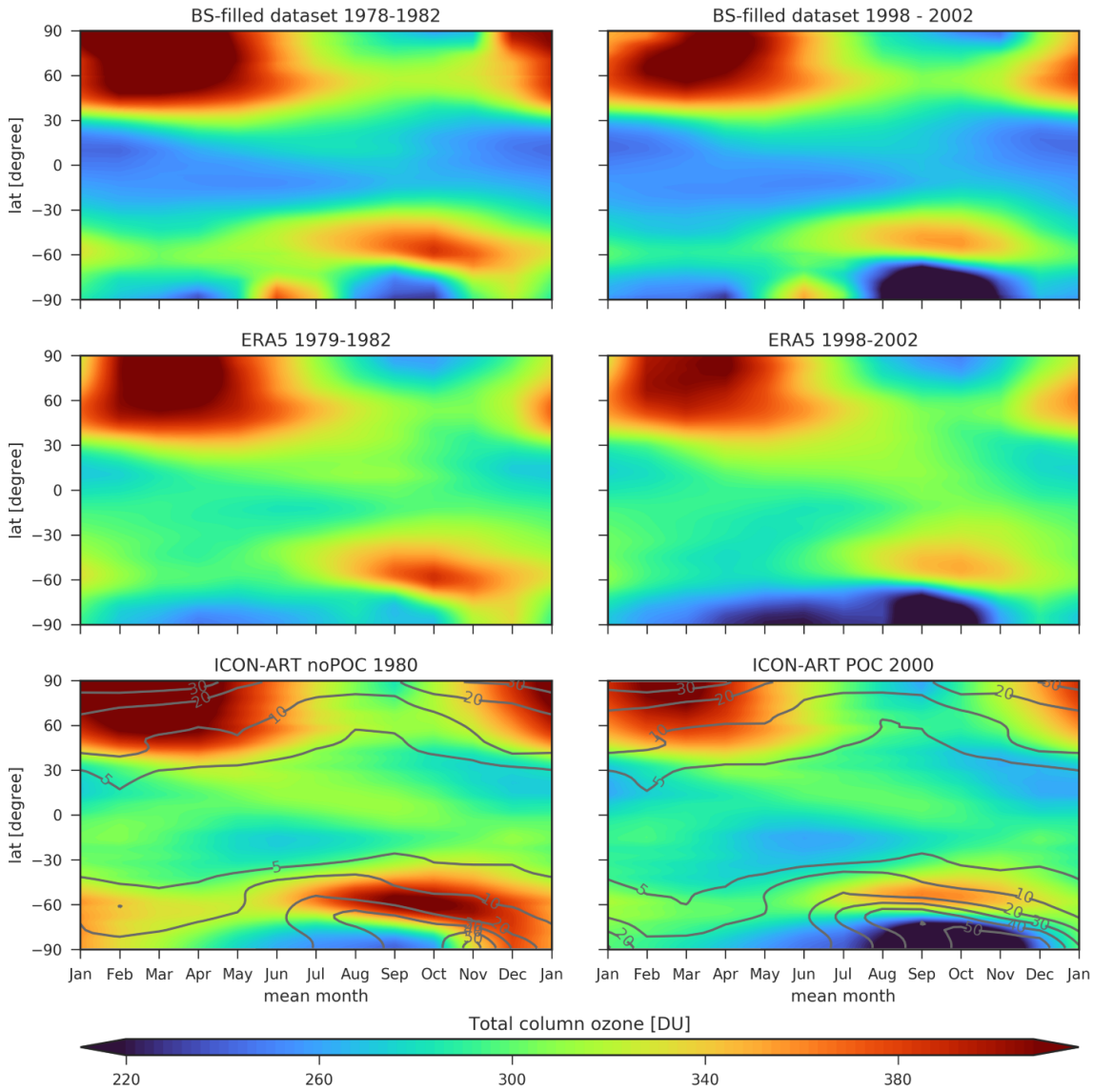

Figure 5.3: Monthly mean zonal mean total column ozone distribution [DU]. Top panels: BS-filled TCO dataset for 1978 - 1982 (left) and 1998 - 2002 (right); middle panels: ERA5 for 1979 - 1982 (left) and 1998 - 2002 (right); lower panels: ICON-ART ensemble mean (65 members) of the noPOC 1980 simulation (left) and the POC 2000 simulation (right). The contour lines shown for the ICON-ART simulations represent the standard deviation of the zonal mean TCO distribution.

in the ICON-ART POC 2000 simulation. Overall, ICON-ART shows an agreement with the BS-filled dataset and ERA5 data regarding global structure and temporal evolution throughout the year and on longer timescales. The differences between ICON-ART and the ERA5 and BS-filled datasets are in the same order of magnitude as the differences between the datasets themselves, except for the already mentioned longer persistence of the Antarctic ozone hole.

5.3 Vertical profiles of ozone and temperature for the years 1980 and 2000

So far, only vertically integrated ozone has been analyzed. In the following section, we assess the model's ability to realistically capture the vertical ozone and temperature structure in the southern hemisphere. Therefore the model results are compared with ozonesonde data at different stations to analyze the model's ability to reproduce the vertical profiles. Ozonesonde data was obtained from the World Ozone and Ultraviolet Radiation Data Centre (WOUDC; WOUDC Ozonesonde Monitoring Community et al., 2015) for selected southern hemispheric stations as summarized in Table 5.1. For comparison with the noPOC 1980 simulation, the stations Aspendale and Syowa were chosen, while for the POC 2000 simulation, a comparison for the stations Broadmeadows, Lauder, Macquarie Island, Neumayer, and South Pole was performed. The noPOC 1980 simulation was compared to sonde data of 1978 - 1982, while the POC 2000 simulation was compared to sonde observations between 1998 and 2002. For Broadmeadows, the comparison was performed with data between 1999 and 2002 due to data availability.

Table 5.1: Ozone sonde stations and corresponding ICON grid points

Name	Coordinates	Period	Coordinates of closest ICON grid point
Aspendale (APL)	38.03°S, 145.10°E	1978 - 1982	38.96°S, 145.35°E
Syowa (SYO)	69.01°S, 39.58°E	1978 - 1982	68.61°S, 39.45°E
Broadmeadows (BRO)	37.68°S, 144.95°E	1999 - 2002	36.98°S, 144.00°E
Lauder (LAU)	45.04°S, 169.68°E	1998 - 2002	45.33°S, 170.54°E
Macquarie Island (MQA)	54.50°S, 158.96°E	1998 - 2002	55.54°S, 159.91°E
Neumayer (NMY)	70.65°S, 8.26°W	1998 - 2002	70.97°S, 7.01°W
South Pole (SP)	89.99°S, 169.00°W	1998 - 2002	88.92°S, 3.54°E

In a first step, the sonde data were interpolated linearly to selected pressure levels corresponding to the ICON pressure levels. Afterward, monthly means were calculated. From those monthly means, seasonal means, maxima, and minima were obtained. This approach was chosen as the number of ozonesonde launches differs between the months and seasons.
For the comparison with the model simulations, the closest ICON grid point for every sonde location was determined. An overview of the ozonesonde stations and the corresponding ICON grid points is given in Table 5.1 and is displayed in Figure 5.4. As for the ozonesonde data, the seasonal means, maxima, and minima of the vertical ozone and

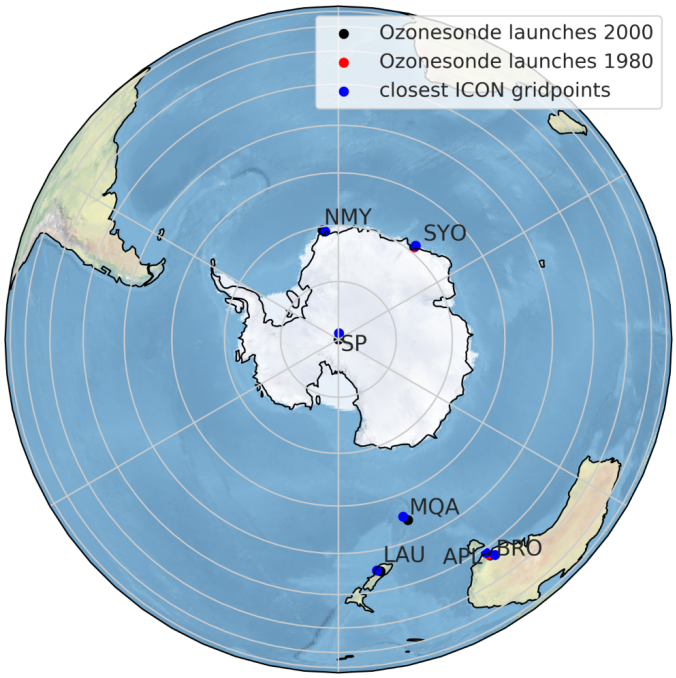

Figure 5.4: Location of ozonesonde launches for the years 1980 (red) and 2000 (blue) and their corresponding closest ICON grid point used for comparison (blue)

temperatures profiles at the corresponding ICON grid points were obtained from monthly mean data. Also, differences are calculated between the sonde data's mean profiles and the ICON-ART simulations at the corresponding grid point. The comparison of vertical ozone profiles at the stations Aspendale and Syowa with the corresponding ICON grid points of the noPOC 1980 simulation is shown in Fig. 5.5.

When interpreting the results, it should be noted that the resulting sonde profile can be obtained from a different number of sonde launches at different levels. Particularly at high levels, the data availability is limited. Therefore the sonde profiles are only displayed up to 5 hPa. Particularly for the 1980 data, abrupt changes in the sonde profiles should be interpreted as changes in the number of underlying sonde launches and the generally sparse amount of available data. Even though those changes illustrate the shortcomings of the comparison, the profiles are shown up to 5 hPa here to hint at the actual profiles. Further, seasonal maxima or minima obtained from monthly mean data can correspond to a single sonde launch if only one launch was made during that month.

The ICON-ART noPOC 1980 simulation generally shows an agreement at the stations Aspendale and Syowa. While the profiles' overall structure is similar, the ICON-ART simulation shows a systematic bias in tropospheric values with significantly lower ozone. The ozone concentration is reduced by at least 50 % below 400 hPa for Aspendale and more than 80 % at Syowa compared to the observations. The reduction is stronger with lower altitude and reaches almost 100 % at all stations and seasons at 1000 hPa. This systematic bias indicates that the chosen tropospheric lifetime of ozone is significantly

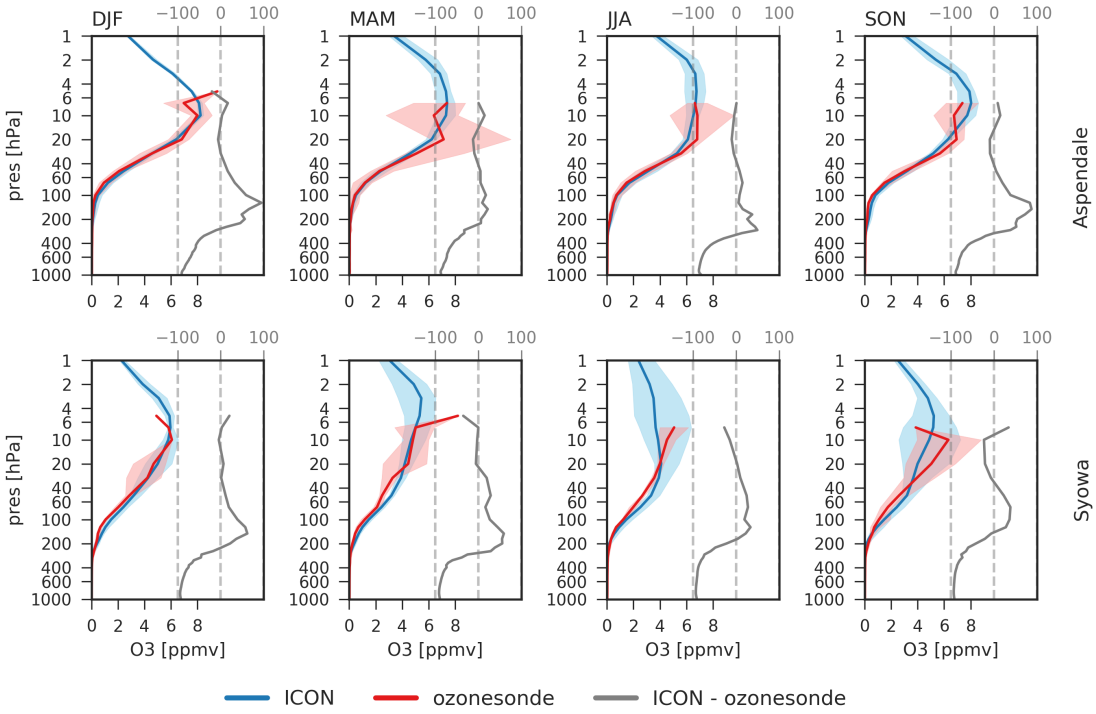

Figure 5.5: Seasonal averaged ozone profiles of the ICON-ART noPOC 1980 simulation (blue) compared to ozonesonde data (red) for Aspendale and Syowa. ICON-ART data is averaged over all ensemble members. Ozonesonde data is averaged over 1978 - 1982. Shading indicates the range of monthly mean values. The grey line indicates the difference between the ICON-ART simulation and the ozonesonde data in percent (based on the ozonesonde profile).

too short, or tropospheric ozone sources and sinks are not represented realistically in the model. Changes in tropospheric lifetime have been investigated in sensitivity studies (see section 6.2.1). Even though an enhanced tropospheric ozone lifetime shifts the model towards slightly increased tropospheric values, significant systematic biases remain (not shown here). Therefore an unrealistic tropospheric source and sink representation is more likely. Further, underestimated tropospheric ozone volume mixing ratios can point to weaker stratosphere-troposphere transport in the model.

However, as already mentioned, the underlying sonde data is limited for the period considered, especially for Syowa. Abrupt changes in the mean profiles and the model spread are detected when a different number of launches are available at different altitudes. This is the case for both stations at levels above 40 hPa and underlines the sparsity of available data. Additionally, the limited amount of data can also impact the observed spread of ozone values. This is the case when a monthly mean value is obtained from a single launch, which enhances the probability of more extreme values. Therefore, a higher spread in the observed data does not necessarily indicate higher internal variability. Similarly, a lower than modeled spread could result from a very limited amount of data. Overall, considering the shortcomings of the comparison, the noPOC 1980 simulation

shows agreement with the observations and hints on a systematic tropospheric bias that could partly be caused by a weaker stratosphere-troposphere transport or an insufficient representation of tropospheric sources and sinks.

The model is further evaluated by comparing the POC 2000 simulation at five different southern hemispheric stations. These stations are characterized by a larger number of launches during the given period and can provide a better indication of systematic biases in the model. While temperature profiles were not available for the year 1980, temperature profiles are available for the year 2000, and their analysis complements the evaluation of vertical ozone profiles. The comparison of vertical ozone profiles is shown in Fig. 5.6, and the comparison of temperature profiles is depicted in Fig. 5.7.

The ozone profiles for Broadmeadows and Lauder show an agreement compared with the sonde data. The comparison at Macquarie Island illustrates slightly higher ozone values in the POC 2000 simulation from December to August in the stratosphere. Similar behavior is seen at the Neumayer and South Pole stations during that time of year. While the ozone values agree well at Macquarie Island during spring (SON), there are larger deviations at Neumayer and the South Pole. At Neumayer, a positive ozone bias of the ICON-ART simulation is detected between 100 hPa and 40 hPa, while a negative bias is visible at levels between 40 hPa and 10 hPa. At the South Pole, the POC 2000 simulation underestimates the ozone concentrations in the stratosphere.

When analyzing the profile of differences, the tropospheric ozone bias detected in the 1980 comparison is also visible here. While the individual manifestations vary, a characteristic bias evolves at low altitudes at all stations and seasons. The occurrence of this pattern strengthens the assumption of an incomplete representation of tropospheric source processes. When analyzing the profile of differences, it should be noted that the difference is expressed as the percentage of the ozone value observed by the sondes. This can lead to the impression of extreme deviations while the absolute difference is small, especially when the observed ozone concentration is small. This is desirable to detect deviations in the troposphere that would otherwise not be visible. However, this also favors the overinterpretation of differences in the lower stratosphere, where ozone values are small compared to higher levels. This is illustrated by the positive ozone bias around 200 hPa that decreases with altitude apparent at different stations and seasons.

In addition to the comparison of the ozone profiles, the temperature profiles are compared (Fig. 5.7). Here, as for the ozone concentrations, Broadmeadows and Lauder show an agreement between sonde data and the ICON-ART simulation. While the modeled temperature structure at Macquarie Island corresponds with the observations, ICON-ART shows a more pronounced tropopause with a slight cold bias visible at all seasons. Further,

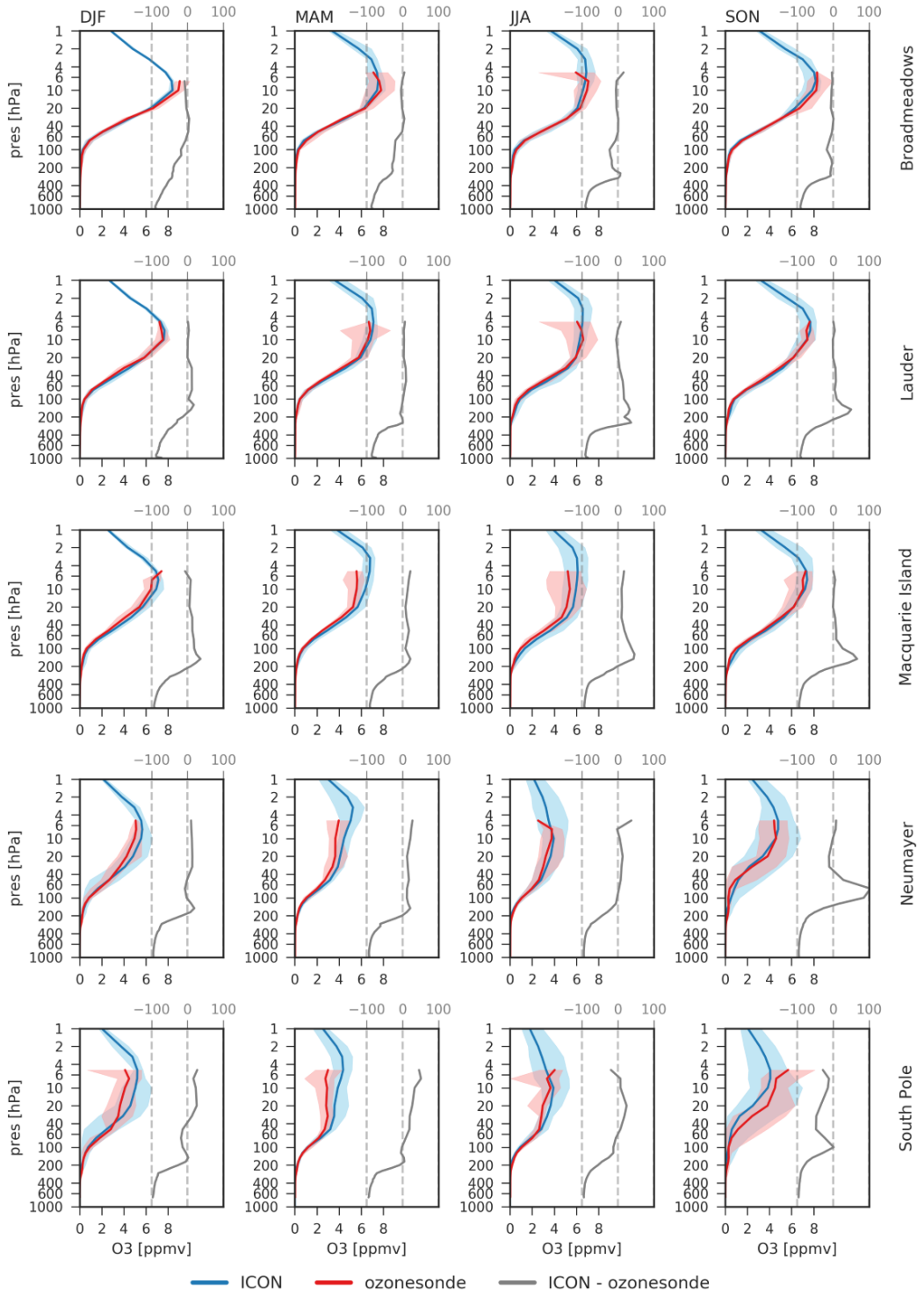

Figure 5.6: Seasonal averaged ozone profiles of the ICON-ART POC 2000 simulation (blue) compared to ozonesonde data (red) for Broadmeadows, Lauder, Macquarie Island, Neumayer, and South Pole. ICON-ART data is averaged over all ensemble members. Ozonesonde data is averaged over 1998 - 2002 (1999 - 2002 for Broadmeadows). Shading indicates the range of monthly mean values. The grey line indicates the difference between the ICON-ART simulation and the ozonesonde data in percent (based on the ozonesonde profile).

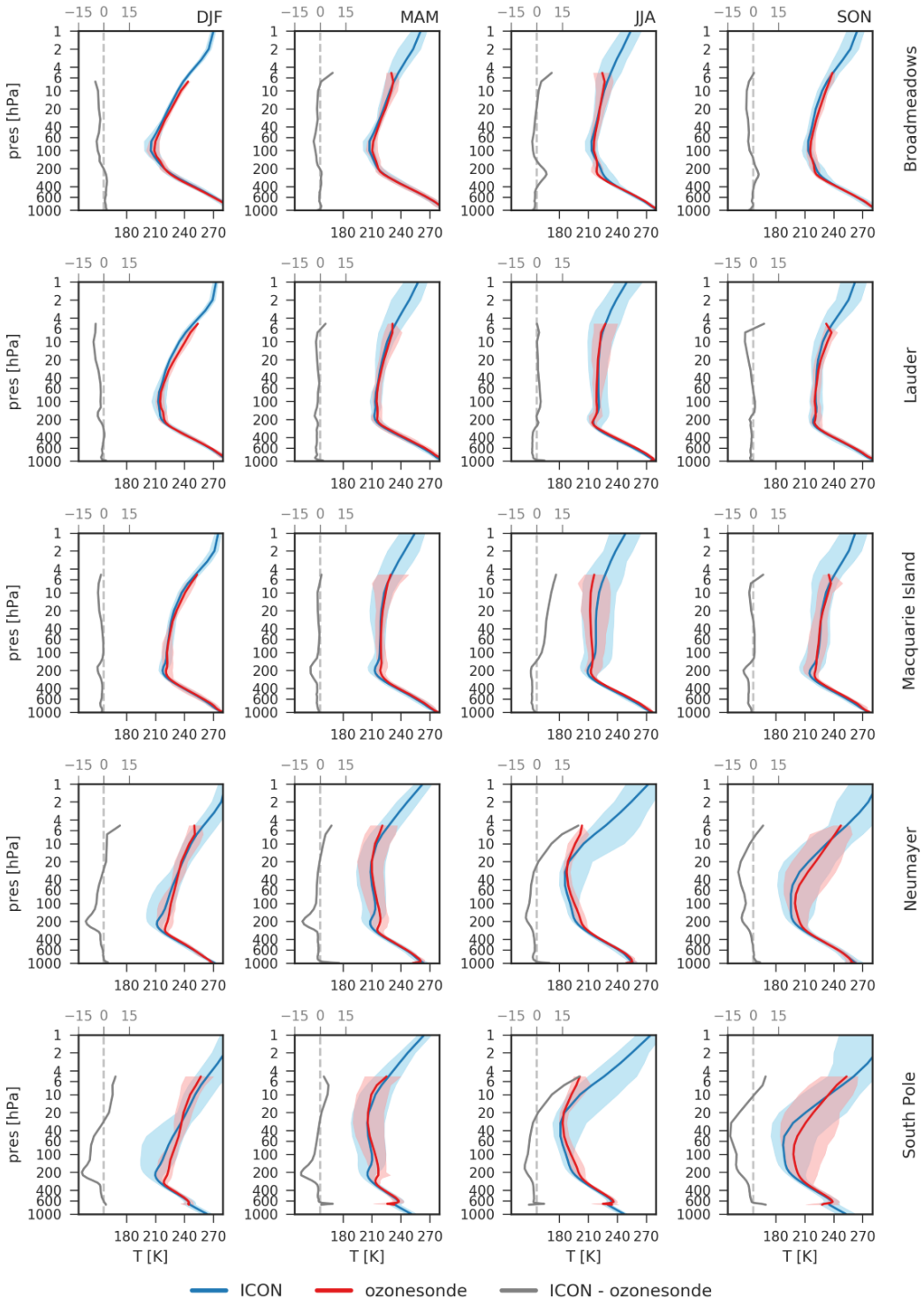

Figure 5.7: Seasonal averaged temperature profiles of the ICON-ART POC 2000 (blue) simulation compared to ozonesonde data (red) for Broadmeadows, Lauder, Macquarie Island, Neumayer and South Pole. ICON-ART data is averaged over all ensemble members. Ozonesonde data is averaged over 1998 - 2002 (1999 - 2002 for Broadmeadows). Shading indicates the range of monthly mean values. The grey line indicates the difference of the ICON-ART simulation and the ozonesonde data.

a warm bias of up to 15 K is evident above 150 hPa in winter. At Neumayer and South Pole, more distinct differences are found. In DJF, MAM, and JJA, a more pronounced, colder tropopause is present in the ICON-ART simulations. This results in a cold bias of up to 5 K up to 20 hPa. In SON, the ICON-ART simulation exhibits significantly colder temperatures up to 10 hPa at both stations. The differences are particularly large at the South Pole. This temperature offset favors a stronger than usual ozone depletion by the polar ozone chemistry representation in the Linoz scheme and could be responsible for the low ozone values in spring. Further, the differences in tropopause temperatures indicate higher static stability of the atmosphere in the model simulations that could weaken the stratosphere-troposphere transport. This could result in the enhanced lowermost stratosphere ozone values detected in the ICON-ART simulations.
Overall, ICON-ART shows an agreement compared with the sonde data apart from some systematic biases. The POC 2000 comparison supports the indication of an insufficient realization of tropospheric ozone sources and sinks as well as weaker stratosphere-troposphere transport caused by a more pronounced tropopause. Other differences can partly be explained by the model's resolution and the resulting distance of the station location and the chosen ICON grid point. Further, the comparability is limited by the experimental design, comparing the results of an ensemble with 65 members with sonde data from five years resulting in significantly lower accuracy. This is visible especially at high altitudes, where more abrupt changes in the mean profiles are visible.

5.4 Conclusions

The comparison of the model's ability to realistically map the climatological ozone distribution shows remarkable skill when considering the simplicity of the underlying chemistry scheme. When comparing the TCO climatology, the model's tendency towards a delayed vortex breakup is visible. However, this behavior is not specific to the ICON-ART model and can be seen in several model studies. The same tendency is visible in some models of the CMIP6 models' evaluation study by Keeble et al. (2020) and the study by Eyring et al. (2006), investigating 13 CCMs. Further, Stone et al. (2016) report a similar development of the Antarctic ozone hole in the ACCESS (Australian Community Climate and Earth System Simulator) model that is run with a reaction-based stratospheric and tropospheric chemistry. In those studies, similar to the ICON-ART results, the maximum ozone concentrations between May and July, seen in the NIWA-BS dataset, are not apparent. The same is the case for the study by Morgenstern et al. (2009), which is, however, showing a realistic vortex breakup in the UKCA model that has a similar chemistry scheme as the ACCESS model.
Stone et al. (2016) also evaluated vertical profiles of ozone concentrations and temperature based on the comparison with sonde data of several southern hemispheric stations.

There, the model's problem with adequately representing the springtime vertical ozone profiles is encountered.
Overall, the ICON-ART climate simulations performed with the Linoz scheme can compete with state-of-the-art climate models. More complex chemistry schemes show similar shortcomings as the ICON-ART simulations with the simplified Linoz scheme and are not necessarily better in mapping climatological ozone concentrations. The evaluation performed in this chapter shows that the Linoz scheme is suited for this kind of modeling study.

6 Simulated southern hemispheric climate change signals

The formation of the Antarctic ozone hole is characterized by a large ozone loss of more than 80 % in the Antarctic lower stratosphere in spring (e.g. Previdi and Polvani, 2014). Due to the radiative properties of ozone as a strong absorber of UV radiation, ozone loss of this extent is expected to influence temperatures in the corresponding altitude range. Randel and Wu (1999) and Thompson and Solomon (2002), indeed reported Antarctic stratospheric temperature changes based on numerous sonde observations between 1970 and 1998. Both studies found a springtime cooling of stratospheric temperatures, coinciding with the season of largest ozone losses, that was interpreted as a result of ozone depletion. Along with the stratospheric cooling, a strengthening of the polar vortex resulting in a delayed vortex breakup was observed (Waugh et al., 1999; Thompson and Solomon, 2002). This strengthening of zonal winds was not limited to the stratosphere but reached down to the troposphere about 1 - 2 months later. The intensification of the zonal wind in the polar troposphere was accompanied by a decrease in strength in the midlatitudes. Consequently, the tropospheric signal is characterized by a poleward shift of the jet, which is commonly referred to as the high-index polarity of the Southern Annular Mode. In addition to the tropospheric circulation changes, warming of the Antarctic Peninsula and Patagonia has been observed as well as a cooling of the remaining Antarctic continent (Thompson and Solomon, 2002).

Even though the occurrence of the observed changes coincides with polar ozone depletion, atmospheric changes in recent decades are not limited to the changes in ODSs and the corresponding development of the Antarctic ozone hole. Another main driver of climate change is the increase of greenhouse gases that is expected to cause a decrease in stratospheric temperatures. Further, the atmospheric system shows high internal variability, and therefore it is difficult to prove the causality between changes in ozone concentrations and the observed stratospheric and tropospheric trends.

As a result, multiple modeling studies have been performed in the past to reconstruct climate change signals and investigate the impact of stratospheric ozone loss compared to the effect of increased GHGs (e.g. Perlwitz et al., 2008; Karpechko et al., 2008, 2010; Son et al., 2008, 2010, 2018; McLandress et al., 2011; Polvani et al., 2011a; Maycock et al., 2018). While the attribution of the stratospheric cooling signal and the prolonged persistence of the polar vortex to polar ozone depletion is supported by all studies, they

differ in the projected strength of circulation changes, particularly for the effect on surface climate.

As stratospheric ozone is expected to recover, a reversal of the circulation changes induced by ozone depletion is assumed. In contrast, the increase of GHGs will strongly affect the climate in the future and is expected to lead to tropospheric warming and stratospheric cooling. Further, increased GHGs are associated with a poleward shift of the midlatitude jet that is associated with a shift of the tropospheric SAM towards higher values. The reversal of ozone hole induced surface climate change signals will thus likely counteract the changes induced by increased GHGs. First observational indications that this is the case have been reported recently by Banerjee et al. (2020). For meaningful future climate simulations, it is therefore important to obtain a detailed characterization of the ozone hole induced climate change signals.

A detailed characterization of the signals requires a clean experimental design, investigating the effects of individual forcings. The above-mentioned studies work with transient simulations where multiple boundary conditions change simultaneously. Thus an attribution of the signal to a single forcing is difficult. Further, transient studies are not able to account for internal variability.

A method to overcome those problems is the timeslice experimental design as described in section 3.4. Here, the boundary conditions for a given year are perpetually applied in the model simulations, and thus, the climate change signals result only from different representations of polar ozone chemistry or different chosen boundary conditions for the simulations that are compared. Further, long timeslice experiments can be used to investigate internal variability. Thompson et al. (2011) stated the importance of more clean model experiments, focusing only on individual effects, particularly as there is a large spread in model formulations as well as a large internal variability. Further, Seviour et al. (2017) proposed that previous intermodel differences could largely be attributed to internal variability and highlighted the importance of either large ensemble sizes or long time slice simulations to quantify intermodel differences accurately. The timeslice approach has been used for several studies in the past years (e.g. Gillett and Thompson, 2003; Polvani et al., 2011b; Staten et al., 2012; Keeble et al., 2014), but the number of experiments with this approach is still comparatively small.

The calculation of long integrations requires a trade-off in model complexity. Thus, most timeslice studies work with prescribed ozone climatologies to investigate the effects of ozone destruction. Keeble et al. (2014) use a comprehensive and interactive calculation of ozone for their timeslice experiments; however, the realization size of 20 years is small in this study.

Here, the results of 65-year long timeslice integrations with an interactive calculation of ozone are presented. The usage of the Linoz scheme enables the realization of a large ensemble size while taking into account chemistry-climate-interactions due to its interac-

tive ozone calculation. The timeslice approach is well suited to investigate the effects of increasing GHGs and polar ozone depletion separately. Further, internal variability can be analyzed in those model simulations, and thus an assessment of the significance and uncertainties of the model results is feasible.

In this chapter, we investigate the climate change signals that are resulting from polar ozone depletion as well as greenhouse gases based on the four model simulations with and without polar ozone chemistry for the years 2000 and 2060, focusing on the southern hemisphere. Signals induced by polar ozone depletion are investigated by the ensemble mean differences between the POC 2000 and noPOC 2000 simulations and between the POC 2060 and noPOC 2060 simulations. For the impacts of increasing greenhouse gases, the differences between the POC 2060 and POC 2000 simulations and between the noPOC 2060 and noPOC 2000 simulations are analyzed. The climate change scenario, taking into account the effects of ozone recovery and increasing greenhouse gases, is analyzed based on the differences between the noPOC 2060 and POC 2000 simulations.

In the following, the temporal and altitude structure of zonal mean climatological changes is analyzed. To focus on the regions affected strongest by the Antarctic ozone hole, the temporal evolution of changes of zonal mean ozone concentrations and temperatures averaged over 90 - 75°S are displayed in Figure 6.1 over the course of the year, as well as the changes in zonal wind averaged over 75 - 50°S. Due to the large differences in ozone concentrations with altitude, ozone changes are described in percent, with the first model simulation as a reference (except for the difference between the noPOC 2060 and POC 2000 simulations). Further, as zonal winds vary between easterlies and westerlies, the wind climatology of the first model simulation is included in the zonal wind differences as contour lines. This enables a better interpretation of zonal wind changes and indicates if changes are corresponding with a weakening or strengthening of the climatological wind speeds. In addition, zonal mean seasonal differences are regarded in the Figures 6.2, 6.3 and 6.4 to get a more detailed picture of the climate change signals. Here, only the cases marked in bold in Fig. 6.1 are discussed.

Comparing the polar cap ozone climatologies of the POC 2000 and noPOC 2000 simulation (Fig. 6.1), seasonally changing ozone concentration differences are visible between 20 and 300 hPa. Those stratospheric changes are significant below 20 hPa. The stratospheric ozone differences are characterized by the onset of strong ozone depletion in the POC 2000 simulation by the beginning of August, leading to a maximum ozone difference of 80 % by October around 60 hPa. While the differences intensify between August and October, a slight descent of the upper and lower boundaries is detected. By the beginning of November, the differences slowly get smaller, starting at upper altitudes. At 200 hPa, a 50 % ozone concentration is visible in February and a 30 % difference persists until June. This development of stratospheric changes is in agreement with the climatology of the Antarctic ozone hole. In the troposphere, the POC 2000 simulation is characterized by

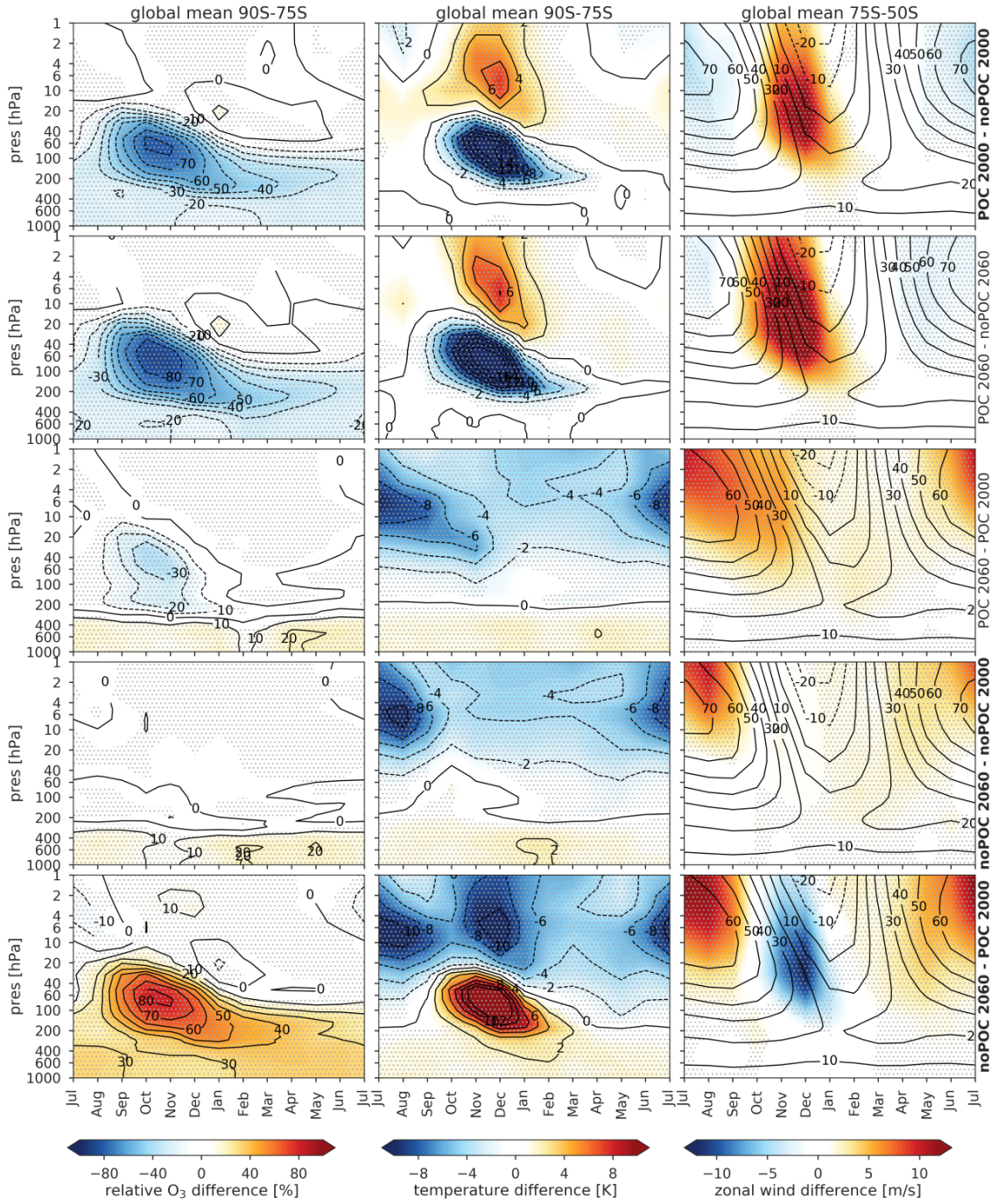

Figure 6.1: Monthly mean relative ozone difference [%] (left panels) and monthly mean temperature difference [K] (middle panels) averaged over 75°S - 90°S and monthly mean zonal wind difference [m/s] (left panels) averaged over 50°S - 75°S for the differences between the POC 2000 and noPOC 2000, POC 2060 and noPOC 2060, POC 2060 and POC 2000, noPOC 2060 and noPOC 2000, and noPOC 2060 and POC 2000 experiments. The percentage of ozone difference is based on the ozone concentration of the first experiment (except for the differences between noPOC 2060 and POC 2000). Contour lines depicted with the zonal wind differences show the zonal wind climatology of the first experiment. Dots represent significance with a false discovery rate of 0.1.

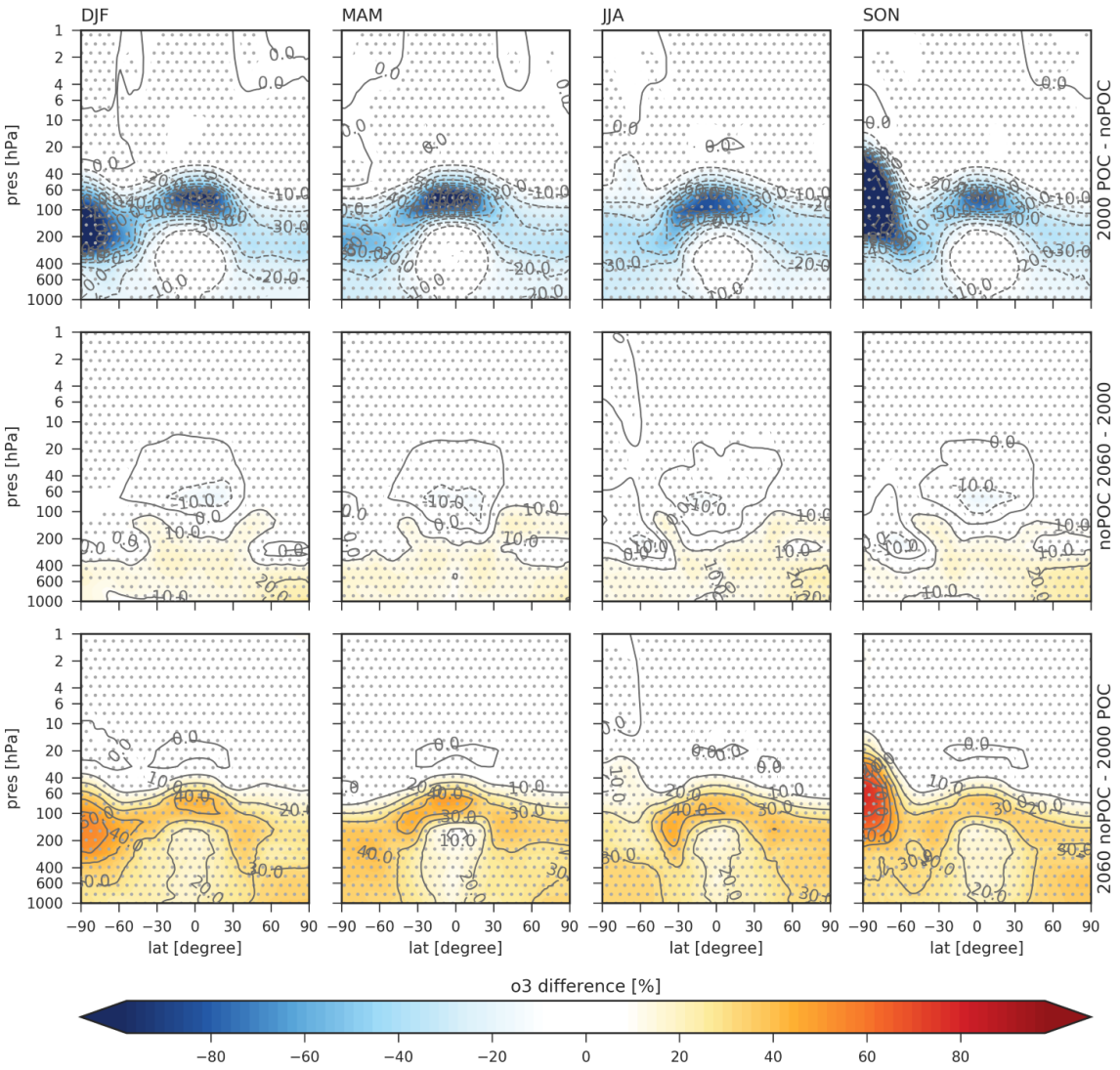

Figure 6.2: Latitude-height cross sections of seasonally averaged relative ozone differences [%] between POC 2000 and noPOC 2000, noPOC 2060 and noPOC 2000, and noPOC 2060 and POC 2000. Dots represent significance with a false discovery rate of 0.1. Percentage is based on the first experiment except for the differences between noPOC 2060 and POC 2000.

around 20 % lower ozone concentrations than the noPOC 2000 simulation. However, as already identified in chapter 5, tropospheric ozone is significantly too low in the ICON-ART simulations. Thus, very small changes in ozone can lead to a high percentage of concentration changes.

The ozone hole induced polar cap temperature differences show a significant temperature decrease in the POC 2000 simulation compared to the noPOC 2000 simulation, matching the temporal and spatial extent of the ozone hole. Temperatures are significantly lower in the POC 2000 simulation between October and February between 200 and 20 hPa, reaching a minimum of more than 16 K in December.

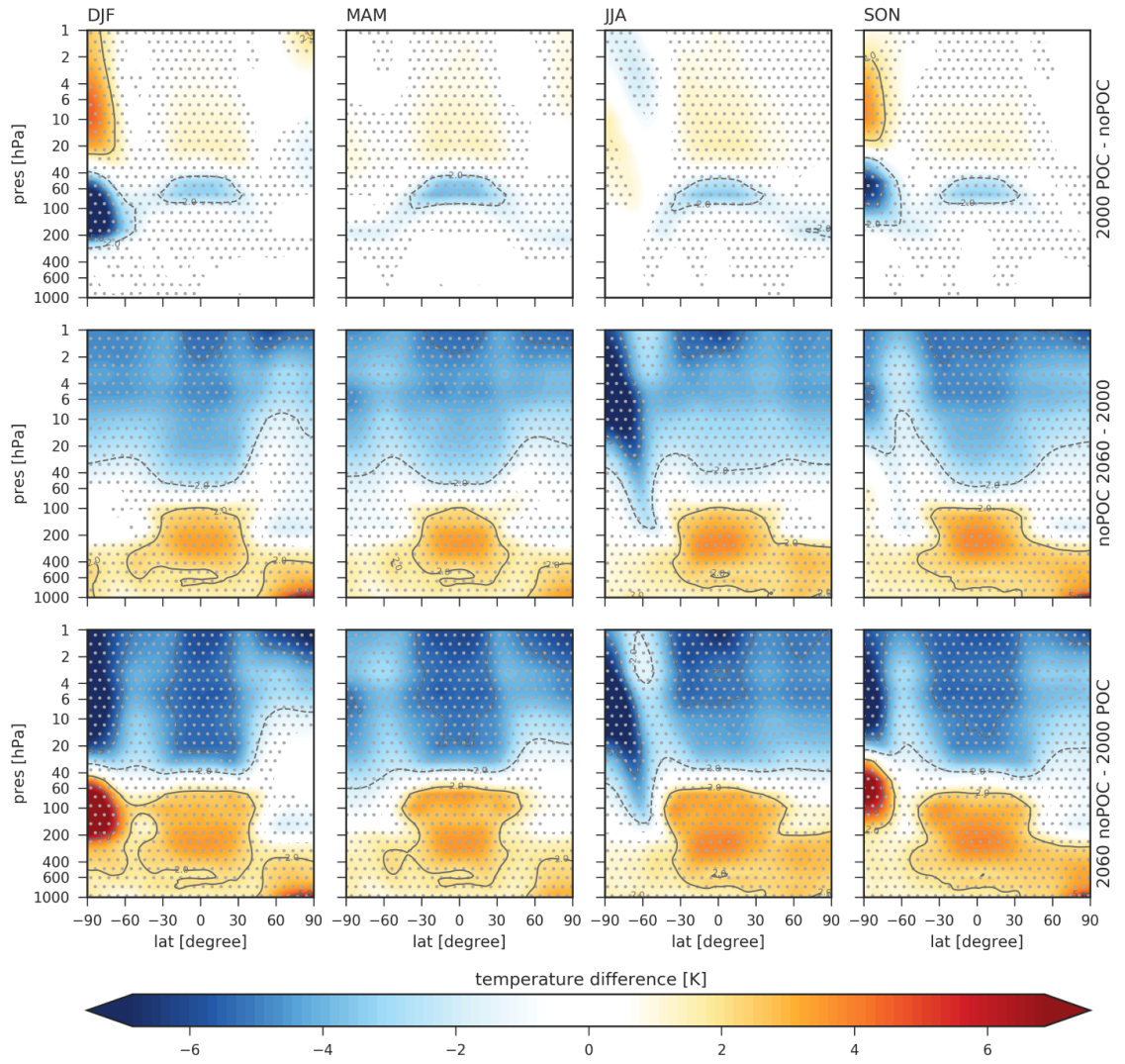

Figure 6.3: Latitude-height cross sections of seasonally averaged temperature differences [K] between POC 2000 and noPOC 2000, noPOC 2060 and noPOC 2000, and noPOC 2060 and POC 2000. Dots represent significance with a false discovery rate of 0.1.

The lower temperatures detected in the POC 2000 simulation are caused by the radiative feedbacks of polar ozone depletion. Stratospheric ozone absorbs incoming solar radiation resulting in enhanced temperatures. The lack of ozone is therefore associated with colder temperatures. This radiative cooling of the Antarctic lower stratosphere was detected by numerous observational and modeling studies investigating the impact of ozone depletion on climate (e.g. Randel and Wu, 1999; Thompson and Solomon, 2002; Maycock et al., 2018). At higher levels, a significantly enhanced temperature reaching up to 6 K is visible for the POC 2000 simulation between October and February. Similar warming was previously observed by Keeble et al. (2014) and identified to result mainly from changes in dynamical heating. Further, changes in the local radiation budget could contribute to the detected temperature changes.

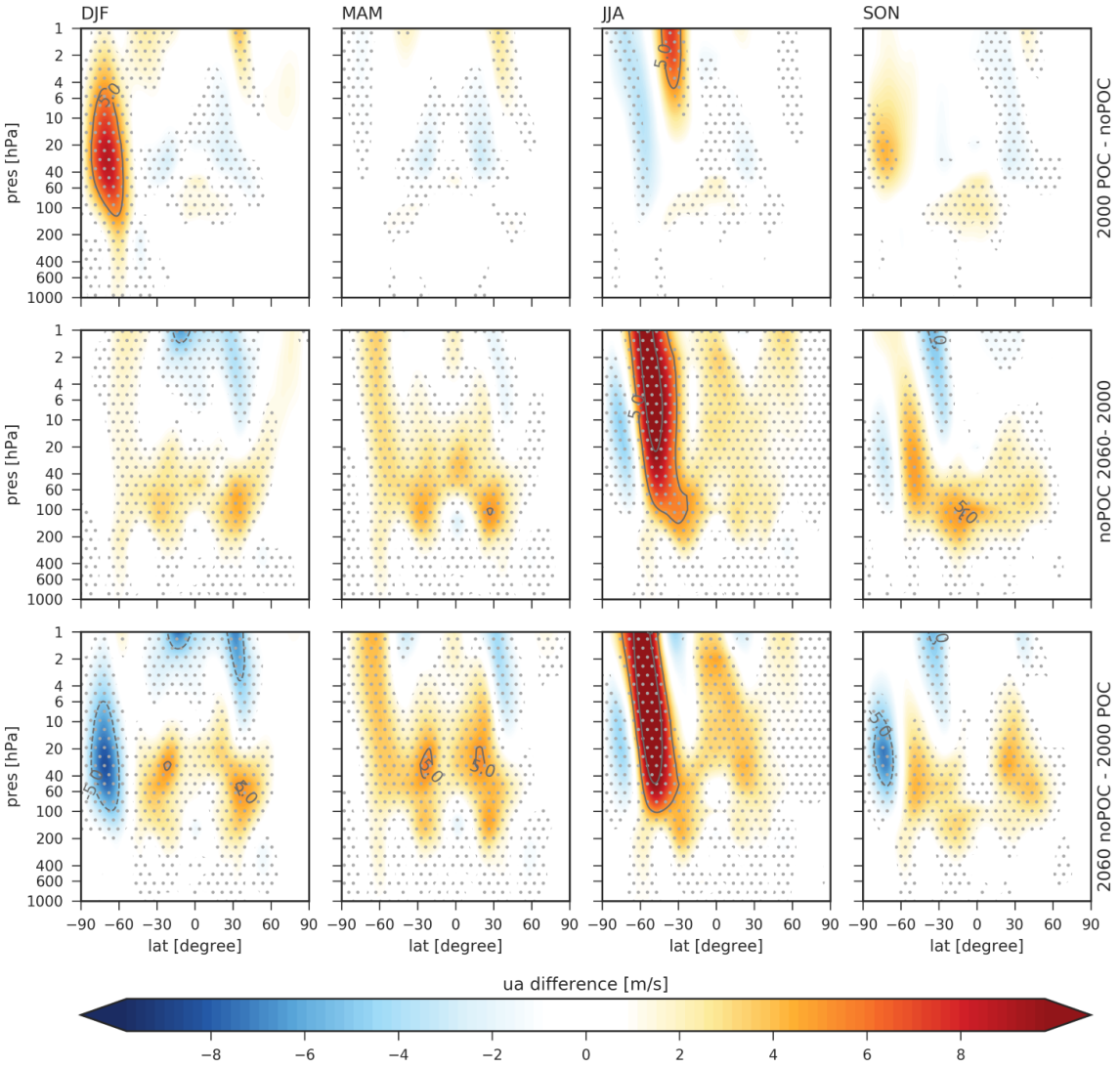

Figure 6.4: Latitude-height cross sections of seasonally averaged zonal wind differences [m/s] between POC 2000 and noPOC 2000, noPOC 2060 and noPOC 2000, and noPOC 2060 and POC 2000. Dots represent significance with a false discovery rate of 0.1.

Additionally to the changes in spring and summer, small, non-significant temperature differences are visible during winter between the POC 2000 and noPOC 2000 simulations with a temperature increase between 60 and 6 hPa, and a slight decrease above. These temperature changes cannot be explained by the visible ozone changes and are dynamically driven, as no sunlight is available during that time of the year.

Investigating the changes in zonal wind averaged over 75 - 50°S, differences are largest between October and January with significantly stronger westerlies of more than 10 m/s in the POC 2000 simulation, particularly between 100 and 4 hPa. These changes are the consequence of the thermal wind response to the detected temperature changes, consistent with the findings of previous studies (e.g. McLandress et al., 2011). The detected stronger westerlies indicate a longer persistence of the polar vortex and a later transition to easterlies in the mid-latitudes. Significant changes are also found in the troposphere between

December and February and are associated with a downward propagation of stratospheric zonal wind changes. Further, slightly lower wind speeds of 2 m/s are found in the stratosphere between May and September for the POC 2000 simulation, indicating a weaker polar night jet. This weakening of the jet is corresponding with weaker latitudinal temperature gradients and, therefore, with the detected temperature dipole pattern.
The zonal mean seasonal ozone differences between the POC 2000 and noPOC 2000 simulations (Fig. 6.2) show the largest changes outside the southern polar region in the tropical tropopause region. The lower ozone concentrations here are possibly caused by the polar ozone loss term in the Linoz scheme that was not limited to polar latitudes. The tropical tropopause is typically located above 10 km, and the appearance of low temperatures in this region could potentially lead to the activation of the polar ozone loss term and thus result in lower ozone concentrations. The detected tropical ozone changes correspond with lower temperatures in the tropical lowermost stratosphere and enhanced temperatures above (Fig. 6.3). This temperature pattern is likely caused by the radiative feedback induced by the ozone changes.
Climatological changes between the POC 2060 simulation and the noPOC 2060 simulation are very similar to the changes visible between the POC 2000 and noPOC 2000 simulations. Therefore the analysis is limited to the monthly mean zonal mean changes averaged over the polar cap for ozone and temperature changes and over the midlatitudes for zonal wind changes (Fig. 6.1). The temporal evolution of the ozone differences between the POC 2060 and noPOC 2060 simulations is similar to the differences for the year 2000. However, the ozone differences for 2060 are larger than for 2000. This stronger ozone loss in the POC 2060 simulation is likely caused by a more efficient ozone depletion due to decreased stratospheric temperatures that are resulting from increased GHGs. The increased ozone loss corresponds with a lower temperature minimum between November and January and a higher temperature maximum at upper levels. Consequently, consistent with thermal wind balance, the intensification of the westerlies is stronger than for the POC 2000 and noPOC 2000 difference between October and January, indicating a longer persistence of the vortex and a later transition to easterlies. The larger stratospheric wind response induces a larger tropospheric response, with an increased period of significant zonal wind changes.
The differences between the noPOC 2060 and noPOC 2000 simulations (Fig. 6.1) show slightly smaller polar cap ozone concentrations for 2000, reaching up to 10 % in the stratosphere and larger deviations in the troposphere. Here, a significant enhancement of up to 20 % is visible throughout the year. The temperature differences are characterized by significant tropospheric warming and significant stratospheric cooling for the noPOC 2060 simulation. Those temperature changes are expected due to the increased greenhouse gas boundary conditions. In addition to the overall stratospheric cooling, a particularly strong cooling pattern is visible between June and September, with colder temperatures between

20 and 1 hPa. Those temperature changes correspond with a significant intensification of the polar vortex between May and September at levels above 10 hPa. Further, a small increase in stratospheric wind speeds is visible throughout the year, with significance from January to September.

The zonal mean seasonal ozone differences between the noPOC 2060 and noPOC 2000 simulations (Fig. 6.2) show globally enhanced tropospheric ozone of approximately 10 % for the noPOC 2060 simulation. The increase is stronger in the Arctic, reaching between 20 and 30 % from winter to summer. Additionally, a small decrease in the tropical lowermost stratosphere is detected throughout the year. The seasonal temperature differences (Fig. 6.3) show a global tropospheric temperature increase of around 1.5 - 3 K and a stratospheric decrease of around 3 K for the noPOC 2060 simulation, as already identified for the southern polar region. As for tropospheric ozone changes, the tropospheric temperature increase is particularly strong in the Arctic and reaches a maximum of more than 5 K in northern hemisphere winter (DJF). Differences in zonal wind (Fig. 6.4) show a more complex pattern of decreases and increases. The most prominent pattern is the intensification of the southern midlatitude jet by up to 10 m/s in winter for the noPOC 2060 simulation. This is in conjunction with a general positive wind difference in the southern hemisphere mid-latitudes throughout the year. Further, a tendency towards stronger tropospheric westerlies is found in the subtropics for the noPOC 2060 simulation.

The differences between the POC 2060 and POC 2000 simulations resemble the noPOC changes. However, the changes in polar cap ozone concentrations differ (Fig. 6.1), with an additional stratospheric ozone loss up to 30 % between August and December for levels between 10 and 200 hPa for the POC 2060 simulation. This can be explained by more effective ozone depletion and, therefore, a stronger ozone hole due to the colder stratospheric temperatures. This ozone change is also reflected by the polar cap temperature changes, showing a more persistent stratospheric temperature minimum than for the noPOC simulations. The zonal wind differences show a stronger increase between September and December, indicating a longer persistence of the polar vortex due to the stronger ozone depletion.

The differences between the noPOC 2060 and the POC 2000 simulations provide insights on the atmospheric response to the combined effects of increased greenhouse gases and stratospheric ozone recovery. Polar cap ozone changes (Fig. 6.1) are characterized by a significant increase of ozone at levels between 10 and 200 hPa between August and April due to ozone recovery for the noPOC 2060 simulation. Additionally, significantly enhanced tropospheric values are visible, matching the enhancements detected for increased GHGs and the reverse effect of differences caused by ozone depletion. The polar cap temperature differences reflect the ozone changes with significantly enhanced temperatures in the noPOC 2060 simulation, reaching maxima of more than 12 K for the duration and altitude range where ozone depletion occurred in the POC 2000 simulation. At higher lev-

els, a significant temperature decrease up to 10 K is visible, reversing the effect detected in the ozone depletion comparisons. Additionally, between May and September, the additional cooling structure identified in the differences associated with increased GHGs is found. A significantly strengthened vortex is detected between April and October in the noPOC 2060 simulation. Even though the vortex is strengthened in winter, its persistence is lower, as indicated by the significant negative wind differences between October and January. Overall the detected signal is influenced mostly by increasing GHGs between March and September, while the influence of ozone recovery is strongest between October and January. This behavior is also visible in the seasonal zonal mean differences.

6.1 Stratospheric impact on surface climate

Stratospheric circulation changes induced by the ozone hole can affect surface climate. As detected in the previous sections, climatological changes in zonal wind can penetrate down to the surface, where they result in circulation and temperature changes. Further, increasing GHGs are projected to cause tropospheric warming and influence tropospheric circulation due to changes in the polarity of the Southern Annular Mode. In this chapter, we investigate the stratospheric impact on surface climate induced by the ozone hole and increased greenhouse gases.

6.1.1 Impacts of polar ozone depletion

Comparing the near-surface pressure of the POC and noPOC simulations (Fig. 6.5), changes are most pronounced in summer for the 2000 as well as the 2060 simulations. The dominating pattern is a dipole of significantly decreased surface pressure of 1 - 4 hPa between 90 and 60°S and significantly increased pressure of up to 3 hPa between 60 and 30°S. The decrease is stronger in West Antarctica, the Antarctic Peninsula, and the surrounding Southern Ocean and weaker in East Antarctica for both time horizons. The pressure increase surrounding Antarctica is similar in strength; however, differences in the location of maxima and minima occur. For the differences between POC 2000 and noPOC 2000, local minima are visible around 60°E, 60°W, and 140°W. For the differences between the 2060 simulations, the structure is shifted with minima around 30°E, 140°E, and 90°W. The changes during all other seasons are substantially smaller and show less significance for both time horizons. Additionally, no matching patterns are detected for the 2000 and 2060 simulations. This indicates a higher internal variability and a limited effect of stratospheric changes on surface pressure during those seasons.
Ozone hole induced changes in near-surface zonal wind (Fig. 6.6) mirror the changes detected in near-surface pressure. The season with the largest differences is summer with a significant intensification of westerlies of up to 1.5 m/s between 70 and 50°S and a significant decrease in wind speeds of about 1 m/s between 50 and 30°S for the POC 2000

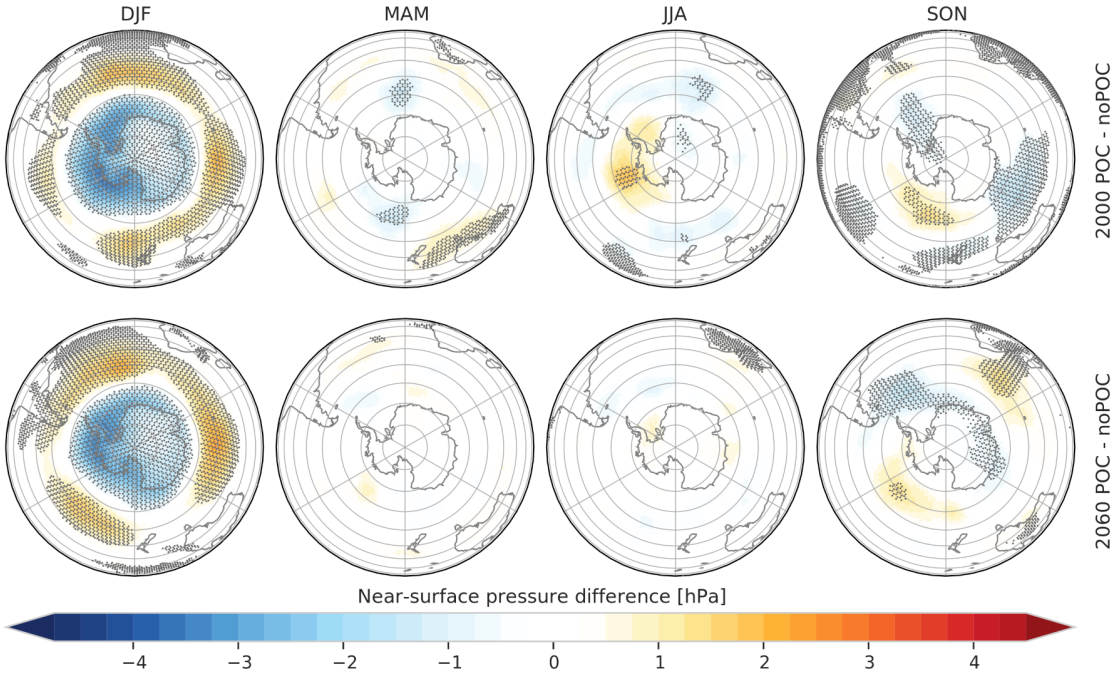

Figure 6.5: Seasonal mean near-surface pressure difference [hPa] between POC 2000 and noPOC 2000, and POC 2060 and noPOC 2060. Dots represent significance with a false discovery rate of 0.1.

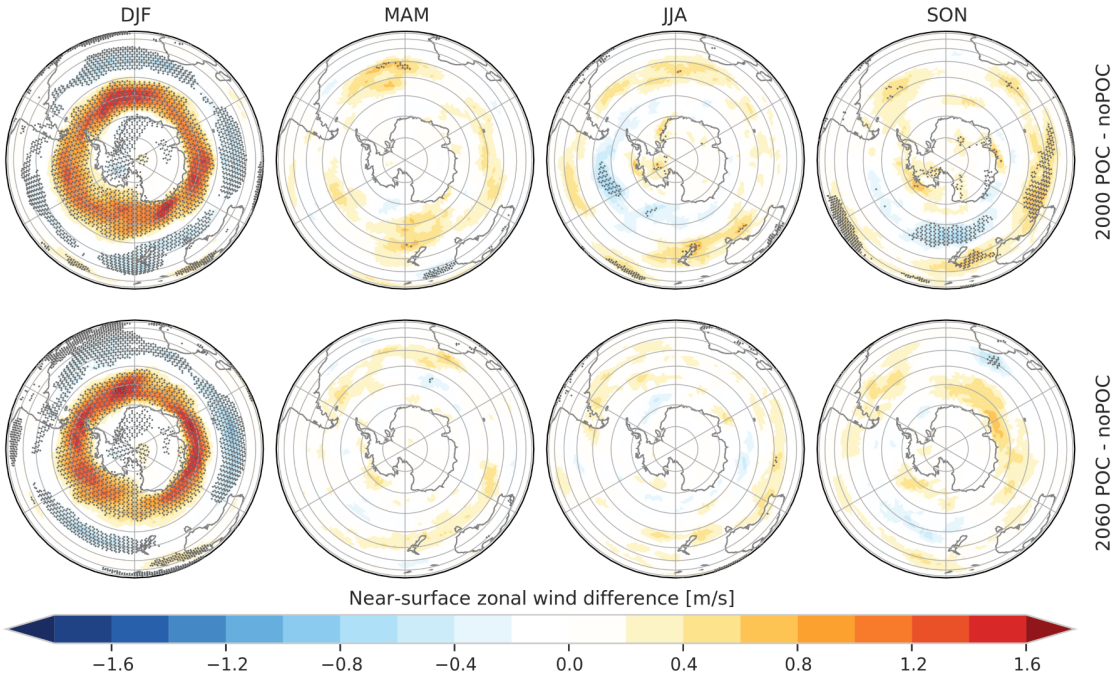

Figure 6.6: Seasonal mean near-surface zonal wind difference [m/s] between POC 2000 and noPOC 2000, and POC 2060 and noPOC 2060. Dots represent significance with a false discovery rate of 0.1.

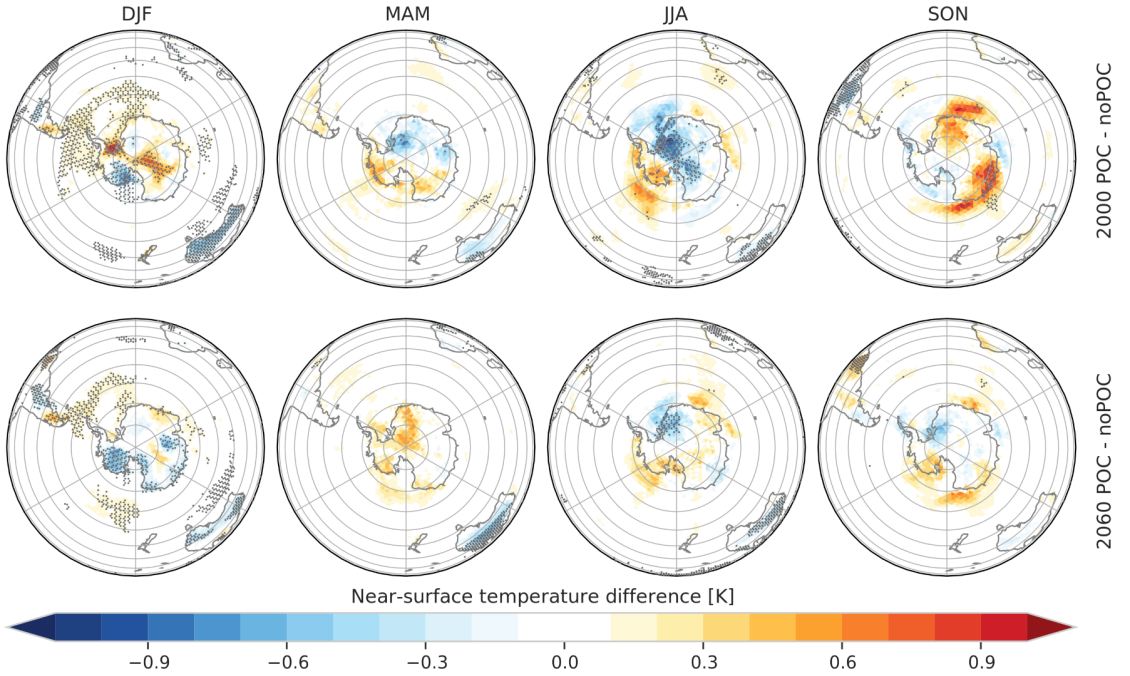

Figure 6.7: Seasonal mean near-surface temperature difference [K] between POC 2000 and noPOC 2000, and POC 2060 and noPOC 2060. Dots represent significance with a false discovery rate of 0.1.

and POC 2060 simulations. This pattern shows the poleward shift of the midlatitude jet for the POC simulations that is associated with the high-index polarity of the SAM. Changes in zonal wind during all other seasons are significantly lower and show little significance.

The temperature changes associated with polar ozone depletion (Fig. 6.7) are more complex than the patterns detected for near-surface pressure and zonal wind changes. As for pressure and zonal wind differences, the number of significantly changed grid points is highest in summer. Then, for the differences between POC 2000 and noPOC 2000, significant warming of up to 0.5 K around the Antarctic Peninsula and the surrounding Southern Ocean (between 80 and 50°S and 0 and 120°W) is visible. Additionally, a complex warming and cooling pattern is visible throughout Antarctica with a significant cooling of 0.7 K of West Antarctica and a contrasting warming pattern along 120°E in East Antarctica, reaching 0.6 K. The strongest warming is detected for the Filchner-Ronne ice shelf with an increase of more than 1 K. At lower latitudes, a temperature decrease is detected in the southern half of Australia, a temperature increase is visible in New Zealand, and warming and cooling patterns are found in South America.

The differences between POC 2060 and noPOC 2060 show slightly weaker near-surface temperature changes in summer with warming and cooling patterns, similar to the ones identified for 2000. The warming around the Antarctic Peninsula is, however, limited to 0 to 90°W. Further, the warming apparent around 120°E is not significant for the differences between the 2060 simulations. The cooling and warming patterns throughout the rest of

Antarctica have the same sign as for the 2000 simulations, while the strength of the signal varies and displays a stronger cooling along coastal areas of Antarctica between 60 and 180°E.

During all seasons except summer, the near-surface temperature changes between the 2060 simulations are small, and the significance is limited to specific regions. Generally, the magnitude of near-surface temperature changes is smaller for the 2060 simulations than for the 2000 simulations, indicating a weaker influence of polar ozone depletion on the surface. Temperature changes between the 2000 simulations in autumn, winter, and spring also show less significant grid points than for summer. Significant changes are visible in winter with a strong cooling around the South Pole and a warming of the Antarctic Peninsula and West Antarctica and in spring with warming at coastal areas of most of East Antarctica. However, the detected changes are confined to smaller regions and are not resembled by the differences between the 2060 simulations to the same degree as the pattern detected for summer. Therefore it is more likely that the signals in winter and spring are generated by internal variability than induced by stratospheric polar ozone chemistry changes. This assumption is further evaluated in section 6.2.1 where the influence of tropospheric ozone lifetimes on the surface temperature signal is analyzed.

6.1.2 Impacts of greenhouse gases

In the following section, the influence of increased greenhouse gases on surface climate is assessed by the differences between the POC 2060 and POC 2000 simulations and between the noPOC 2060 and noPOC 2000 simulations.

Near-surface pressure changes associated with increasing GHGs (Fig. 6.8) are similar for the POC and noPOC differences and show a high number of significant grid points throughout the year and only a weak seasonal cycle. Generally, the pressure changes are characterized by a significant pressure decrease of 1 - 3 hPa south of 50 to 60°S, with the exception of East Antarctica, and a significant pressure increase of 1.5 - 3 hPa at lower latitudes for the 2060 simulations. For the differences between noPOC 2060 and noPOC 2000, from spring to autumn a significant pressure increase of about 1 hPa is apparent in East Antarctica. The differences between the POC 2060 and POC 2000 simulations show a weaker pressure increase for East Antarctica in summer and a stronger pressure increase in autumn. The near-surface pressure changes at lower latitudes in the noPOC differences show a pattern of increased and decreased pressure with three maxima and minima that are shifting in longitude. A similar pattern is visible for the POC differences. In winter, both comparisons show decreased pressure in the polar region that is extending further northward and is more zonally uniform than for the other seasons.

Changes in the near-surface zonal wind (Fig. 6.9) correspond to the pressure changes and are characterized by significantly increased zonal wind speeds of up to 2 m/s from

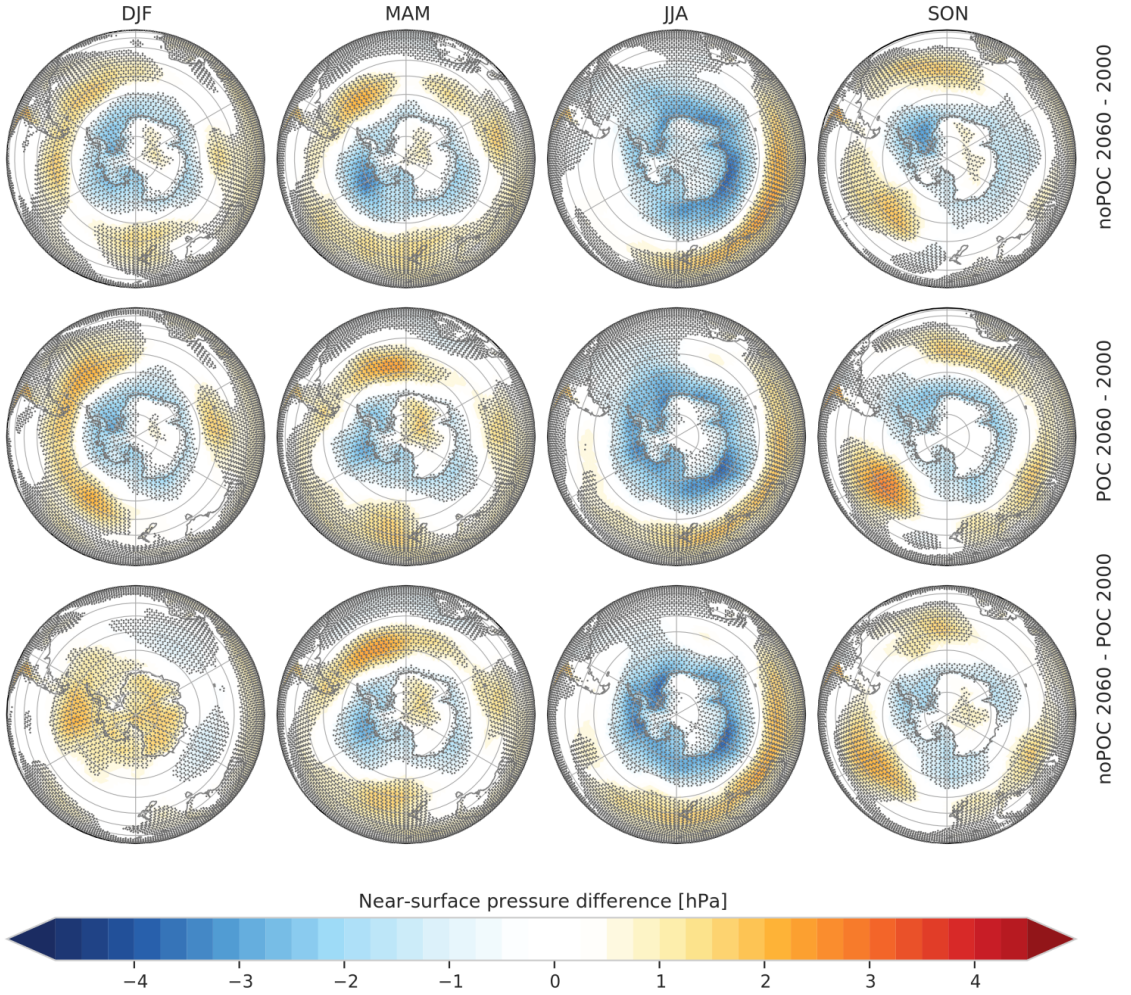

Figure 6.8: Seasonal mean near-surface pressure difference [hPa] between noPOC 2060 and noPOC 2000, POC 2060 and POC 2000, and noPOC 2060 and POC 2000. Dots represent significance with a false discovery rate of 0.1.

70 - 50°S and slightly decreased zonal winds by 0.5 -1 m/s at lower latitudes. As already noticed for the pressure changes, the signal is zonally highly variable and shifted to the north in winter.

The greenhouse gas induced near-surface temperature signals (Fig. 6.10) are characterized by a significant warming of the southern hemisphere of about 1.5 K throughout the year for the 2060 simulations. The signals are very similar for the POC and noPOC differences. South of 60°S, a seasonal cycle is detected with largest changes over the Southern Ocean. Here, a strong increase of more than 3.5 K is detected in the Weddell Sea in autumn, a strong increase of similar magnitude between 180°W - 60°E is visible in winter. In spring, a temperature increase of around 3 K is visible between 0 - 60°E. The signal is smallest in summer around western Antarctica, with a temperature increase of less than 0.5 K. The temperature signal detected for the Antarctic continent differs less strongly around the year. Here, the strongest warming occurs in summer and autumn in

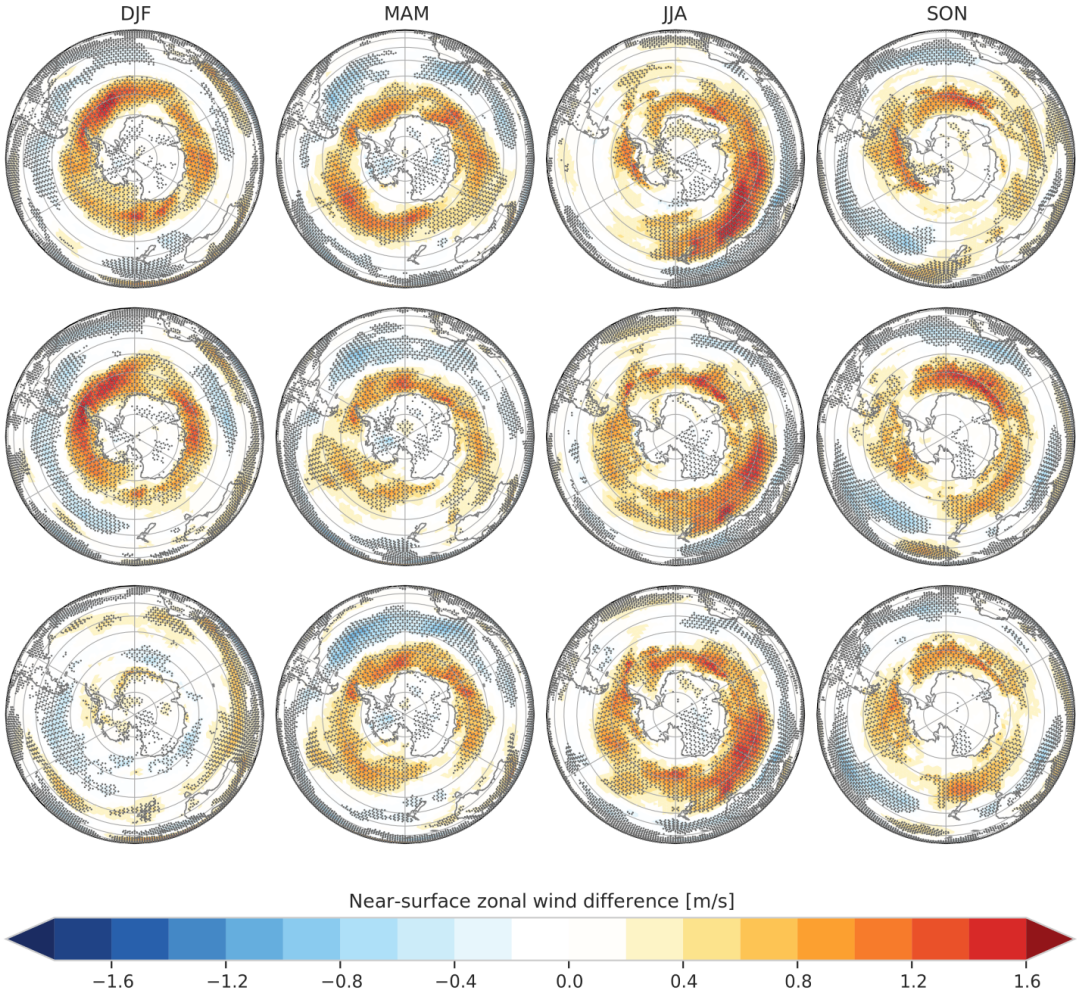

Figure 6.9: Seasonal mean near-surface zonal wind difference [m/s] between noPOC 2060 and noPOC 2000, POC 2060 and POC 2000, and noPOC 2060 and POC 2000. Dots represent significance with a false discovery rate of 0.1.

East Antarctica, and the strongest warming of West Antarctica is detected in winter in the differences between noPOC 2060 and noPOC 2000. While the temperature changes differ only slightly between the POC and noPOC simulations for ocean grid points, larger differences occur for the Antarctic continent. The POC simulations show a weaker temperature increase for spring and summer and a stronger increase that is shifted towards the South Pole during autumn.

Comparing the evolution of temperature changes with changes in pressure and zonal wind speeds, a higher seasonal variability in temperature changes is revealed. This hints at changes that are not only induced by the changes in near-surface circulation. The strong signals in the Southern Ocean indicate the influence of changes in sea surface temperatures. In Figure 6.11 seasonal means of the prescribed changes in sea surface temperatures between 2060 and 2000 are displayed. Comparing the patterns displayed here with the changes in near-surface temperature, a strong resemblance becomes apparent, indicating

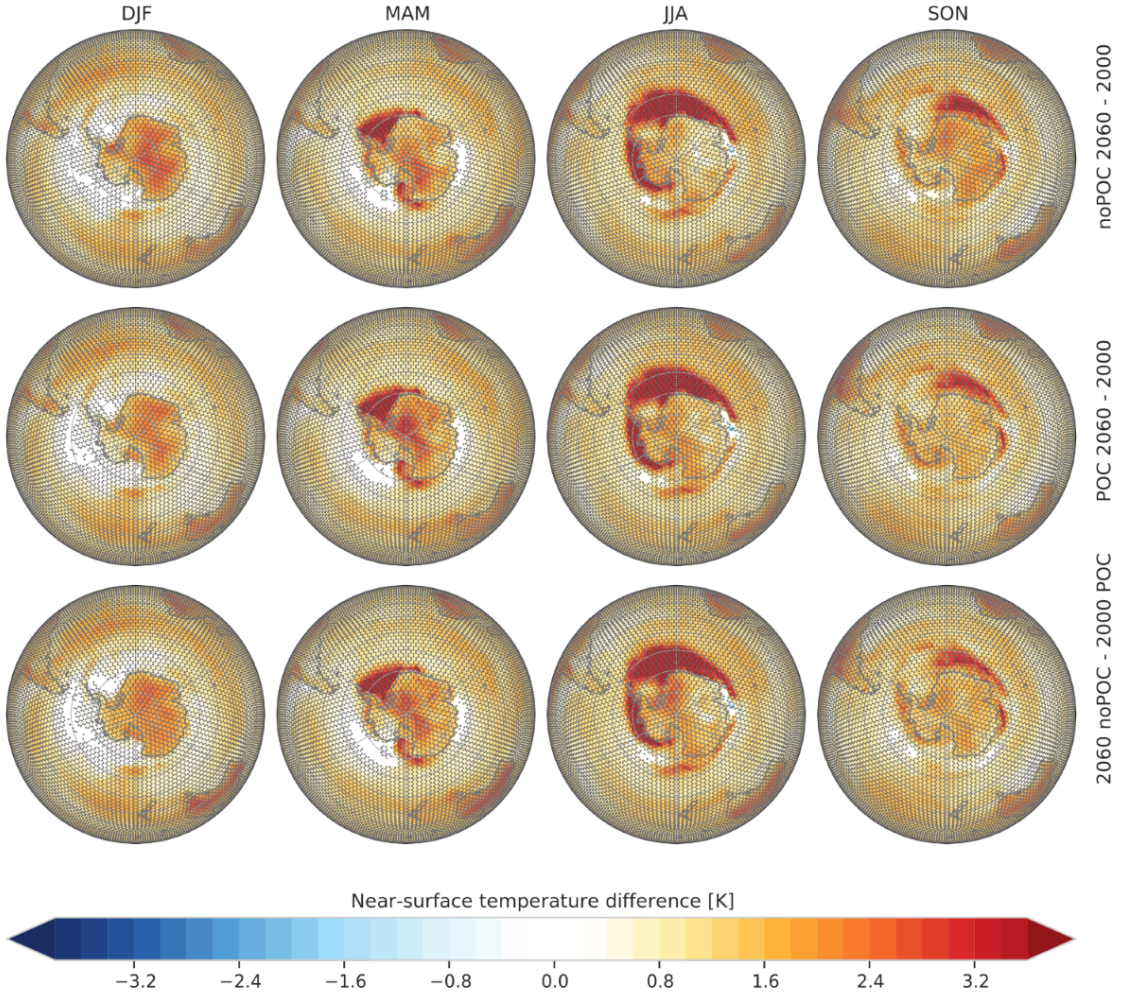

Figure 6.10: Seasonal mean near-surface temperature difference [K] between noPOC 2060 and noPOC 2000, POC 2060 and POC 2000, and noPOC 2060 and POC 2000. Dots represent significance with a false discovery rate of 0.1.

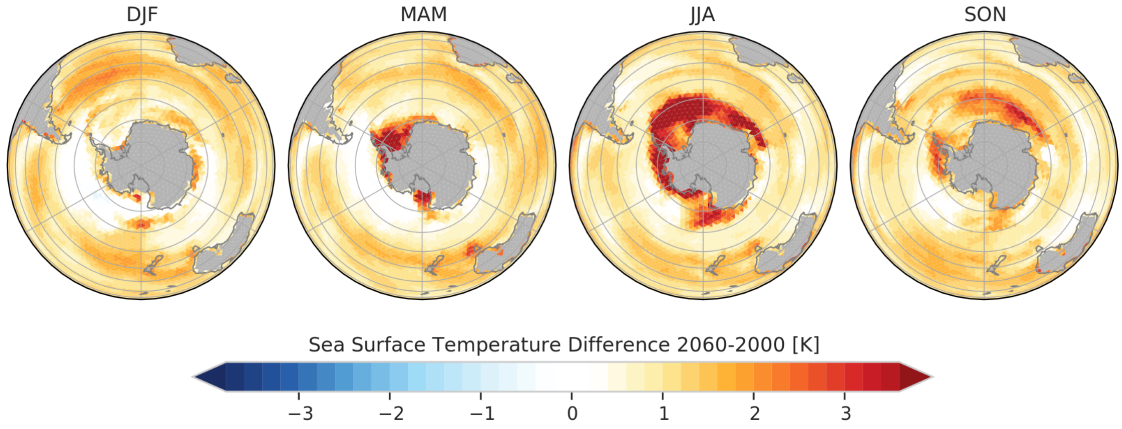

Figure 6.11: Seasonal mean prescribed sea surface temperature difference [K] between 2060 and 2000.

that the detected changes are strongly governed by changes in the prescribed boundary SSTs. However, it should be noted that the prescribed SSTs were chosen to be consistent with the prescribed GHG increases. The SST changes for large parts of the southern hemisphere are consistent with the tropospheric warming due to increased GHG detected in the previous sections. An additional seasonal warming pattern in the Southern Ocean is detected that is associated with a decreasing sea ice cover.

6.1.3 Implications for future climate

In addition to the detection of climate changes induced by polar ozone chemistry or increasing GHGs, changes associated with the climate change scenario, namely the differences between the noPOC 2060 with the POC 2000 simulation, are analyzed. The surface signals are expected to reflect changes induced by increasing greenhouse gases as well as ozone recovery. Near-surface pressure differences for this scenario (Fig. 6.8) closely resemble differences associated with increased GHG from autumn to spring. This is in line with only small pressure changes expected from ozone recovery as described in section 6.1.1. Changes in summer differ from the GHG signal with a pressure increase of up to 2 hPa south of 60°S and a pressure decrease of 1 hPa between 60 - 40°S for eastern longitudes. This pattern is in conjunction with the counteracting effect of increasing GHGs and ozone recovery. Similar behavior is visible for the near-surface differences of zonal wind (Fig. 6.9) that are closely resembling the signal detected for increased GHGs except for summer when GHG changes are counteracted by the ozone recovery signal resulting in weaker changes during that season. Near-surface temperature changes (Fig. 6.10) also closely resemble the GHG signal. The largest deviations are found over the Antarctic continent and are in agreement with the ozone recovery signal. As the signal induced by ozone recovery is significantly smaller than the GHG effect, the overall climate change signal is governed by the GHG signal.

6.1.4 Simulation of recent climate change

So far, only an intercomparison of model simulations was investigated for changes in the surface climate. The analysis of recent climate change allows for a comparison with the ERA5 reanalysis. In Figure 6.12 the summertime near-surface temperature changes between 2000 and 1980 from the ERA5 reanalysis are shown together with the detected signals between the POC 2000 and noPOC 2000 and between the POC 2000 and noPOC 1980 simulations. To account for some internal variability in the reanalysis data, mean near-surface temperatures for 1980 and 2000 were calculated for ERA5 by averaging the years 1979 - 1982 and 1998 - 2002.

The near-surface temperature change for the ERA5 data is characterized by strong warming of the Antarctic Peninsula and the Filchner-Ronne ice shelf and a strong cooling of

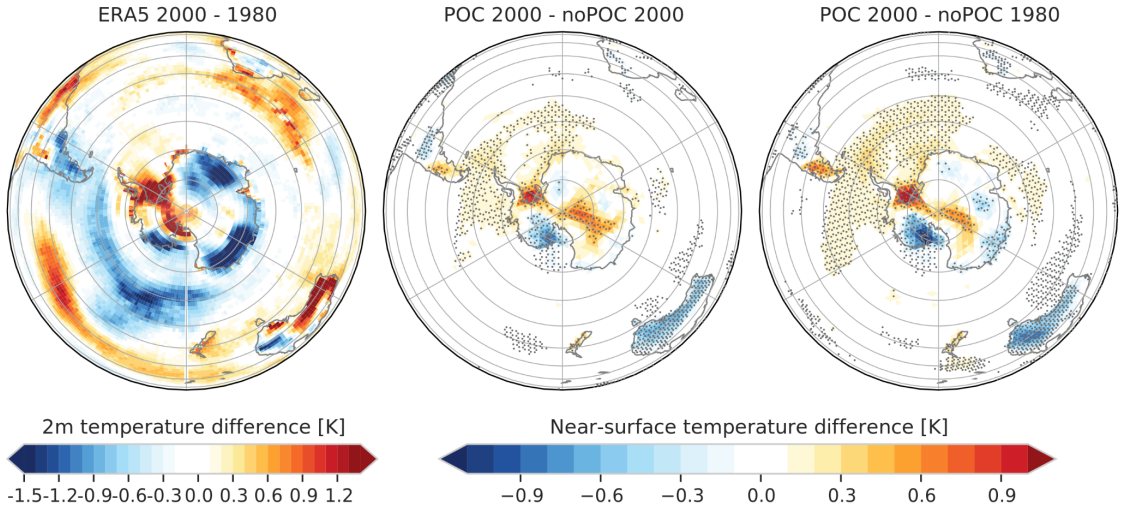

Figure 6.12: Summertime (December - February) near-surface temperature difference [K] between 2000 and 1980 for the ERA5 dataset, the POC 2000 and noPOC 2000 simulations, and the POC 2000 and noPOC 1980 simulations. For the ICON-ART simulations, dots represent significance with a false discovery rate of 0.1. Note the different colorscales, for the ERA5 and ICON-ART data.

West Antarctica and parts of East Antarctica, especially of coastal areas. Further, cooling is detected for large parts of the Southern Ocean. The temperature patterns detected in the ICON-ART simulations are similar for the differences between the POC 2000 and noPOC 2000 simulations and the POC 2000 and noPOC 1980 simulations. Both comparisons show a temperature signal that is characterized by a warming of the Filchner-Ronne ice shelf, the Antarctic Peninsula, and parts of East Antarctica and the Southern Ocean. A cooling is detected for West Antarctica and the coastal areas of East Antarctica. The temperature signal is more distinct for the differences between the POC 2000 and noPOC 1980 simulations with a larger area of the Southern Ocean warming and a stronger cooling for Antarctica. The general temperature pattern over Antarctica agrees between the ERA5 data and the ICON-ART simulations; the magnitude of the changes is more pronounced for the ERA5 reanalysis. For the remaining southern hemisphere, there are larger discrepancies between the ERA5 data and the ICON-ART simulations. These discrepancies could result from an insufficient representation of internal variability in the calculation of the ERA5 differences. As the effect of internal variability is largely covered in the ICON-ART simulations, the resulting temperature signals are comparably small. The comparison of the differences of a 4-year mean with 65 ensemble members could therefore explain the different strengths of the detected signals. Thus, considering the difficulties arising for a detailed comparison, a better agreement between the ICON-ART simulations and ERA5 than concerning the major patterns seems unlikely. Further, the ICON-ART simulations suggest that the temperature changes, including a change in

GHGs, are larger than for the effect of ozone depletion only, while the detected pattern is stable.

6.2 Model sensitivity and uncertainty estimation

6.2.1 Influence of tropospheric ozone lifetimes

Ozone concentrations in the model experiments are calculated with the Linoz scheme for altitudes higher than 10 km. Below that, a fixed tropospheric lifetime is assumed. In this section, the influence of the tropospheric ozone lifetimes on stratospheric circulation changes and the near-surface temperature and pressure signals is investigated. The lifetime of ozone in the troposphere is typically assumed to be around 20 days (Ehhalt et al., 2001; Young et al., 2013). To investigate the impact of tropospheric ozone, three sets of the POC and noPOC 2000 simulations were performed with lifetimes of 10, 20, and 30 days. Similar to the changes of zonal mean ozone concentrations and temperatures averaged over 90 - 75°S over the course of the year, as well as the changes in zonal wind averaged over 75 - 50°S displayed in Figure 6.1 for the different experiments, the changes between the POC 2000 and noPOC 2000 simulations for different tropospheric ozone lifetimes are displayed in Figure 6.13.

The changes in polar cap ozone concentrations between the POC 2000 and noPOC 2000 simulations are similar for all chosen tropospheric ozone lifetimes. The maximum ozone difference in mid-October is highest for the 30-day simulation and lowest for the 10-day simulation. The same is the case for the tropospheric changes. The polar cap temperature differences show larger deviations for the different cases. The temperature dipole pattern between October and April, which is associated with the development of the ozone hole, is comparable in all three simulations, with the largest temperature decrease for the 30-day simulation, consistent with the detected ozone changes. Temperature changes between June and October display a higher variability. The dipole pattern, with enhanced temperatures below 4 hPa and decreased temperatures above, is visible in different strengths and timing in the simulations. The pattern is particularly strong for the 10-day simulation. This corresponds with the strongest weakening of the polar vortex of all cases between June and August. The 20-day simulation shows the same temperature pattern with a decreased strength. The dipole pattern in the 30-day simulation is shifted towards later in the year and is strongest in September. Those temperature signals between June and September are only significant in the 10-day simulation. Changes in zonal wind are similar between the 10-day and 20-day simulations, showing a strong intensification signal between October and February. During polar night a small decrease in wind speeds is visible. The 30-day simulations show a stronger intensification signal between October

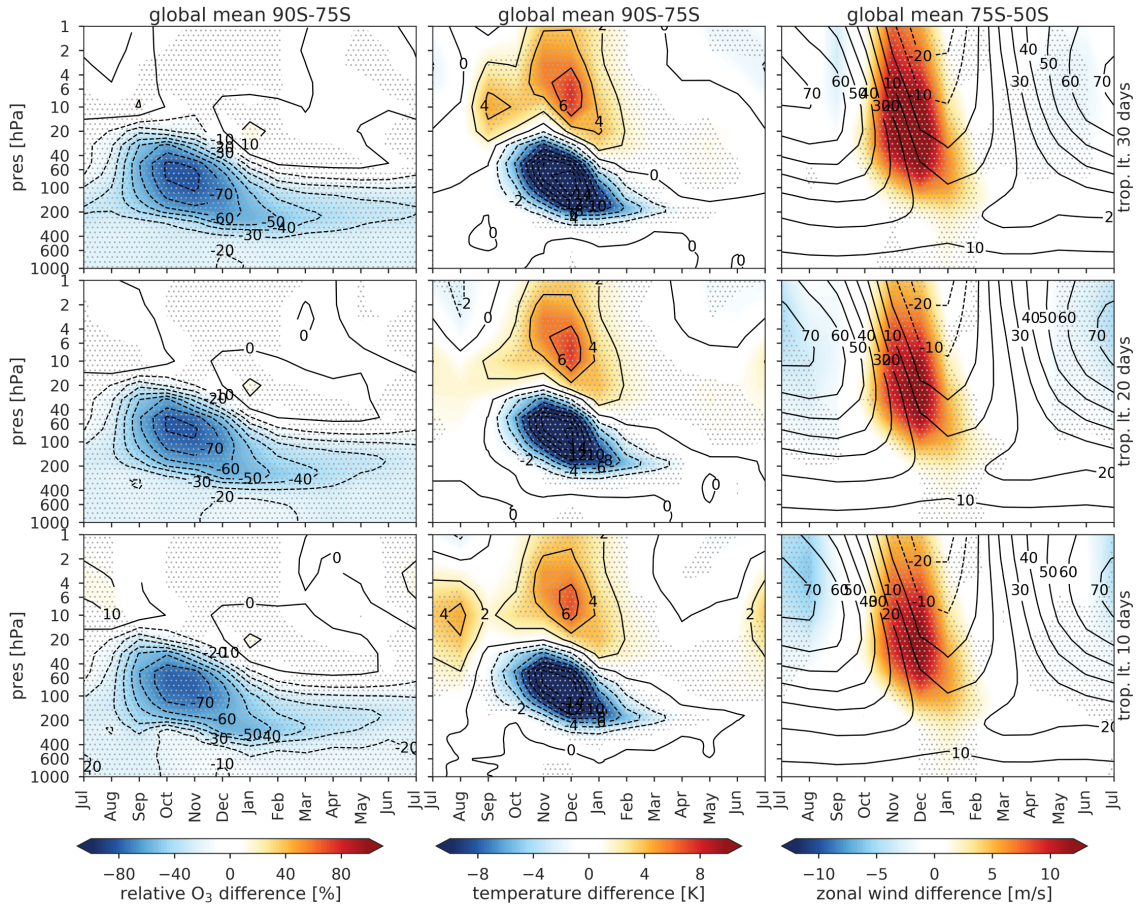

Figure 6.13: Monthly mean relative ozone difference [%] (left panels) and monthly mean temperature difference [K] (middle panels) averaged over 75°S - 90°S and monthly mean zonal wind difference [m/s] (left panels) averaged over 50°S - 75°S for the differences between the POC 2000 and noPOC 2000 experiment with tropospheric lifetimes of 30, 20 or 10 days. The percentage of ozone difference is based on the ozone concentration of the POC 2000 experiment. Contour lines depicted for the zonal wind differences show the zonal wind climatology of the POC 2000 experiment. Dots represent significance with a false discovery rate of 0.1.

and February, matching the stronger ozone signal. Between June and October, changes are not significant in this set of simulations.

Overall, the detected ozone changes are only slightly modulated by different tropospheric ozone lifetimes. The same is the case for the induced radiative and dynamical feedbacks that lead to the dipole temperature structure and result from the changes in ozone between October and February. This is also manifested by the increase of wind speeds leading to a prolonged persistence of the vortex. While the spring and summertime signal is very robust, the effect of polar ozone depletion on the wintertime circulation and climate differs for the chosen tropospheric ozone lifetimes. The different manifestations of wintertime circulation changes coincide with the season of highest variability of the polar vortex and could therefore be the result of internal variability. Thus, for the investigation of

wintertime changes, a higher sample size would be desirable to predict climate change signals confidentially.

The analysis of the ozone hole induced near-surface signals showed the highest number of significant grid points and similar patterns in summer for the years 2000 and 2060. All other seasons showed a smaller number of significant grid points and larger deviations in the detected patterns. This indicates that near-surface changes in all other seasons are more variable and might be caused by a larger internal variability. To further investigate this assumption, the effect of choosing different tropospheric ozone lifetimes on the surface signal is analyzed. This analysis focuses only on changes in pressure and temperature, as changes in zonal wind are closely related to changes in pressure.

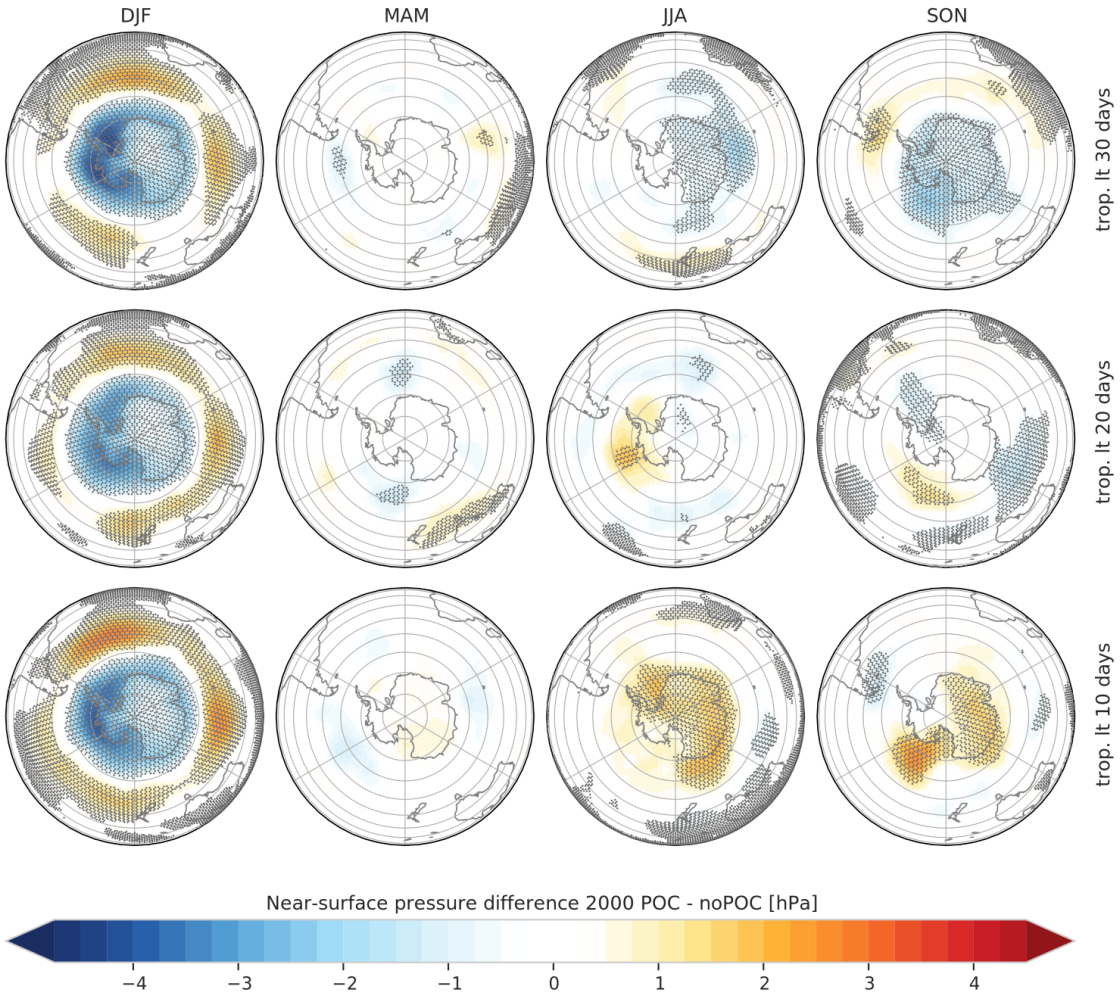

Figure 6.14: Seasonal mean near-surface pressure difference [hPa] between POC 2000 and noPOC 2000 with tropospheric lifetimes of 30, 20 or 10 days. Dots represent significance with a false discovery rate of 0.1.

The near-surface pressure changes identified for the different tropospheric ozone lifetimes (Fig. 6.14) strongly resemble each other during summer and are characterized by the significant pressure decrease south of 60°S and a significant pressure increase from

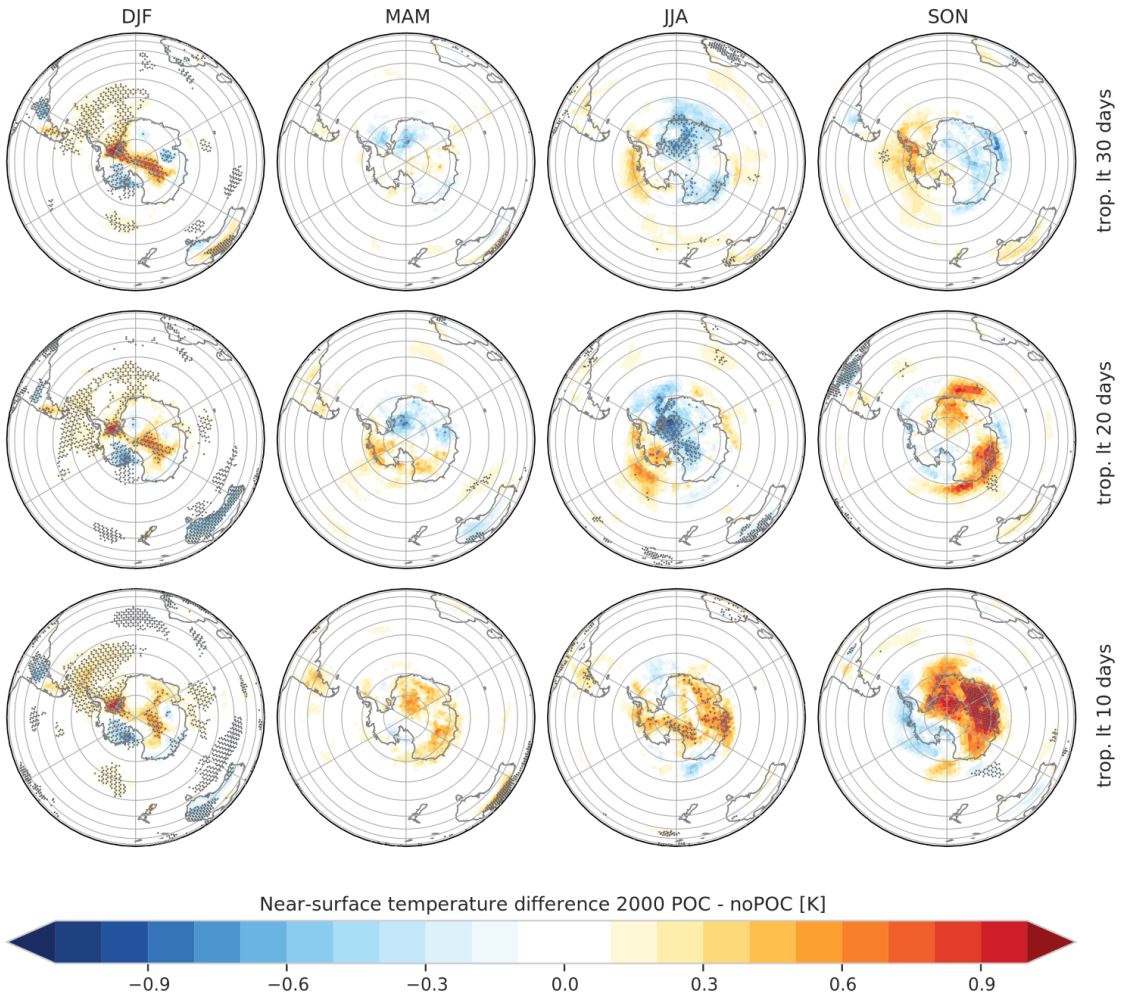

Figure 6.15: Seasonal mean near-surface temperature difference [K] between POC 2000 and noPOC 2000 with tropospheric lifetimes of 30, 20 or 10 days. Dots represent significance with a false discovery rate of 0.1.

60 to 30°S. The main differences are visible in the location of the maxima and minima occurring in the regions of increased pressure. As already noticed for the impacts of polar ozone depletion for the 2000 and 2060 simulations analyzed before, all other seasons show a smaller number of significant grid points and typically a weaker signal for all chosen lifetimes. Nevertheless, regional patches of significant grid points are found for most of the remaining seasons and chosen tropospheric ozone lifetimes. However, the regional patterns visible for a particular season do not resemble each other, neither in location nor sign in contrast to the summertime differences.

The detected near-surface temperature changes (Fig. 6.15) show a similar response to different tropospheric ozone lifetimes as the pressure signals. The patterns of temperature changes for summer are similar for the chosen tropospheric lifetimes with significant warming around the Antarctic Peninsula, a significant warming pattern in East Antarctica around 120°E, and the significant cooling of West Antarctica. All other seasons show a

smaller number of significant grid points. While temperature changes in autumn show barely any significance, changes in winter and spring show significant areas over Antarctica. However, the identified changes in those seasons vary strongly in location and sign for different tropospheric ozone lifetimes. This could either indicate the importance of a correct representation of tropospheric ozone lifetimes during those seasons or hint at a large internal variability that is not sufficiently represented by the number of ensemble members. In conjunction with the results of the differences in zonal mean circulation, showing large differences in the stratospheric temperature and zonal wind response between June and October, the latter is the more likely case. In conclusion, analyzing the ozone hole induced near-surface climate changes should be limited to the summer season, as a robust response to stratospheric changes is visible, while the remaining seasons show distinct differences and need further sensitivity studies analyzing the influence of tropospheric ozone lifetimes as well as larger ensemble sizes to exclude a large influence of internal variability.

6.2.2 Uncertainty of near-surface temperature signals

Besides the identification of significant grid points, it is desirable to obtain an uncertainty estimate for the detected near-surface temperature changes. The timeslice approach used in this study offers the possibility to calculate an ensemble-based uncertainty estimate. The uncertainty estimate used here quantifies the influence of individual realizations on the detected signals. A detailed description of the uncertainty estimate calculation is given in section 4.2. The resulting uncertainties for seasonal near-surface temperature differences between the POC 2000 and noPOC 2000, as well as the POC 2060 and POC 2000 simulations, are shown in Figure 6.16.

Both differences show similar uncertainty characteristics, with the weakest uncertainties in summer and highest uncertainties in winter. The largest uncertainties for each individual season are associated with land grid points or high southern latitudes. Uncertainties for latitudes below 50°S are typically smaller and do not exhibit a considerable annual cycle. The annual cycle detected for polar latitudes is characterized by an extent of enhanced uncertainty values that closely resembles the extent of sea ice coverage (see Figure 6.17). The strength and extent of uncertainties are hardly affected by the chosen comparison or the strength of the detected surface temperature difference for the chosen experiments. The small uncertainties for ocean grid points indicate a strong influence of the prescribed sea surface temperatures damping the surface temperature signal and, therefore, its variability. In contrast, grid points associated with land or sea ice display higher uncertainties and are therefore associated with a higher variability that is not significantly influenced by the choice of model experiments.

In summer, uncertainties over land reach maximum values of 0.15 K, ocean grid points show an uncertainty estimate below 0.05 K. For the other seasons, the regions of enhanced uncertainty are extended to the Southern Ocean with a maximum extend during winter and spring and maximum values up to 0.25 K uncertainty during winter. The enhanced uncertainties in winter are consistent with the assumption of higher internal variability during that time of year.

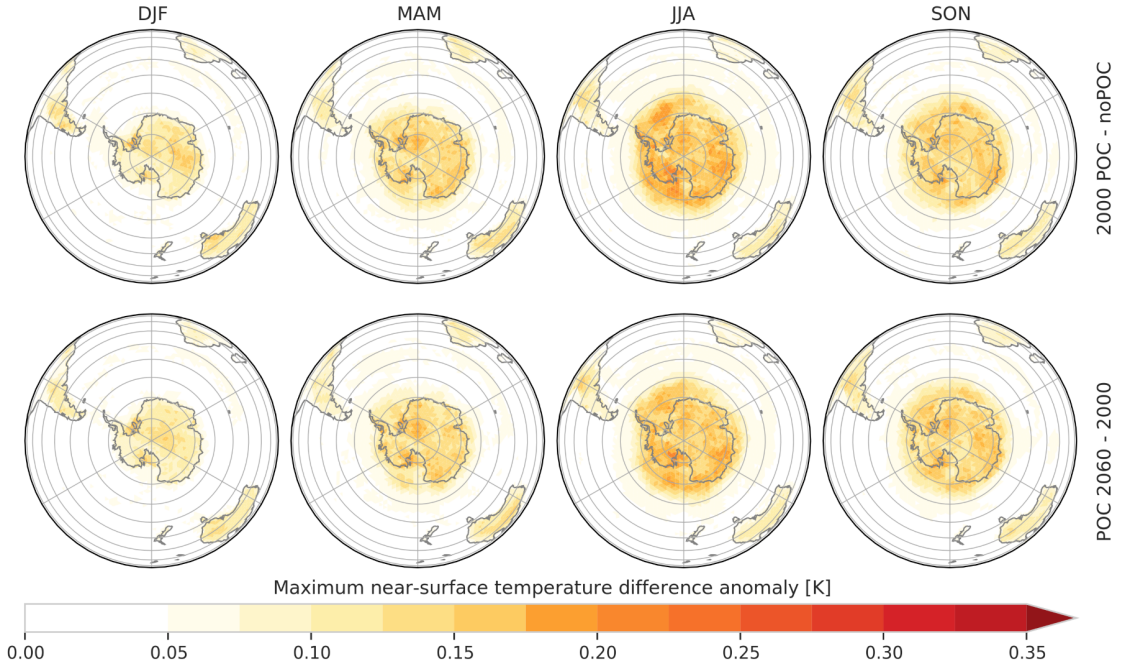

Figure 6.16: Seasonal uncertainty estimate [K] for the near-surface temperature difference between POC 2000 and noPOC 2000.

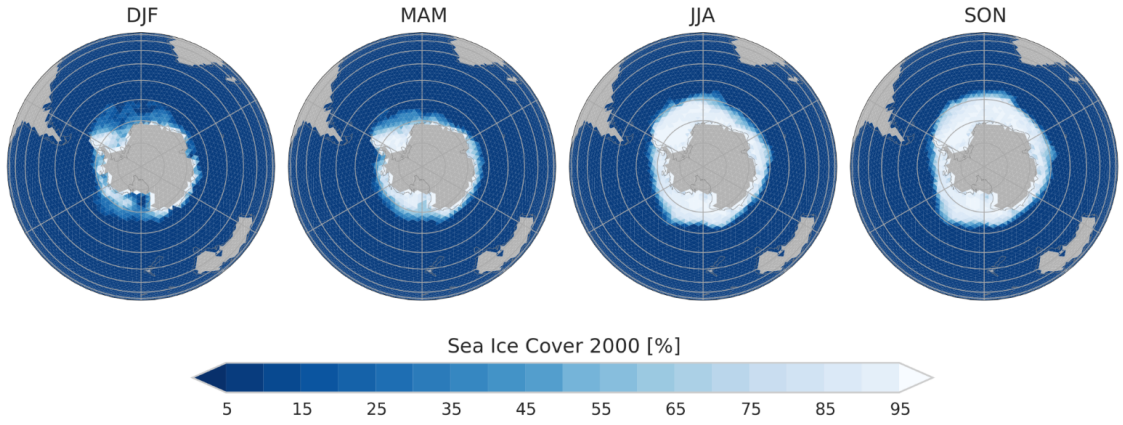

Figure 6.17: Seasonal mean prescribed sea ice cover [%] for 2000.

The uncertainties of the near-surface temperature signal are expected to decrease with increasing ensemble members. Therefore, the influence of the chosen ensemble size on the detected uncertainties is quantified for the ICON-ART simulations. Based on the find-

ing that the choice of model experiments is not crucial for the uncertainty estimation of a season, the analysis is performed for the near-surface temperature difference between the POC and noPOC 2000 simulations for summer. The ensemble-based uncertainty estimate was applied for four different ensemble sizes of 20, 35, 50, and 65 realizations. The results are depicted in Figure 6.18.

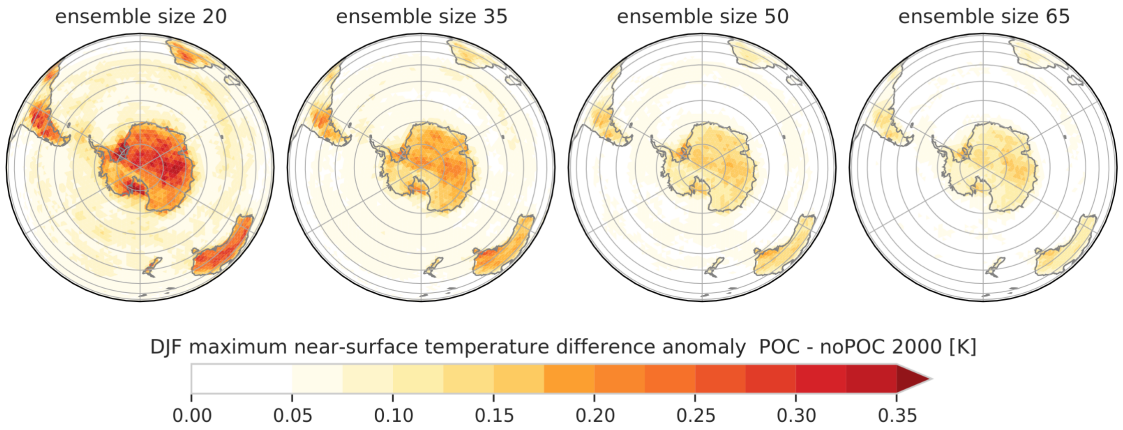

Figure 6.18: Summertime uncertainty estimate [K] for the near-surface temperature difference between POC 2000 and noPOC 2000 for ensemble sizes of 20, 35, 50 and 65.

Comparable to the previous findings from the analysis of seasonal uncertainties, land grid points show a larger uncertainty than ocean grid points for all chosen realization sizes. Further, the regions of highest uncertainty are similar for different realization sizes. As expected, uncertainty decreases with an increase in ensemble size. While the uncertainty of the Antarctic temperature difference is typically around 0.3 K for 20 realizations, it is only around 0.1 K for 65 ensemble members. Further, the uncertainty for ocean grid points drops from values up to 0.1 K to values below 0.05 K.
Considering the magnitude of the near-surface temperature difference detected (around 0.15 K for ocean grid points and up to 0.7 K for land grid points), a sample size of 20 would typically result in uncertainties around 50 % with some grid points showing an uncertainty estimate with a similar magnitude as the actually detected signal. A realization size of 65, as used in this study, shows decreased uncertainties of around 20 %. Thus, our analysis underlines the importance of long timeslice integrations for a detailed characterization of ozone hole induced surface climate signals.

6.3 Conclusions

The climate change signals induced by changes in polar ozone chemistry and increasing GHGs simulated with ICON-ART timeslice experiments were analyzed in this chapter with a focus on the southern hemisphere. The occurrence of the Antarctic ozone hole results in a stratospheric cooling in the altitude range of ozone depletion. This cooling

is detected from October to January for levels between 300 and 20 hPa with a maximum temperature decrease of up to 16 K in December. A weaker cooling persists in the lower stratosphere until March. At higher altitudes, warming of up to 6 K is detected between October and January. The results are comparable for the years 2000 and 2060, with stronger stratospheric signals of around 2 K for 2060, likely resulting from the increased ozone depletion modeled for the year 2060 due to colder stratospheric temperatures. The robustness of the ozone hole induced temperature and circulation changes was analyzed based on a sensitivity study investigating the impact of changes in tropospheric ozone lifetimes. The results suggest a very robust signal between October and March, while estimates for winter show some uncertainties.

The temporal evolution and altitude structure of the stratospheric temperature decrease is similar to the observational studies by Randel and Wu (1999) and Thompson and Solomon (2002), as well as multiple modeling studies (e.g. Gillett and Thompson, 2003; Karpechko et al., 2008; McLandress et al., 2011). The maximum stratospheric temperature decrease is slightly delayed compared to these studies, which is likely connected with the delayed vortex breakup in the ICON-ART simulations. While most previous studies focused only on stratospheric levels up to 10 hPa, the occurrence of the temperature increase at higher stratospheric levels detected in the ICON-ART simulations is also reported by Keeble et al. (2014), Perlwitz et al. (2008), and Maycock et al. (2018).

Consistent with the temperature changes, a strengthening of the polar vortex by up to 12 m/s was detected throughout the stratosphere between October and January. Changes in zonal wind penetrate down to the troposphere, where a slight intensification of the zonal wind is observed between December and February. This response of the zonal wind to the induced stratospheric temperature changes was also detected by various modeling studies. However, the strength of the ozone hole induced stratospheric temperature changes differs between individual studies. Consequently, the changes in the zonal wind are varying accordingly.

The observational studies by Randel and Wu (1999) and Thompson and Solomon (2002) estimated a stratospheric cooling trend of 6 K and 7 K between 1970 and 2000. The cooling trends estimated in transient modeling studies vary between 6 - 7 K/30 years (Karpechko et al., 2008, 2010), 3 K/decade (Maycock et al., 2018; Son et al., 2010), and 5.5 K/decade (McLandress et al., 2011) as well as a 15 K temperature difference between 1969 and 1999 (Perlwitz et al., 2008). Idealized timeslice simulations estimated the ozone hole induced stratospheric cooling to be even higher between 9 K (Gillett and Thompson, 2003) and 12 K (Keeble et al., 2014). The stratospheric warming above is estimated to range between 0.8 K/decade (Maycock et al., 2018) and 6 K (Keeble et al., 2014). Changes in stratospheric zonal wind vary accordingly, ranging from 3 m/s decade (Son et al., 2010) to 12 m/s difference between simulations with and without ozone chem-

istry (Keeble et al., 2014). The detected tropospheric wind signal lies typically between 0.5 - 1 m/s.

Compared to those previous studies, the ozone hole induced stratospheric climate change signals visible in the ICON-ART simulations are stronger than typically detected. However, it should be noted that observational studies are typically based on few radiosonde observations, with the majority of locations north of 70°S. Ozone hole induced signals are likely larger in the center of the Antarctic ozone hole and are thus not fully represented by the sparse amount of observational data. Therefore an underestimation of the signal by observational studies cannot be excluded. Further, modeling studies performing transient simulations calculate a linear trend in stratospheric temperatures that is smaller than the differences calculated between idealized timeslice simulations. This could indicate a non-linear relationship between polar ozone depletion and the detected stratospheric response that cannot be fully represented by the linear trend calculation. Further, those studies do not account for internal variability. The results obtained from the ICON-ART simulations in this study show similar results as the study by Keeble et al. (2014), who performed a modeling study with a comprehensive and interactive ozone calculation and a timeslice setup. Similarities in the strength of the detected signals could therefore indicate an increased ozone hole induced signal if an interactive calculation of ozone is implemented in the models.

Increasing GHGs between 2000 and 2060 result in tropospheric warming of around 1 K and stratospheric cooling of about 4 K in the Antarctic polar region in the ICON-ART simulations. Further, a strengthening of the polar night jet at altitudes above 20 hPa is detected. Comparing the noPOC 2060 simulation with the POC 2000 simulation, a composed signal of increased GHGs and ozone recovery changes is visible. A tropospheric warming and stratospheric cooling is detected, as well as a temperature increase in the lower stratosphere of more than 14 K due to the recovery of the ozone hole and an additional stratospheric cooling above. Temperature changes are represented by changes in zonal wind and show a stronger but less persistent polar vortex with enhanced wind speeds between April and October and decreased wind speeds between October and December. The structure and magnitude of the calculated changes are consistent with the modeling studies by Perlwitz et al. (2008), Karpechko et al. (2010), and McLandress et al. (2011).

Ozone hole induced surface climate signals are robust in the ICON-ART simulations in summer. All other seasons show weaker and more variable signals and are thus not considered reliable. Summertime differences in near-surface pressure are characterized by a pressure decrease of 1 - 4 hPa south of 60°S and a pressure increase of up to 3 hPa between 60 and 30°S. These changes are represented by an increase of zonal winds up to 1.5 m/s between 70 and 50°S and a significant decrease in wind speeds of about 1 m/s between 50 and 30°S, indicating a shift of the jet towards higher latitudes. The changes in near-surface pressure are consistent with the December-May trend in 500 hPa geopoten-

tial height observed by Thompson and Solomon (2002) and the corresponding modeling study by Gillett and Thompson (2003). The magnitude of the detected pressure changes is comparable with the December-May sea level pressure trend modeled by Arblaster and Meehl (2006) as well as the station data presented by Turner et al. (2005). Magnitude and pattern also closely resemble the results of the idealized timeslice experiments by Keeble et al. (2014) and Polvani et al. (2011b) but show a smaller pressure decrease over East Antarctica and a different position of maxima for the regions of increased pressure.
The near-surface pressure signal due to increased GHGs is characterized by lower pressure of 1 - 3 hPa south of 50 to 60°S and increased pressure of 1.5 - 3 hPa at lower latitudes. Pressure changes associated with climate change are very similar to the GHG scenario for all seasons but summer. Here, the GHG signal is counteracted by ozone recovery, resulting in increased near-surface pressure of about 2 hPa in Antarctica. These results agree well with Polvani et al. (2011a). Further, Son et al. (2009) detected the counteracting effects of GHGs and ozone recovery in summer in idealized model simulations. However, the magnitude of the pressure changes differs from the ICON-ART results.
While the near-surface pressure changes of the ICON-ART simulations are consistent with and throughout other studies, the picture becomes less clear when investigating the changes in near-surface temperature. The sonde observations presented in Thompson and Solomon (2002) detect a December-May linear temperature trend of 0.5 - 1.5 K/30 years for the Antarctic Peninsula and Patagonia and a 0.5 - 2 K/30 years temperature decrease for the rest of Antarctica. The station data presented in Turner et al. (2005) show a similar tendency for Antarctic stations during summer. However, the cooling observed here is less pronounced. Chapman and Walsh (2007) attempted a comprehensive estimate of Antarctic temperature based on station data based on correlation length scales. The result suggests complex warming and cooling patterns in summer that are, however, not significant. Gillett and Thompson (2003) could model similar temperature trends as those obtained from sonde observations. However, the results are less pronounced than those presented in Thompson and Solomon (2002). Further, Gillett and Thompson (2003) detect warming for some parts of East Antarctica, as well as for the Filchner-Ronne ice shelf. This warming of the Filchner-Ronne ice shelf is also visible in ERA-40 as well as modeling data as analyzed by Arblaster and Meehl (2006). For ERA-40, additional warming at some parts of East Antarctica is detected. In contrast, Keeble et al. (2014) detect warming of the Antarctic Peninsula and Patagonia and cooling for the rest of Antarctica as a result of the idealized timeslice experiments. However, this result focuses on December only, while the other studies analyzed data from December to May.
A warming of the Antarctic Peninsula, Patagonia, and the Filchner-Ronne ice shelf is also detected in the ICON-ART simulations for summer. Further, a warming pattern in East Antarctica is pronounced in the model simulations, while West Antarctica and the coastal areas are experiencing a cooling. Overall, our model results show an agreement

with previous modeling studies. However, the cooling of large parts of Antarctica is less pronounced in our simulations. The exact warming and cooling patterns differ in previous modeling studies and are likely influenced by the experimental design and the chosen averaging intervals for the calculation of differences and trends. Further, observational data is sparse and mostly limited to coastal areas. Thus, a meaningful interpretation of the temperature evolution of the whole Antarctic continent is difficult.

The signals detected due to increased GHG are seasonally more uniform and show significant changes throughout the year. Changes in near-surface pressure are characterized by a pressure decrease south of 50 to 60°S, and a pressure increase at lower latitudes. The changes in wind correspond to the pressure changes. The near-surface temperature signals show an overall southern hemispheric warming and a seasonal cycle that is influenced by the prescribed SSTs. The analysis of the combined influence of increased GHGs and ozone recovery closely resembles the effects of increased GHGs for all seasons but summer. Then, changes in near-surface pressure and zonal wind are influenced by the counteracting effects of increased GHGs and ozone recovery. The temperature signal, however, closely resembles the GHG signal due to the comparably smaller magnitude of the ozone recovery effect.

Overall the observed stratospheric and tropospheric climate change signals detected in the ICON-ART simulations are consistent with previous studies. However, the near-surface temperature signal shows some discrepancies compared to previous model results. Therefore a closer investigation of the origin of those near-surface temperature changes is desirable. Changes in near-surface temperatures are often associated with climatological changes of the tropospheric Southern Annular Modes. Thus, to further investigate the origin of near-surface temperature signals in this study, we analyze the model's representation and climatological changes of the Southern Annular Mode in detail in the following chapter.

7 Simulated patterns of variability: The Southern Annular Mode

A large fraction of southern hemispheric near-surface circulation changes due to polar ozone depletion and increasing GHGs is associated with changes of the near-surface SAM that are characterized by a latitudinal shift of the midlatitude jet (e.g. Thompson and Solomon, 2002). While the SAM accounts for large parts of the simulated climate change, the magnitude of trends, and thus the shift in the southern hemispheric westerlies, calculated from different models for a similar external forcing differs (e.g. Yin, 2005). Those differences in the SAM's response to external forcing could be dependent on the models' representation of the internal variability of the SAM itself (e.g. Gerber et al., 2008b). Models with a high persistence of SAM anomalies are found to develop larger trends than models with a shorter persistence of SAM anomalies for similar climate forcings (Gerber et al., 2008a). This is consistent with fluctuation-dissipation theory (e.g. Leith, 1975; Ring and Plumb, 2008) that links the strength of the SAMs response to external forcing to its e-folding timescale, a measure that is commonly used to analyze the persistence of SAM anomalies. More persistent e-folding timescales go along with a stronger sensitivity to external forcing, while shorter e-folding timescales are associated with a weaker climate response to external forcing. Consequently, a correct representation of the internal variability of the SAM is crucial to model recent and future climate change accurately.

Therefore, the e-folding timescale is used as a benchmark for climate models, with a realistic representation of e-folding timescales indicating a realistic model response to external forcing. However, tropospheric e-folding timescales are commonly overestimated in GCMs, which might imply that those models are overly sensitive to external forcing (e.g. Kim and Reichler, 2016).

The stratosphere and troposphere are dynamically coupled, and thus the stratospheric SAM can influence the tropospheric SAM. Large and persistent stratospheric SAM anomalies can induce persistent tropospheric SAM anomalies of the same sign (Thompson et al., 2005). Consequently, large and persistent stratospheric SAM anomalies can result in increased tropospheric SAM e-folding timescales (Baldwin et al., 2003). Thus, an incorrect representation of the stratospheric variability can lead to biases in the troposphere. Due to the coupling of the stratosphere and the troposphere, the stratospheric SAM can be used to predict the surface SAM one month in advance. As surface SAM anomalies are associ-

ated with characteristic temperature and precipitation anomalies (e.g. Gillett et al., 2006), the extended-range weather forecast can be affected by changes in the predictability of the surface SAM due to stratospheric changes.
In the following section, the representation of internal variability of the SAM in the ICON-ART simulations is analyzed as well as the coupling between the stratosphere and the troposphere. The results are compared with the ERA5 reanalysis to investigate if the model shows realistic results for the 2000 simulations. Further, the changes between the different model simulations are analyzed. The analysis of the SAM's internal variability and the stratosphere-troposphere coupling is performed based on the variability and persistence of the SAM as well as a prediction value that indicates how strongly the SAM at different levels influences the near-surface SAM one month in advance. In the subsequent section, changes in near-surface temperature associated with changes in the near-surface SAM are investigated.

7.1 Temporal structure of the Southern Annular Mode

The Southern Annular Mode can be defined at each pressure level, resulting in a characteristic SAM pattern and a corresponding index time series at every level. Consequently, the temporal structure of the SAM can be analyzed across different levels. However, the percentage of the variance explained by the SAM differs for different altitudes.

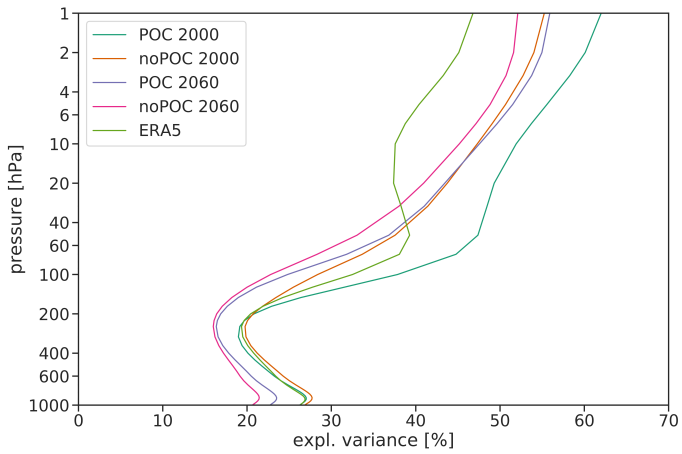

Figure 7.1: Explained variance of the Southern Annular Mode as a function of pressure for the ICON-ART simulations and the ERA5 dataset.

The explained variance for different levels is depicted in Fig. 7.1 for the POC and noPOC, 2000 and 2060 simulations, as well as for detrended ERA5 data from 1986 to 2014. The general structure is similar for all datasets. Lowest explained variances of about 20 % are visible around 200 hPa in the tropopause region. Below 200 hPa, in the troposphere, explained variances decrease with altitude. Above 200 hPa, in the stratosphere, the explained variances are increasing with altitude.

Comparing the different ICON-ART simulations, the 2060 simulations show smaller explained variances than the 2000 simulations. This indicates that the SAM shows decreased internal variability in the future, and thus other modes of variability gain more importance. Further, the noPOC simulations exhibit smaller explained variances in the stratosphere than the corresponding POC simulations. The explained variances obtained from the ERA5 dataset are in agreement with the 2000 simulations in the troposphere and the lowermost stratosphere. At levels above 50 hPa, the ICON-ART simulations show significantly higher explained variances.
Corresponding with the explained variance is the climatological distribution of SAM indices at a given level, with a larger spread for high explained variances and a smaller spread for low explained variances. Therefore, a normalization of the SAM time series at every level is advantageous for analyzing the temporal structure of the SAM across different altitudes.

7.1.1 Standard deviation

The SAM's variability at different altitudes is analyzed based on the standard deviation as a function of month and altitude. The results for the ERA5 dataset are depicted in Figure 7.2. The results for the ICON-ART experiments are shown in Figure 7.3.

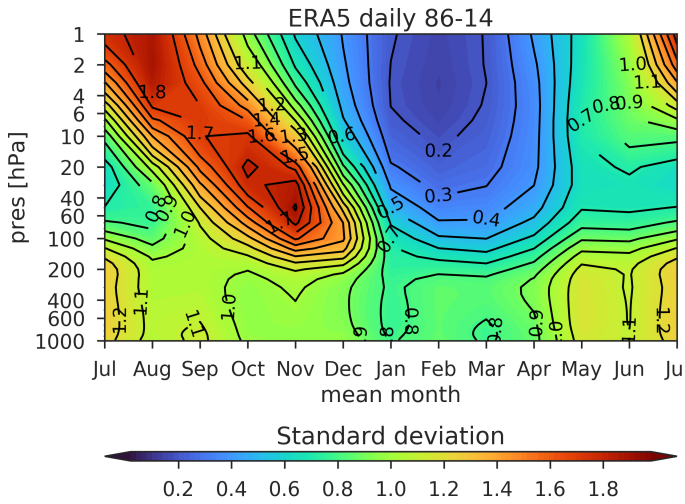

Figure 7.2: Standard deviation of the SAM index as a function of month and pressure for detrended daily ERA5 data for the period 1986 - 2014.

The standard deviation for the ERA5 dataset shows a strong seasonal cycle with the highest variability in the upper stratosphere during winter and a weak variability in summer with a minimum in February. While the minimum appears in February throughout the stratosphere, the stratospheric maximum is shifted towards later dates with decreasing altitude. The maximum is detected in August at 1 hPa and in November at 100 hPa, about three months delayed to the upper stratospheric signal. In the troposphere, the annual

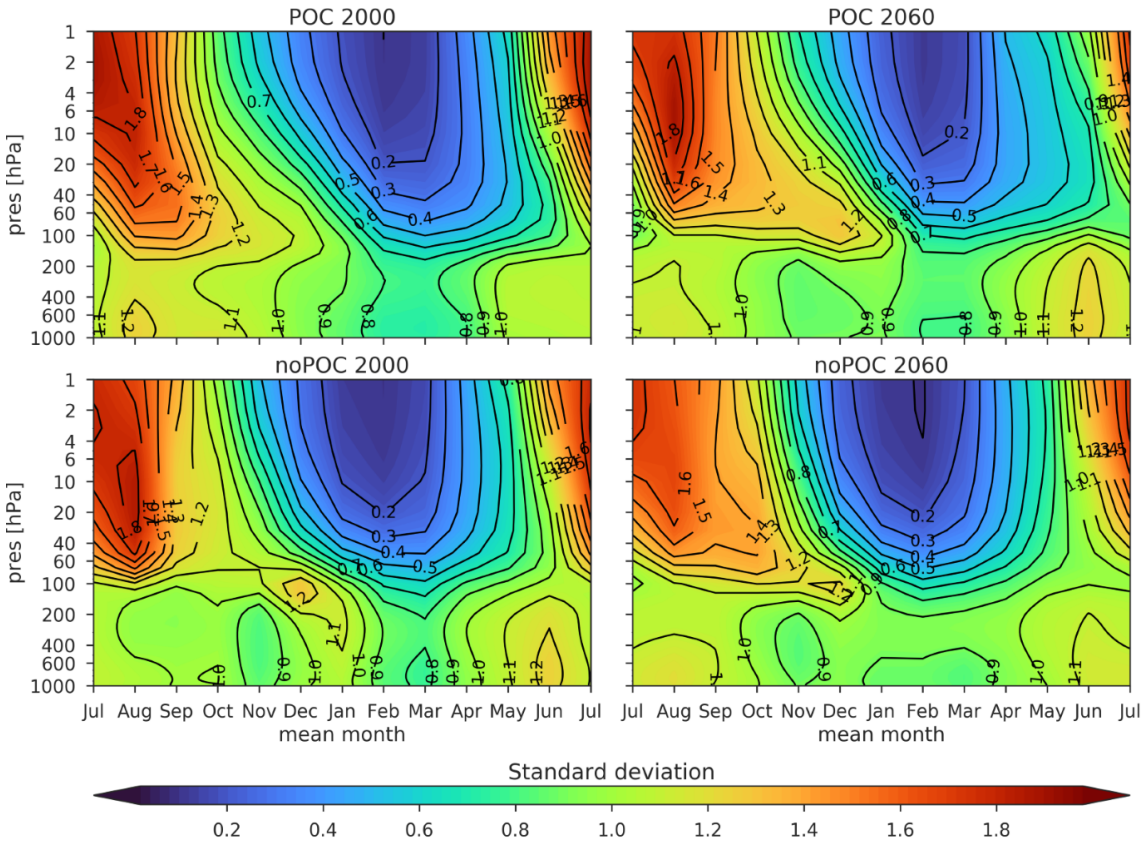

Figure 7.3: Standard deviation of the SAM index as a function of month and pressure for the POC 2000, noPOC 2000, POC 2060, and noPOC 2000 simulations.

cycle is less pronounced than in the stratosphere. Tropospheric variability is highest in the winter and lowest during late summer and early autumn.

The variability of the SAM can be regarded as a proxy for the variability of vortex strength in the stratosphere. As the polar vortex is climatologically strong in winter, the variability in this season is comparably small (Baldwin et al., 2003) as detected for levels between 10 and 100 hPa between June and August in the ERA5 dataset. The highest variability is associated with the breakdown of the polar vortex that begins in the upper stratosphere and evolves downward with time. Variability is small during summer due to the occurrence of stratospheric easterlies that prohibit the vertical propagation of waves and thus limit the wave-induced variability (Gerber et al., 2010).

The ICON-ART experiments show a similar variability structure of the SAM as the ERA5 dataset. The annual cycle is more pronounced in the stratosphere than in the troposphere, with the largest stratospheric variability values in winter and the lowest variability in summer. Tropospheric variability is highest in winter and lowest in summer and autumn. The lowest stratospheric variability in the model is detected during the occurrence of easterly or weak westerly winds. Even though the overall temporal variability structure is similar for the ICON-ART simulations and ERA5, some distinct differences appear. While the highest variability in the ERA5 dataset is associated with the breakup of the

polar vortex, the ICON-ART simulations show the highest stratospheric variability during mid-winter. A high variability during that time of year indicates a large variability of the strength of the polar vortex. Due to the higher variability of the mid-winter SAM, the pronounced descent of maximum variability with time, as detected for the ERA5 dataset, cannot be identified in the model simulations. However, a slight descent of enhanced values associated with the breakup of the polar vortex is recognizable between 10 and 100 hPa in spring and early summer in the ICON-ART simulations.

For all model experiments, the detected temporal structure of variability is highly dependent on the predominantly apparent wind speeds, i.e., the lowest internal variability in the stratosphere occurs during the existence of easterly or weak westerly winds. In contrast, higher variability is associated with predominantly westerly flows.

Consequently, the POC simulations exhibit a delayed transition to low stratospheric variabilities in autumn. This is consistent with a delayed transition to easterlies and prolonged persistence of the polar vortex as detected in the previous chapter.

7.1.2 E-folding timescale

The e-folding timescale of SAM anomalies is defined as the time where the autocorrelation function of the SAM decreases to 1/e. A detailed description of its calculation workflow is given in section 4.4.1. The e-folding timescale can be interpreted as a rough estimate of the persistence of SAM anomalies. Long e-folding timescales indicate a slow decay of anomalies, whereas short e-folding timescales correspond to a fast decay of anomalies. The e-folding timescales should be analyzed with respect to the SAM's variability, i.e., long e-folding timescales are more meaningful when the corresponding variability is large (Gerber et al., 2010). The e-folding timescales calculated from the ERA5 dataset are depicted in Figure 7.4 together with the detected variability represented by contour lines. The results for the ICON-ART experiments are shown in Figure 7.5.

For the ERA5 dataset, the largest e-folding timescales are detected between August and December in the stratosphere. The annual cycle is most pronounced between 150 and 10 hPa, where a maximum of around 70 days is visible between August and November. In the upper stratosphere above 10 hPa, the maximum occurs in November and December. The shortest stratospheric e-folding timescales of around 20 days are visible from January to May for all stratospheric levels.

The high stratospheric values are associated with the persistence of the polar vortex. The maximum between August and November occurs during a period of high variability that is associated with the strength of the polar vortex and its breakup date. High e-folding timescales in this period indicate that anomalies decay slowly, i.e., a strong vortex will likely remain strong, while a weak vortex will likely stay weak. Therefore high e-folding timescales during periods of high variability suggest a high interannual variability with

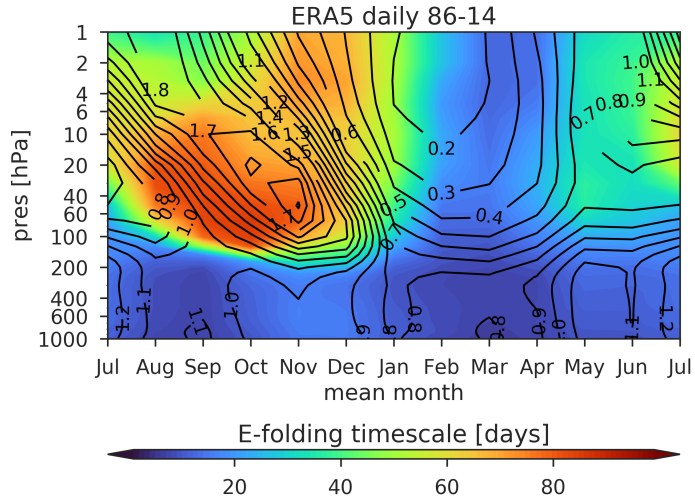

Figure 7.4: E-folding timescale of the SAM index [days] as a function of month and pressure for detrended daily ERA5 data for the period 1986 - 2014. Contour lines represent the standard deviation of the SAM index.

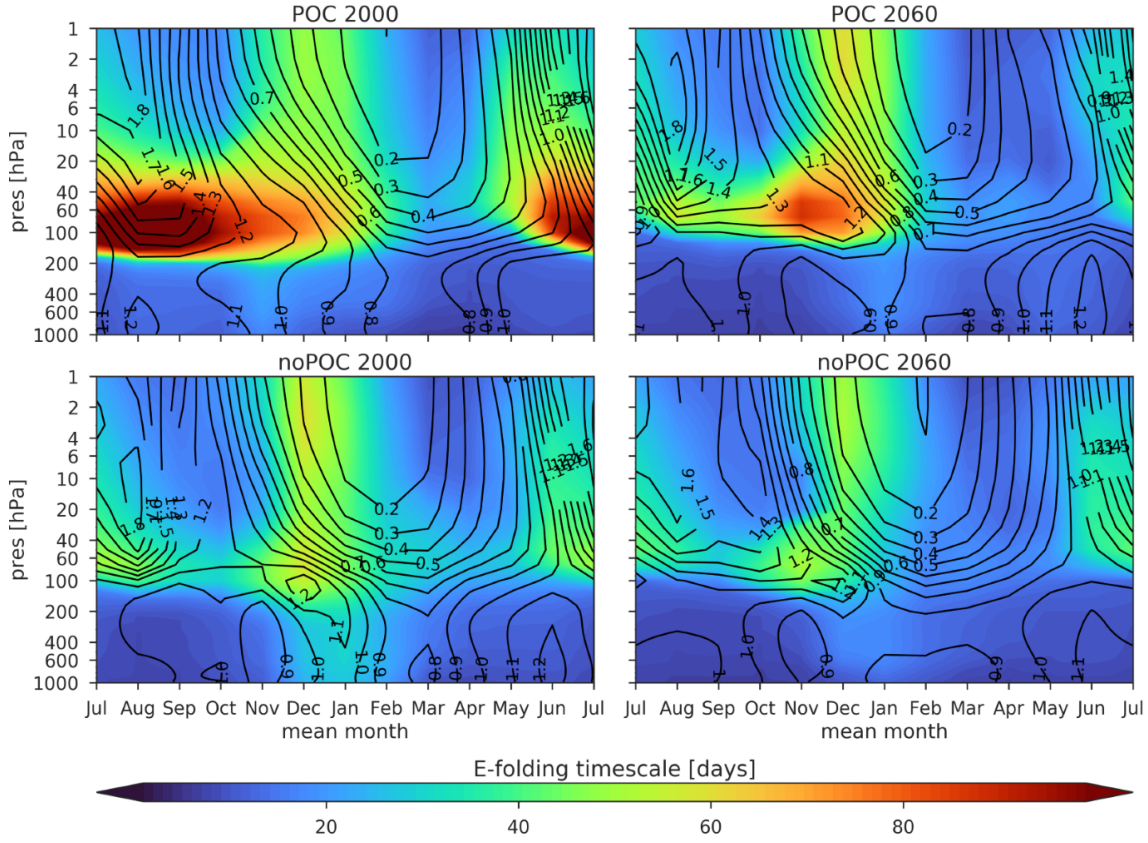

Figure 7.5: E-folding timescale of the SAM index [days] as a function of month and pressure for the POC 2000, noPOC 2000, POC 2060, and noPOC 2000 simulations. Contour lines represent the standard deviation of the SAM index.

limited intraannual variability. Further, a drop in e-folding timescale length is identified after the final warming. This hints at little influence of the vortex strength on the state of summertime circulation.

Tropospheric e-folding timescales are generally shorter and reach a maximum of around 20 days in November and December. Tropospheric maxima are visible during the period of highest variability in the lowermost stratosphere, consistent with the assumption that large and persistent stratospheric SAM anomalies can lead to persistent tropospheric anomalies of the same sign as proposed by Baldwin et al. (2003).

The ICON-ART simulations exhibit a similar overall structure as the ERA5 dataset, with higher e-folding timescales in the stratosphere than in the troposphere. The longest timescales are detected in summer for tropospheric and stratospheric levels. The stratospheric maximum detected from August to November in the ERA5 dataset is, however, not detected in all ICON-ART simulations.

The POC 2000 simulation shows the highest stratospheric e-folding timescales of all ICON-ART simulations with a pronounced maximum reaching e-folding timescales longer than 100 days between July and October for levels between 150 and 50 hPa. This maximum occurs during the period of highest variability at those levels, indicating strong and persistent SAM anomalies that can likely influence the troposphere. Tropospheric maxima are visible in November, slightly before the tropospheric ERA5 maximum. Compared to the ERA5 dataset, the POC 2000 simulation shows a maximum that is limited to a smaller altitude range. Above 20 hPa, significantly shorter timescales are detected in the ICON-ART simulations. This is consistent with the generally higher variability of the jet in those altitudes that was detected in the results of the standard deviation and is also visible in the higher explained variance of the POC 2000 simulations at those altitudes. At altitudes between 150 and 50 hPa, the detected maximum is overestimated and shifted to earlier dates compared to the ERA5 dataset. This finding is consistent with the prolonged persistence of the polar vortex in the lower stratosphere that was described in the chapter 5. The prolonged persistence of the vortex is also visible in the later transition to shorter timescales in February.

The noPOC 2000 simulation shows significantly shorter e-folding timescales in winter and spring between 150 and 50 hPa compared to the POC simulation, corresponding with a decrease in the persistence of vortex strength. This decrease in persistence can be associated with the earlier vortex breakup in the noPOC simulation. Tropospheric e-folding timescales reach a maximum between December and February that is increased to 30 days.

The POC 2060 and noPOC 2060 simulations generally show shorter e-folding timescales than the corresponding 2000 simulations. The POC 2060 simulation shows a similar SAM persistence as the POC 2000 simulation in November and December. However, the strong maximum between July and October is not detected. The stratospheric temporal structure of the noPOC 2060 simulation closely resembles the structure of the noPOC 2000 simulation.

Overall, we observe shorter stratospheric e-folding timescales for the noPOC simulations compared to the POC simulations and shorter stratospheric e-folding timescales for 2060 than for 2000. This finding is in agreement with Dennison et al. (2015) but in contrast to the study by Gerber et al. (2010) who did not observe significant changes in the e-folding timescale between the 20th and 21st century.

Compared to the ERA5 dataset, ICON-ART underestimates upper stratospheric maxima. The e-folding timescale in the lower and middle stratosphere is highly dependent on the model simulation, including experiments with higher maximum values as well as experiments with lower maximum values than the ERA5 dataset. Further, the ICON-ART simulations slightly overestimate tropospheric values.

A direct comparison between the ICON-ART simulations and the ERA5 dataset is difficult due to the different characteristics of the datasets. The ICON simulations were performed in a timeslice setup and include 65 realizations. In contrast, the ERA5 dataset is a 29-year long transient reanalysis dataset. Further, the ERA5 dataset includes years with different amounts of ozone-depleting substances and GHGs, while the ICON-ART simulations work with fixed boundary conditions and polar ozone chemistry switched on or off. However, the model results suggest that different boundary conditions and the ozone hole can significantly influence the e-folding timescales. Further, the calculation of e-folding timescales can be influenced by the length of the analyzed time series, as will be discussed later in this chapter. The detected overestimation of e-folding timescales in the model simulations could partly occur due to the interpolation of the ICON-ART output data, which is available every three days, to a daily sampling. The impact of this interpolation is analyzed in section 7.1.4. Nevertheless, the comparison of the model with the ERA5 dataset shows that ICON-ART is able to simulate the general temporal structure and range of the identified e-folding timescales.

Large and persistent SAM anomalies in the lower stratosphere can influence the tropospheric SAM and induce large and persistent anomalies there (e.g. Baldwin et al., 2003). In this section, large e-folding timescales were detected in the lower stratosphere that coincided with large variability, thus indicating strong and persistent SAM anomalies in these altitude regions. However, e-folding timescales are significantly decreased for the 2060 simulations. This decrease in persistence could influence the stratospheric impact on the tropospheric SAM, and thus on surface climate, in the future. High tropospheric e-folding timescales are associated with high variability in the lowermost stratosphere in all ICON-ART simulations and ERA5. This indicates an influence of stratospheric anomalies on the troposphere. To further investigate the stratospheric impact on the surface, a prediction value was calculated that is discussed in the next section.

7.1.3 Predictability

The prediction value indicates how well the monthly mean SAM at 850 hPa is predicted by the SAM index at different altitudes a month before. It is a measure of how strongly the 850 hPa SAM is affected by SAM anomalies at different altitudes. A high stratospheric prediction value indicates that the stratospheric influence on the surface SAM one month later is large, while a low value indicates only a weak influence. A detailed description of the prediction values' calculation can be found in section 4.4.2. The results for the ERA5 dataset are shown in Figure 7.6, the results for the ICON-ART simulations are depicted in Figure 7.7.

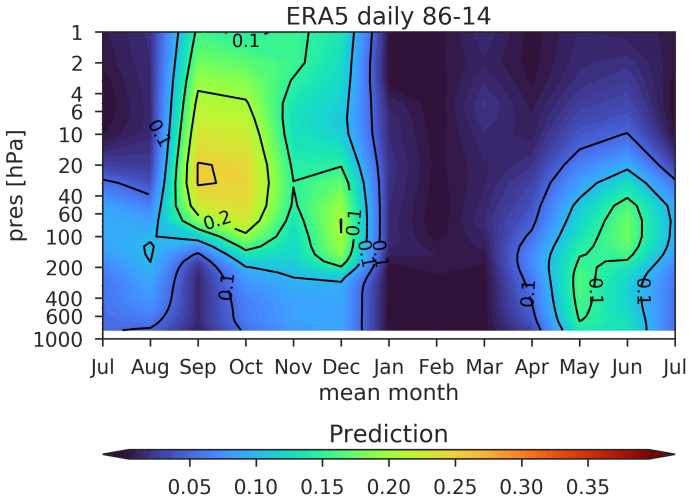

Figure 7.6: Predictability of the 30-day mean 850 hPa SAM index as a function of month and pressure for detrended daily ERA5 data for 1986 - 2014. The predictability is defined by the fraction of variance of the 30-day mean 850 hPa SAM index with a lead time of 25 days that is linearly correlated with the instantaneous SAM index at a given time and pressure level.

For ERA5, the prediction value shows increased stratospheric values between August and December, with the highest values in September. This indicates that for the given period, the stratospheric annular mode index is a better predictor for the state of the near-surface monthly mean annular mode than the annular mode near the surface itself. This observation suggests a stratospheric influence on the troposphere during this time of year. The high prediction values correspond with the long persistence in the lower stratosphere detected in the previous sections. For the rest of the year, stratospheric prediction values are either similar or smaller than the tropospheric values, and thus less stratospheric influence is detected.

The POC 2000 simulation is characterized by high prediction values and an extended period of high stratospheric predictability from June until January. Similar to the ERA5 dataset, two individual stratospheric maxima are visible: a stronger maximum in August

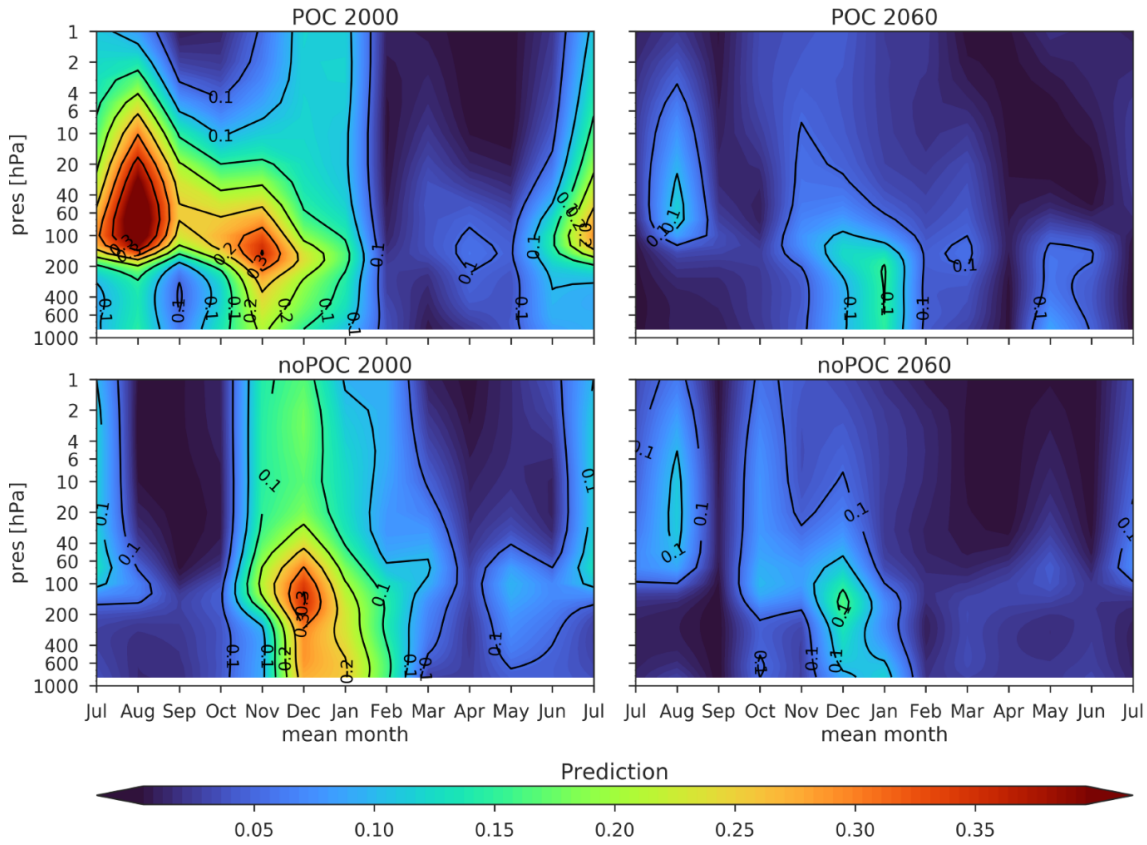

Figure 7.7: As Figure 7.6 but for the POC 2000, noPOC 2000, POC 2060, and noPOC 2000 simulations.

(September for ERA5) and a weaker maximum in November (December for ERA5) located at slightly lower levels.

The noPOC 2000 simulation shows a different period of high stratospheric predictability that is limited to November to February and a weaker maximum in July. Compared to ERA5 and the POC 2000 simulation, tropospheric predictability is increased from December to February.

The POC and noPOC 2060 simulations show a significant decrease in stratospheric prediction compared to ERA5 and the ICON-ART 2000 simulations. Tropospheric prediction is also decreased compared to the 2000 simulations. However, less distinct maxima are still visible in December and January.

The maximum prediction values for the ERA5 dataset and the ICON-ART simulations coincide with the detection of persistent e-folding timescales and large variability, as shown in the previous sections. Therefore the prediction value supports the assumption that large and persistent stratospheric SAM anomalies can influence the surface SAM. The predictability calculations for the ICON-ART simulations suggest that the stratospheric influence on tropospheric climate is significantly decreased for the future simulations. Surface SAM anomalies are associated with characteristic temperature and precipitation anomalies for large parts of the southern hemisphere (e.g. Gillett et al., 2006). Conse-

quently, a reduced predictability of the tropospheric SAM will likely affect the efficiency of extended-range weather forecasts in the future.

7.1.4 Uncertainties in the calculation of standard deviation, e-folding timescale, and prediction

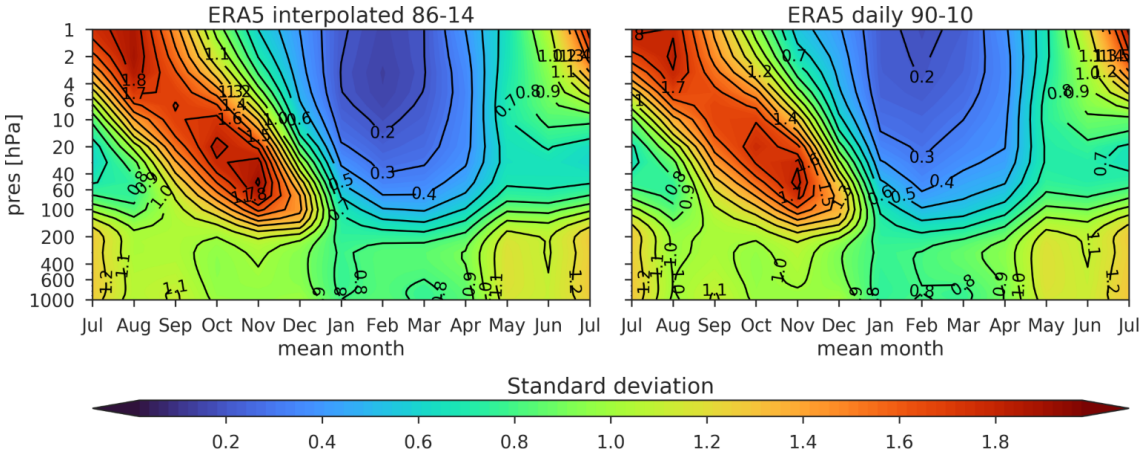

Figure 7.8: Standard deviation of the SAM index as a function of month and pressure for detrended daily ERA5 data obtained by linear interpolation from data every 3 days for the period 1986 - 2014, and detrended daily ERA5 data for the period 1990 - 2010.

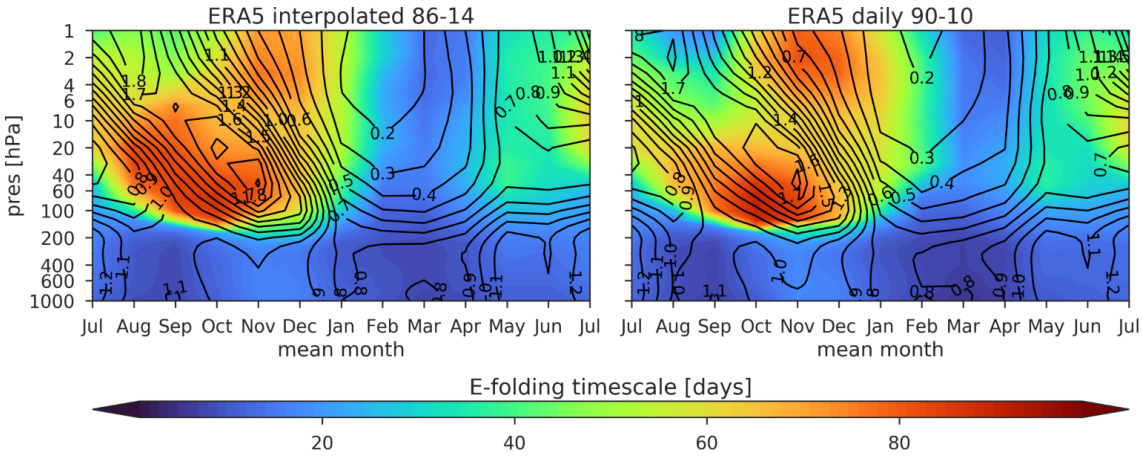

Figure 7.9: E-folding timescale of the SAM index [days] as a function of month and pressure for detrended daily ERA5 data obtained by linear interpolation from data every 3 days for the period 1986 - 2014, and detrended daily ERA5 data for the period 1990 - 2010. Contour lines represent the standard deviation of the SAM index.

In this section, uncertainties in the calculation of standard deviation, e-folding timescales, and the prediction values are investigated based on ERA5 data.

ERA5 data in this study is used with a daily resolution, while the ICON-ART datasets are only available every three days. For calculating standard deviation, e-folding timescales, and prediction, the ICON-ART datasets were linearly interpolated to a daily sampling. To evaluate this effect on the calculation of the characteristics, ERA5 data were processed by

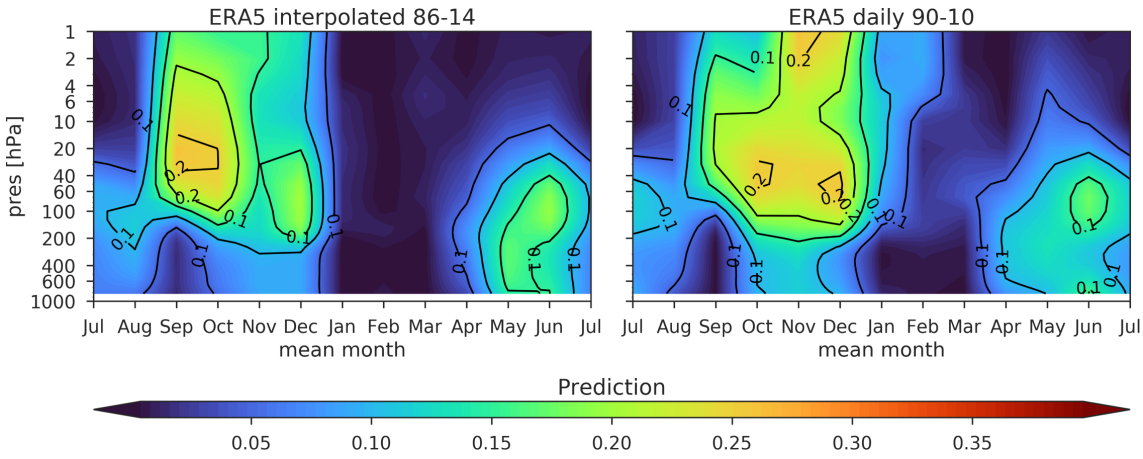

Figure 7.10: Predictability of the 30-day mean 850 hPa SAM index as a function of month and pressure for detrended daily ERA5 data obtained by linear interpolation from data every three days for the period 1986 - 2014, and detrended daily ERA5 data for the period 1990 - 2010. The predictability is defined by the fraction of variance of the 30-day mean 850 hPa SAM index with a lead time of 25 days that is linearly correlated with the instantaneous annular mode at a given time and level.

choosing a subset of data with a resolution of 3 days that was interpolated to daily data again in the next step.

The results for the interpolated ERA5 dataset are shown in Figure 7.8 for the standard deviation, Figure 7.9 for the e-folding timescales and in Figure 7.10 for the prediction calculation. They are compared with the results of the ERA5 dataset with a daily resolution that are shown in the Figures 7.2 (standard deviation), 7.4 (e-folding timescales) and 7.6 (predictability).

For the standard deviation, only minor changes are visible. The e-folding timescales for the daily and interpolated ERA5 datasets show an identical pattern with slightly increased values of a few days for the calculation based on the interpolated data. Similarly, the prediction pattern remains very similar, while slightly higher values are observed for the calculation based on interpolated data.

Further, Kim and Reichler (2016) investigated the uncertainties in e-folding timescale calculations for different dataset lengths. Their results indicate deviations of the SAM e-folding timescale around 25 % for 20 year long datasets and a decrease in uncertainty for longer datasets. Here, we analyzed the differences in standard deviation, e-folding timescale, and prediction between the ERA5 datasets from 1986 - 2014 and 1990 - 2010 to estimate structure and magnitude changes. The results for the 1990 - 2010 ERA5 dataset are shown in Figure 7.8 for the standard deviation, Figure 7.9 for the e-folding timescales and in Figure 7.10 for the prediction calculation. They are compared with the results of the ERA5 dataset including the years 1986 - 2014 that are shown in the Figures 7.2 (standard deviation), 7.4 (e-folding timescales), and 7.6 (predictability).

The standard deviations show a similar structure with a decrease in amplitude in the stratosphere and a slight increase in the troposphere for the shorter dataset. The e-folding timescales show a similar temporal structure at all levels. In the upper stratosphere, the maximum between November and January is stronger, while the minimum from July to September is weaker. Further, the lower stratospheric maximum is slightly higher but also more confined to lower levels and dates between September and November for the shorter ERA5 dataset. Changes in prediction are characterized by a decrease in predictability in September and an increase from October to February at stratospheric levels for the shorter dataset. Also, an increase in the troposphere is detected in October and November.
Overall uncertainties due to temporal resolution differences are comparably small, with interpolated data showing a slight bias towards longer e-folding timescales and higher predictability. Varying the analyzed dataset's length resulted in weak changes of standard deviation and e-folding timescales and more pronounced changes in stratospheric prediction structure. Consequently, the interpolation of the ICON-ART output that is available every three days can lead to a slight overestimation of e-folding timescales and the prediction value. However, the detected magnitude of potential biases is small and does not significantly affect the comparison with the ERA5 dataset. Differences in the length of the analyzed datasets can have a larger impact on the comparison with the prediction value differing in the observed structure. However, the general characteristics of the calculations are robust for the calculation with different time series. Consequently, a comparison of the 29-year long ERA5 dataset with the ICON-ART timeslice simulations is feasible to identify if the general characteristics of the reanalysis dataset are represented in the model.

7.2 Near-surface temperature signals due to changes in the SAM

Climatological surface temperature changes are often associated with a shift of the near-surface Southern Annular Mode index. In this section, we analyze the temperature changes that are in conjunction with shifts in the SAM in the ICON-ART simulations. To detect the SAM's influence on surface temperatures, daily summertime near-surface temperature anomalies were regressed on the daily summertime near-surface SAM indices that were obtained from a merged SAM calculation as described in section 4.3.4.
Due to Antarctica's orography, with altitudes up to 3000 m, surface pressure in the southern hemisphere differs significantly between oceanic regions and elevated regions as the Antarctic Plateau, where a surface pressure of around 600 hPa is observed. The 600 hPa pressure level was therefore chosen as the near-surface level for the SAM calculation.
The merged annular mode calculation is based on the two model experiments that are compared. Both model experiments are used to define a common climatology that is

used to calculate the geopotential anomalies. In the next step, PCA is applied to the geopotential anomalies of both runs, resulting in one annular mode pattern for both runs. Each of the two runs is characterized by an individual annular mode index time series. Now, the climatological distribution of the SAM indices for both runs can be compared. The shift of the SAM between the two runs is then characterized by the difference of the mean SAM indices of the individual runs.
Further, the pattern of temperature changes that are associated with the SAM was obtained by the regression of daily summertime near-surface temperature anomalies on the daily summertime 600 hPa SAM index of the merged SAM calculation. The magnitude of near-surface temperature changes associated with climatological changes of the SAM was then obtained by weighting the resulting pattern with the shift detected in the SAM indices. An overview of the calculation procedure is given in Figure 7.11.

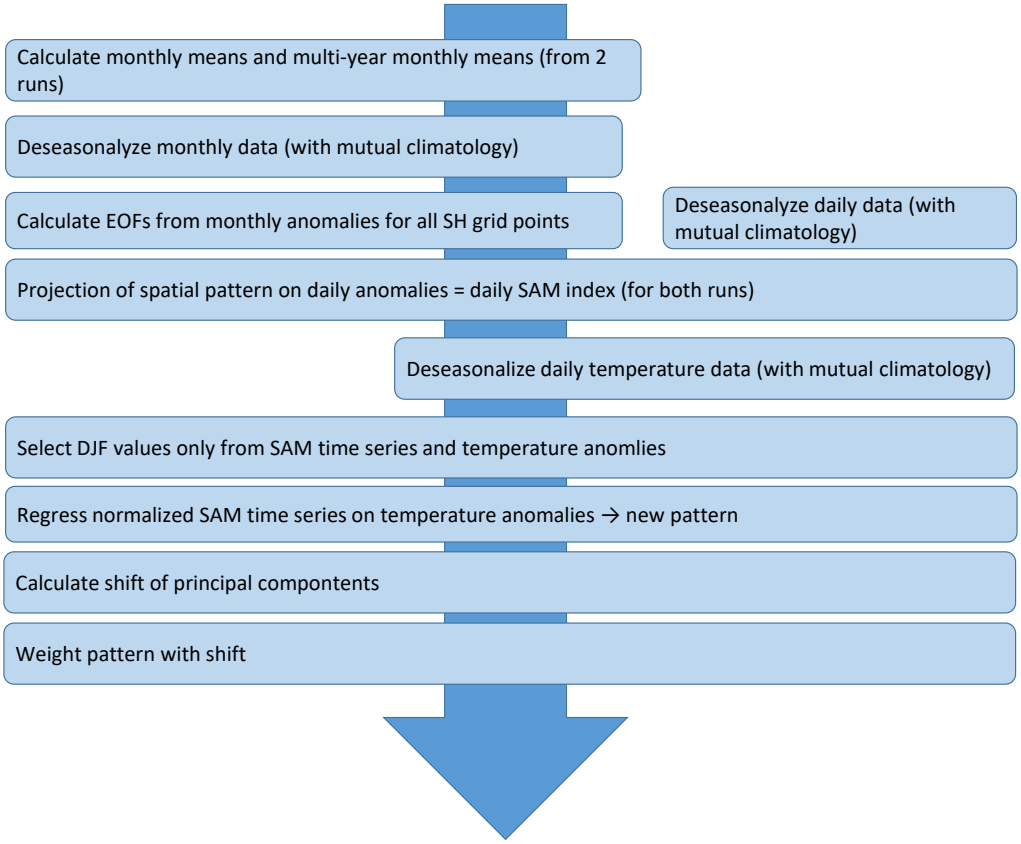

Figure 7.11: Workflow for the calculation of SAM associated near-surface temperature changes.

The near-surface temperature change signal associated with the climatological shift of the 600 hPa SAM between the POC 2000 and noPOC 2000 simulations (Fig. 7.12) is characterized by a temperature decrease south of 70°S that is particularly strong in the center of the Antarctic Plateau. In contrast, warming is observed for the Antarctic Peninsula and the Southern Ocean between 70 and 50°S with three local maxima at 45°W, 45°E and

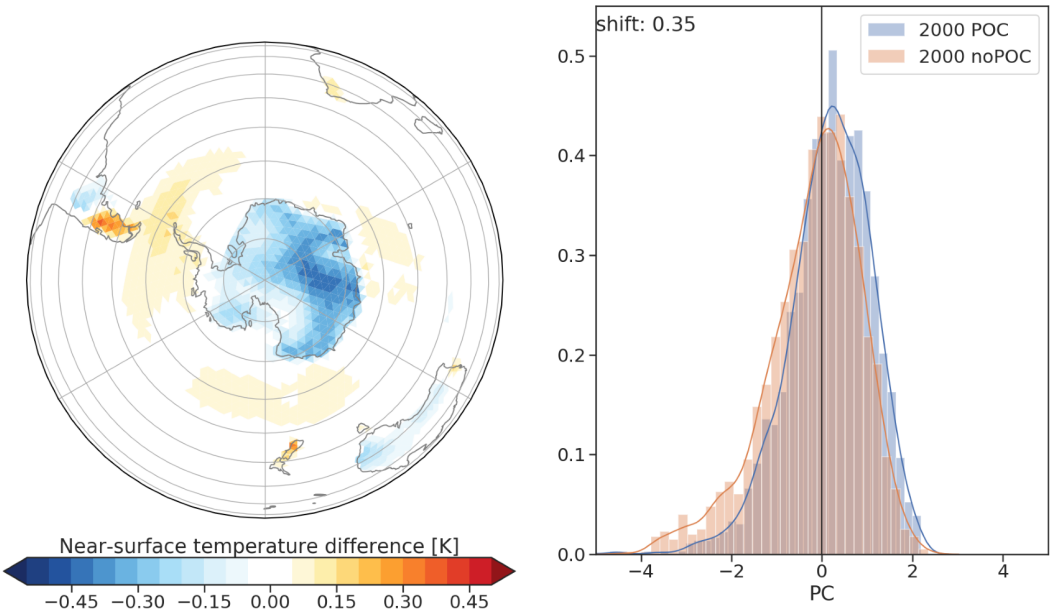

Figure 7.12: Near-surface temperature change signal associated with the climatological shift of the 600 hPa SAM and distribution of the SAM indices for the POC 2000 and noPOC 2000 simulations.

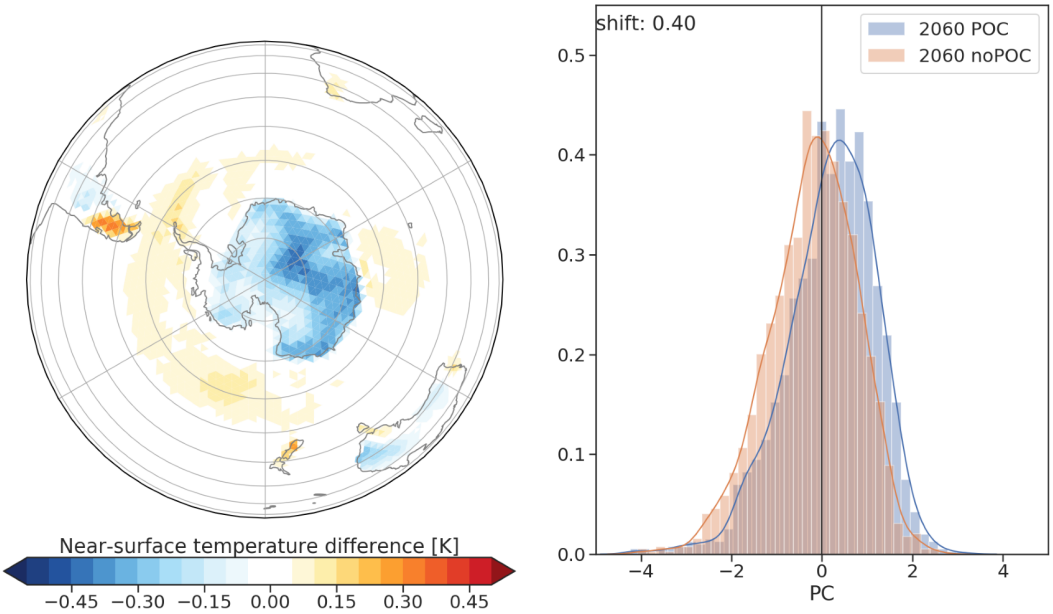

Figure 7.13: Near-surface temperature change signal associated with the climatological shift of the 600 hPa SAM and distribution of the SAM indices for the POC 2060 and noPOC 2060 simulations.

180°E. North of 50°S, changes are only apparent for land grid points with a warming of New Zealand, Tasmania, and the southern tip of Africa, as well as Patagonia. A temperature decrease is detected for most of Australia, as well as the region north of Patagonia. The magnitude of changes is characterized by the climatological shift of the SAM indices between the POC and noPOC 2000 simulations. The mean SAM index of the POC 2000 simulation is shifted by 0.35, resulting in typical temperature changes of 0.2 - 0.4 K for inner Antarctica and a warming up to 0.15 K for the Antarctic Peninsula and the Southern Ocean.

The temperature anomaly pattern detected for the changes between the POC and noPOC 2060 (Fig. 7.13) is comparable to the pattern observed for the 2000 comparison. A slight change in the location of maxima in the Southern Ocean is detected. For the 2060 comparison, a shift of 0.4 is detected. Even though the detected shift is higher for the 2060 comparison, the magnitude of temperature anomalies associated with the shift of the SAM is comparable for both time horizons. This hints at a weaker impact of the SAM on surface temperature changes for the 2060 comparison.

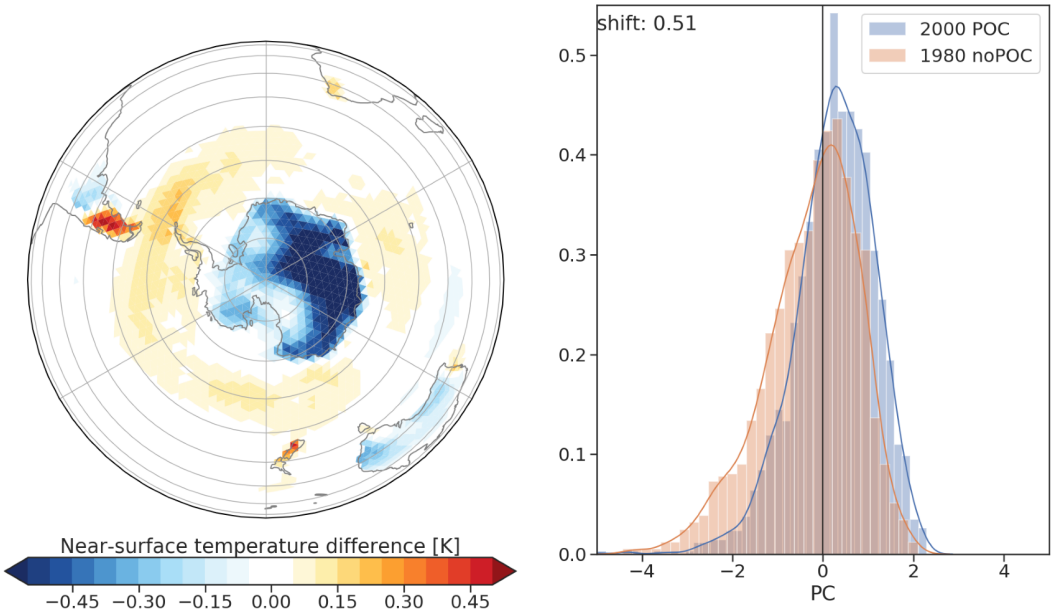

Figure 7.14: Near-surface temperature change signal associated with the climatological shift of the 600 hPa SAM and distribution of the SAM indices for the POC 2000 and noPOC 1980 simulations.

The mean SAM indices for the POC 2000 and noPOC 1980 simulations (Fig. 7.14) show a higher shift of 0.51 than SAM indices associated with changes in polar ozone chemistry for the years 2000 or 2060. Thus, changes in boundary conditions are responsible for an additional change in the SAM index. This finding is of particular interest since changes in observed near-surface temperatures are often attributed to changes in the near-surface

SAM induced by polar ozone depletion. However, additional small changes in boundary conditions can alter the detected signal's strength. The detected temperature pattern for this scenario is similar to the pattern detected for the impact of polar ozone depletion. The stronger shift thus results in a stronger temperature signal, reaching more than 0.5 K temperature decrease for East Antarctica and up to 0.25 K temperature increase at the Southern Ocean.

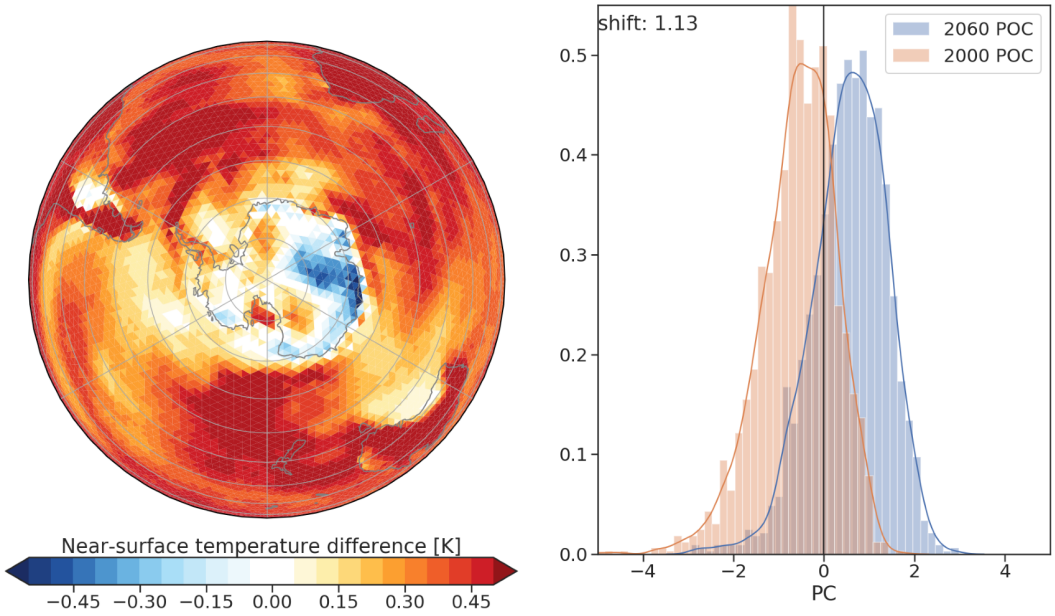

Figure 7.15: Near-surface temperature change signal associated with the climatological shift of the 600 hPa SAM and distribution of the SAM indices for the POC 2060 and POC 2000 simulations.

A positive shift of the SAM is expected for increased GHGs. This influence of changes in boundary conditions was detected in addition to the changes induced by polar ozone depletion for the comparison of the POC 2000 and noPOC 1980 simulations. The influence of increased GHGs on the near-surface SAM and the corresponding temperature patterns is further investigated by the comparison of model simulations for the years 2000 and 2060. The comparison between the POC simulations of the years 2060 and 2000 (Fig. 7.15) shows a large difference in the climatological distribution of the SAM indices, resulting in two distinct populations. Consequently, a strong shift of the mean SAM indices of 1.13 is detected. The strong shift can partly be attributed to the altered structure of the annular mode pattern as described in section 4.3.4. The strong shift between both simulations also influences the SAM-associated temperature pattern. The pattern is characterized by positive temperature anomalies north of 65°S. This positive correlation can be interpreted as the result of general tropospheric warming combined with the strong shift of the SAM indices. Positive SAM indices are predominantly detected for the 2060

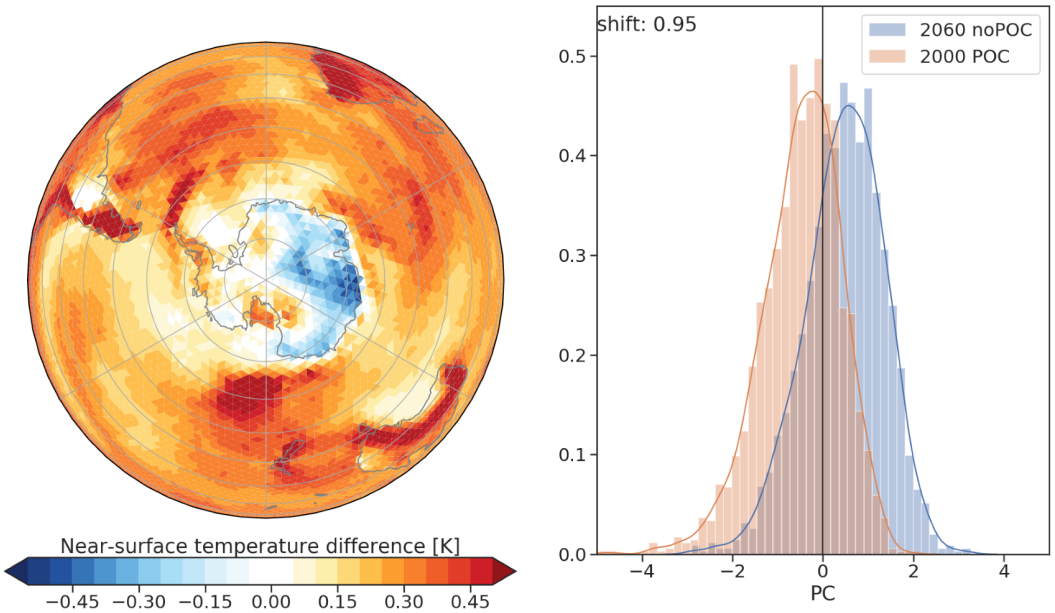

Figure 7.16: Near-surface temperature change signal associated with the climatological shift of the 600 hPa SAM and distribution of the SAM indices for the noPOC 2060 and noPOC 2000 simulations.

simulation, while negative SAM indices occur predominantly for the 2000 simulation. Thus, positive indices are associated with increased temperature in regions where the SAM's influence is small. This effect should be kept in mind for the interpretation of temperature patterns associated with changes in annular modes.

Besides the strong warming pattern, visible for most grid points, that is likely produced by the temperature changes due to increased GHGs, a cooling is visible for various Antarctic grid points, particularly for the coastal regions and East Antarctica. Here a strong negative temperature anomaly was already detected as a result of a shift of the SAM towards more positive values due to polar ozone depletion. Further, the region north of Patagonia and the eastern tip of Australia are displaying a significantly weaker temperature anomaly than surrounding grid points, coinciding with the regions of negative temperature anomalies for the ozone hole effect. Thus the observed temperature pattern for the POC 2060 and POC 2000 comparison can be interpreted as a superimposed anomaly pattern due to tropospheric warming and the temperature anomaly pattern that is actually resulting from changes in the SAM indices. Regions with a positive temperature response due to a shift of the SAM indices are therefore not particularly visible.

This assumption is further supported by the analysis of the SAM-associated temperature pattern for the noPOC 2060 and POC 2000 simulations (Fig. 7.16). For this scenario, the positive shift of the SAM indices due to increased GHGs is expected to be counteracted by a negative shift of the SAM indices due to the ozone hole's recovery. The calculated shift

in the 600 hPa SAM index is decreased to 0.95 for this scenario. The resulting temperature anomaly pattern is similar to the POC comparison; however, the positive temperature anomalies north of 65°S are significantly smaller. This can only partly be explained by the weaker shift. Therefore, for this scenario, a shift of the SAM indices of comparable strength as for the POC scenario is associated with a weaker temperature increase. This can be interpreted as the result of the less distinct SAM populations. Therefore positive indices are not as strongly associated with the 2060 simulation as this was the case for the POC comparison. This results in a weaker correlation with the temperature anomalies induced by GHG changes and, therefore, a weaker temperature anomaly pattern for regions that are not typically affected by changes in the SAM index.

The temperature signal patterns for the climate change scenarios underline the need for a critical interpretation of the results.

7.3 Conclusions

Climate change signals due to ozone depletion and recovery, as well as GHGs, are often associated with changes in the SAM. Therefore a realistic representation of the SAM climatology is important for accurate recent and future climate projections. In this chapter, the temporal structure of the SAM for the various ICON-ART simulations was compared with the structure obtained from the detrended ERA5 dataset for the years 1986 - 2014.

The variability of the SAM showed similar results for the ICON-ART and ERA5 datasets, with low variability in summer and high variability in winter in the stratosphere, consistent with the occurring wind speeds. Stratospheric easterlies are associated with low variability, while westerlies below a certain threshold are associated with increased variability (e.g. Thompson and Wallace, 2000). While the highest variability in the ERA5 dataset is associated with the breakup of the polar vortex, the ICON-ART simulations show significantly increased variability for the strength of the polar vortex throughout winter. The comparison of the POC and noPOC simulations shows a delayed shift to low variability in summer that is consistent with the delayed vortex breakup for the POC simulations and consistent with the results by Gerber et al. (2010).

The persistence of the SAM was analyzed based on the e-folding timescale, a measure commonly used as a benchmark for climate models. Stratospheric e-folding timescales are largest in winter and spring in the ERA5 dataset, indicating a persistent strength of the polar vortex, i.e., a strong vortex likely remains strong during winter, while a weak vortex likely remains weak. A drop in persistence after the final warming hints at little influence of the vortex strength on the summertime circulation. The tropospheric e-folding timescales are significantly smaller than the stratospheric e-folding timescales and show a maximum in late spring and early summer. During that time of year, the variability

of the SAM in the lower stratosphere is highest, thus indicating that large stratospheric anomalies can have an impact on the tropospheric e-folding timescale.
While the ICON-ART simulations agree with the overall structure detected for the ERA5 dataset, they show a decreased timescale in the upper stratosphere in winter that is indicating an increased variability of the polar night jet. Simulations with polar ozone chemistry show significantly higher stratospheric e-folding timescales than simulations without polar ozone chemistry. Further, the simulations with the year 2060 show decreased e-folding timescales compared to the 2000 simulations. This finding is in contrast to Gerber et al. (2010) that found no significant change in e-folding timescales between recent and future climate simulations. However, Dennison et al. (2015) found indications that ozone depletion and GHGs can have an impact on the length of e-folding timescales. As strong and persistent stratospheric SAM anomalies can affect the tropospheric SAM, a decrease in e-folding timescales is expected to influence the surface.
The stratospheric SAM's index on the surface was analyzed based on the prediction calculation. Consistent with the decreased e-folding timescales detected for the 2060 simulations, the predictability decreased significantly for those simulations compared to the 2000 simulations. As surface SAM anomalies are associated with significant temperature and precipitation anomalies across the southern hemisphere, the decrease in predictability will likely influence the efficiency of extended-range weather forecasts in the future.
A realistic representation of e-folding timescales in climate models is particularly important as they can influence the SAM's response to external forcing (e.g. Gerber et al., 2008b). Comparison with the ERA5 dataset showed an overestimation of stratospheric e-folding timescales for the POC 2000 simulation and an underestimation of stratospheric e-folding for the noPOC 2000 simulation. Simulated tropospheric e-folding timescales for the POC 2000 simulation agree with the ERA5 dataset. The noPOC 2000 simulation shows slightly higher tropospheric e-folding timescales in summer. Consequently, a stratospheric bias in e-folding timescales does not necessarily result in tropospheric biases. Further, the overestimation of tropospheric e-folding timescales is not caused by an overestimation of stratospheric e-folding timescales. This finding agrees with the study by Simpson et al. (2011) suggesting that an overestimation of stratospheric e-folding timescales does not necessarily result in prolonged tropospheric e-folding timescales.
The overestimation of the tropospheric e-folding timescales can partly be attributed to the interpolation of the ICON-ART output with a resolution of three days to a daily resolution. Further reasons for the detected differences can be the different lengths of the datasets (Kim and Reichler, 2016) and the different resolutions of the model and the ERA5 data (Gerber et al., 2008b; Osprey et al., 2010). Additionally, as for the previous analyses, a detailed comparison between the transient ERA5 data and the ICON-ART timeslice simulations is not feasible due to differences in the experimental setup. Overall, tropospheric e-folding timescales are well represented in the ICON-ART simulations

in contrast to previous modeling studies, where tropospheric e-folding timescales were commonly overestimated (e.g. Gerber et al., 2008a, 2010; Osprey et al., 2010).

After analyzing the SAM's representation in the model simulations, the near-surface temperature changes that were associated with a shift of the near-surface SAM were investigated. The pattern associated with changes in near-surface SAM indices towards more positive values shows a warming of the Antarctic Peninsula, Patagonia, New Zealand, and the Southern Ocean, while cooling is detected for Australia and the remaining parts of Antarctica. This pattern is consistent with the findings by Thompson and Solomon (2002), Gillett et al. (2006) and Marshall (2007). Comparing the SAM-associated temperature changes with the actual near-surface temperature changes detected in the model comparing the POC and noPOC 2000 simulations, a significantly smaller fraction of the temperature change is explained by the SAM than the previous study by Thompson and Solomon (2002) suggested. This could partly be explained by the different seasons considered. Thompson and Solomon (2002) investigated changes between December and May, while this study focuses on December to January. The study by Marshall et al. (2006) suggests that the correlation between changes in the SAM and near-surface temperature changes is significantly higher in autumn than in the summer season. Consequently, the Antarctic summertime temperature changes in the simulations are not entirely driven by changes in the SAM. Therefore, future studies are required to identify other mechanisms that influence the temperature signals during this season.

Changes in the near-surface SAM are characterized by a shift towards more positive values for the simulations with polar ozone chemistry consistent with previous studies (e.g. Karpechko et al., 2010; Fogt et al., 2009; Miller et al., 2006). Further, simulations of future climate, and thus for increased GHG forcing, result in a shift towards more positive values as well. The comparison of the noPOC 2060 simulation and the POC 2000 simulation results in a decreased shift of the SAM compared to the GHG effect only. This result is consistent with the counteracting effects of ozone recovery and GHG-induced changes on the SAM as detected in previous studies (e.g. Shindell, 2004; Staten et al., 2012). Our results suggest that the GHG-induced shift is significantly higher than the counteracting effect of ozone recovery, thus resulting in a significant shift of the SAM towards higher values even with ozone recovery. However, as explained in the previous section, the SAM calculations for different time horizons can be biased significantly by the underlying climatologies of geopotential. Therefore a calculation of the SAM taking into account changes in the underlying climatologies is desirable for a meaningful interpretation of the magnitude of changes in the SAM between recent and future climate.

8 Conclusions and Outlook

Here, idealized multi-decadal ICON-ART timeslice simulations with an interactive ozone scheme have been performed to investigate the influence of polar ozone loss and recovery on the climate system. In this study, an experimental setup was designed to allow for the analysis of ozone hole induced signals separated from other perturbations of the climate system and that is well suited to characterize the internal variability of the signals.

Evaluation of the timeslice simulation for the year 2000 with polar ozone chemistry and for 1980 without polar ozone chemistry showed that the simplified ozone chemistry scheme Linoz is able to realistically capture the typical evolution of the Antarctic ozone hole, the climatological total column ozone distribution, and vertical profiles of ozone and temperature. The model shows a prolonged persistence of the polar vortex. Comparison with other models demonstrates, however, that this behavior is detected for various chemistry-climate simulations. Generally, the model validation showed that the Linoz scheme is suited for the investigation of ozone hole induced climate change signals due to its good representation of climatological ozone concentrations with and without the ozone hole. Further, comparison with other studies indicated that models with a full chemistry scheme do not necessarily result in a better representation of ozone concentrations. The reduced computational cost of a simplified scheme compared to full chemistry schemes enabled the performance of long timeslice integrations with interactive ozone that are suited for the analysis of internal variability.

Analysis of the ozone hole induced climate change signals showed a cooling of the polar lower stratosphere and warming above and a prolonged persistence of the polar vortex consistent with previous studies. The magnitude of the changes was larger than most previous studies but consistent with the study by Keeble et al. (2014) that performed timeslice integrations with a comprehensive and interactive ozone calculation. Thus, the model results suggest that the magnitude of the detected signals is underestimated when ozone is not calculated interactively with a comprehensive or simplified ozone scheme, but a prescribed ozone climatology is used.

Polar ozone depletion leads to a shift of the tropospheric midlatitude jet towards higher latitudes in summer. This shift is accompanied by a warming of the Antarctic Peninsula, Patagonia, and parts of East Antarctica, while a cooling is detected for West Antarctica and the coastal areas of East Antarctica. This temperature pattern is more complex than derived in previous studies, independent of their representation of ozone, that observed

a warming of the Antarctic Peninsula and a cooling of the rest of Antarctica that was attributed to a shift of the SAM.

Taking into account changes in greenhouse gases in addition to the effect of ozone depletion resulted in a slightly stronger near-surface temperature signal for recent climate change. This indicates that GHG changes have influenced recent southern hemispheric climate change signals. In the future, the increase in GHGs will have a strong impact on surface climate. For the ICON-ART simulations, a strong near-surface warming throughout the year is observed considering changes in GHGs only. Considering ozone recovery in addition to the increase in GHGs shows an effect on zonal wind changes in summer. The changes induced by ozone recovery counteract the GHG-induced changes, resulting in only small circulation changes during summer. The observed temperature signal is, however, only weakly influenced by ozone recovery. This results mainly from the larger magnitude of tropospheric warming due to increased greenhouse gases compared to the ozone recovery signal. Further, analysis of the uncertainties for the near-surface temperature signals resulted in smaller uncertainties for ocean-associated grid points. This indicates that prescribed sea surface temperatures act as strong lower boundary conditions that can reduce the near-surface temperature signal induced by atmospheric composition and circulation changes.

The ozone hole induced near-surface temperature pattern resulting from a shift of the near-surface SAM was calculated and shows a warming of the Antarctic Peninsula and the Southern Ocean and a cooling of inner Antarctica consistent with previous studies. However, the detected temperature signal and the SAM associated signal differ, indicating that the SAM has a weaker influence on near-surface temperature change than previously assumed. For future climate projections, a shift of the SAM towards more positive values is attributed to increased GHGs. This shift is counteracted by ozone recovery consistent with previous studies.

A correct representation of the SAM climatology, particularly the persistence of the SAM, is likely important for a realistic model response to external forcing. The ICON-ART simulations show an agreement with the ERA5 data in the troposphere, suggesting a realistic tropospheric response to GHG and ozone changes. Other modeling studies commonly overestimate the SAM's persistence in the troposphere, which could partly explain the stronger influence of the SAM in previous simulations.

Further, the analysis showed distinct differences in the SAM persistence for the different model simulations with shorter timescales for the POC simulations and shorter timescales for the 2060 simulations compared to the 2000 simulations. Persistent stratospheric SAM anomalies can influence the tropospheric SAM and thus surface climate. Therefore, a prediction value was used to investigate the skill of the SAM in different altitudes predicting the averaged near-surface SAM one month in advance. This calculation showed that there is a high stratospheric prediction skill for the 2000 simulations and a strong decrease

in stratospheric predictability for the 2060 simulations. The decreased stratospheric influence on the tropospheric SAM will likely decrease the efficiency of extended-range weather forecasts in the future.

Sensitivity studies with different tropospheric ozone lifetimes showed that stratospheric signals due to the ozone hole are robust and significant during spring and summer and show more variability in winter when the detected pattern is more variable and significance is only detected for some of the chosen tropospheric ozone lifetimes. The near-surface signals are only robust for summer, and signals show the highest number of significant grid points of all seasons. All other seasons show high variability of the detected circulation and temperature patterns. In winter and spring, when variability is the largest, the patterns strongly deviate even though a considerable number of significant grid points is detected for individual patterns. This result underlines the importance of a careful interpretation of climate change signals detected for different seasons and their attribution to the ozone hole.

Uncertainty estimation for different ensemble sizes further showed that timeslices with 20 realizations resulted in an uncertainty of around 50 % of the observed near-surface temperature change signal. Timeslice simulations with 65 realizations, as performed in this study, are able to decrease the uncertainty to around 20 %. Consequently, long timeslice integrations are important to exclude the effects of internal variability.

The comparison of this modeling study with other modeling and observational results is difficult due to the different experimental designs and the different resulting measures of climate change signals. Observational studies and transient model simulations calculate linear trends to characterize climate change signals, while timeslice simulations obtain the climatological difference for specific years. Larger climate signals detected in timeslice simulations could thus result from the nonlinearity of the climate change signals.

A systematic comparison of transient and timeslice simulations with the same modeling system could improve the understanding of differences that arise from changed experimental setups and would be valuable to increase the confidence in projections of recent and future climate change simulations. Moreover, long timeslice simulations with a similar experimental setup performed with multiple modeling systems are important to investigate the effect of internal variability further.

Further, different studies calculate linear trends or climatological differences based on different time averages. These time averages range from monthly means to seasonal means or even longer averaging intervals of up to six months. However, the model results presented in this study indicate that climate change signals associated with polar ozone depletion are limited to summer. Therefore, a closer investigation of the seasonality of climate change signals is desirable for future studies.

In this work, the fraction of summertime near-surface temperature changes induced by polar ozone depletion that is associated with changes in the SAM is smaller than for pre-

vious studies. However, the detected near-surface temperature changes show a robust pattern of warming and cooling. Therefore, additional research is needed to identify further processes causing the near-surface temperature change detected in the ICON-ART simulations.

Near-surface temperature changes associated with increased greenhouse gases show a similarity to the prescribed SSTs and low uncertainties for ocean grid points, indicating a significant impact of prescribed SSTs on the detected signal. For a more meaningful analysis of future and recent climate change, simulations with a coupled ocean would be desirable.

Bibliography

Andrews, D. G., J. R. Holton, and C. B. Leovy, 1987: *Middle atmosphere dynamics: An Introductory Text*, International geophysics series, Vol. v. 40. Acad. Press, Orlando.

Arblaster, J. M. and G. A. Meehl, 2006: Contributions of External Forcings to Southern Annular Mode Trends. *Journal of Climate*, **19 (12)**, 2896–2905, doi:10.1175/JCLI3774.1.

Arblaster, J. M., G. A. Meehl, and D. J. Karoly, 2011: Future climate change in the Southern Hemisphere: Competing effects of ozone and greenhouse gases. *Geophysical Research Letters*, **38 (2)**, doi:10.1029/2010GL045384.

Baldwin, M. P., D. B. Stephenson, and I. T. Jolliffe, 2009: Spatial Weighting and Iterative Projection Methods for EOFs. *Journal of Climate*, **22 (2)**, 234–243, doi:10.1175/2008JCLI2147.1.

Baldwin, M. P., D. B. Stephenson, D. W. J. Thompson, T. J. Dunkerton, A. J. Charlton, and A. O'Neill, 2003: Stratospheric memory and skill of extended-range weather forecasts. *Science*, **301 (5633)**, 636–640, doi:10.1126/science.1087143.

Banerjee, A., J. C. Fyfe, L. M. Polvani, D. Waugh, and K.-L. Chang, 2020: A pause in Southern Hemisphere circulation trends due to the Montreal Protocol. *Nature*, **579 (7800)**, 544–548, doi:10.1038/s41586-020-2120-4.

Benjamini, Y. and Y. Hochberg, 1995: Controlling the false discovery rate: a practical and powerful approach to multiple testing. *Journal of the Royal statistical society: series B (Methodological)*, **57 (1)**, 289–300, doi:10.1111/j.2517-6161.1995.tb02031.x.

Bodeker, G. E., J. Nitzbon, J. S. Tradowsky, S. Kremser, A. Schwertheim, and J. Lewis, 2020: A Global Total Column Ozone Climate Data Record. *Earth Syst. Sci. Data Discuss.*, doi:10.5194/essd-2020-218.

Braesicke, P., J. Keeble, X. Yang, G. Stiller, S. Kellmann, N. L. Abraham, A. Archibald, P. Telford, and J. A. Pyle, 2013: Circulation anomalies in the Southern Hemisphere and ozone changes. *Atmospheric Chemistry and Physics*, **13 (21)**, 10 677–10 688, doi:10.5194/acp-13-10677-2013.

Canziani, P. O., A. O'Neill, R. Schofield, M. Raphael, G. J. Marshall, and G. Redaelli, 2014: World Climate Research Programme Special Workshop on Climatic Effects of Ozone Depletion in the Southern Hemisphere. *Bulletin of the American Meteorological Society*, **95 (6)**, ES101–ES105, doi:10.1175/BAMS-D-13-00143.1.

Chapman, S., 1930: XXXV. On ozone and atomic oxygen in the upper atmosphere. *The London, Edinburgh, and Dublin Philosophical Magazine and Journal of Science*, **10 (64)**, 369–383, doi:10.1080/14786443009461588.

Chapman, W. L. and J. E. Walsh, 2007: A Synthesis of Antarctic Temperatures. *Journal of Climate*, **20 (16)**, 4096–4117, doi:10.1175/JCLI4236.1.

Chiodo, G. and L. M. Polvani, 2017: Reduced Southern Hemispheric circulation response to quadrupled CO_2 due to stratospheric ozone feedback. *Geophysical Research Letters*, **44 (1)**, 465–474, doi:10.1002/2016GL071011.

Crook, J. A., N. P. Gillett, and S. P. E. Keeley, 2008: Sensitivity of Southern Hemisphere climate to zonal asymmetry in ozone. *Geophysical Research Letters*, **35 (7)**, doi:10.1029/2007GL032698.

Dameris, M., T. Peter, U. Schmidt, and R. Zellner, 2007: Das Ozonloch und seine Ursachen. *Chemie in unserer Zeit*, **41 (3)**, 152–168, doi:10.1002/ciuz.200700418.

Dennison, F. W., A. J. McDonald, and O. Morgenstern, 2015: The effect of ozone depletion on the Southern Annular Mode and stratosphere-troposphere coupling. *Journal of Geophysical Research: Atmospheres*, **120 (13)**, 6305–6312, doi:10.1002/2014JD023009.

Dhomse, S. S., D. Kinnison, M. P. Chipperfield, R. J. Salawitch, I. Cionni, M. I. Hegglin, N. L. Abraham, H. Akiyoshi, A. T. Archibald, E. M. Bednarz, S. Bekki, P. Braesicke, N. Butchart, M. Dameris, M. Deushi, S. Frith, S. C. Hardiman, B. Hassler, L. W. Horowitz, R.-M. Hu, P. Jöckel, B. Josse, O. Kirner, S. Kremser, U. Langematz, J. Lewis, M. Marchand, M. Lin, E. Mancini, V. Marécal, M. Michou, O. Morgenstern, O&apos, F. M. Connor, L. Oman, G. Pitari, D. A. Plummer, J. A. Pyle, L. E. Revell, E. Rozanov, R. Schofield, A. Stenke, K. Stone, K. Sudo, S. Tilmes, D. Visioni, Y. Yamashita, and G. Zeng, 2018: Estimates of ozone return dates from Chemistry-Climate Model Initiative simulations. *Atmospheric Chemistry and Physics*, **18 (11)**, 8409–8438, doi:10.5194/acp-18-8409-2018.

Dipankar, A., B. Stevens, R. Heinze, C. Moseley, G. Zängl, M. Giorgetta, and S. Brdar, 2015: Large eddy simulation using the general circulation model ICON. *Journal of Advances in Modeling Earth Systems*, **7 (3)**, 963–986, doi:10.1002/2015MS000431.

Efron, B. and G. Gong, 1983: A Leisurely Look at the Bootstrap, the Jackknife, and Cross-Validation. *The American Statistician*, **37 (1)**, 36, doi:10.2307/2685844.

Ehhalt, D., M. Prather, F. Dentener, R. Derwent, E. Dlugokencky, E. A. Holland, I. Isaksen, J. Katima, V. Kirchhoff, P. Matson, et al., 2001: Atmospheric chemistry and greenhouse gases. *Climate Change 2001: impacts, adaptation and vulnerability*, Cambridge University Press, 241–287.

Eyring, V., N. Butchart, D. W. Waugh, H. Akiyoshi, J. Austin, S. Bekki, G. E. Bodeker, B. A. Boville, C. Brühl, M. P. Chipperfield, E. Cordero, M. Dameris, M. Deushi, V. E. Fioletov, S. M. Frith, R. R. Garcia, A. Gettelman, M. A. Giorgetta, V. Grewe, L. Jourdain, D. E. Kinnison, E. Mancini, E. Manzini, M. Marchand, D. R. Marsh, T. Nagashima, P. A. Newman, J. E. Nielsen, S. Pawson, G. Pitari, D. A. Plummer, E. Rozanov, M. Schraner, T. G. Shepherd, K. Shibata, R. S. Stolarski, H. Struthers, W. Tian, and M. Yoshiki, 2006: Assessment of temperature, trace species, and ozone in chemistry-climate model simulations of the recent past. *Journal of Geophysical Research*, **111 (D22)**, doi:10.1029/2006JD007327.

Farman, J. C., B. G. Gardiner, and J. D. Shanklin, 1985: Large losses of total ozone in Antarctica reveal seasonal ClO x /NO x interaction. *Nature*, **315 (6016)**, 207–210, doi:10.1038/315207a0.

Feng, W., M. P. Chipperfield, H. K. Roscoe, J. J. Remedios, A. M. Waterfall, G. P. Stiller, N. Glatthor, M. Höpfner, and D.-Y. Wang, 2005: Three-Dimensional Model Study of the Antarctic Ozone Hole in 2002 and Comparison with 2000. *Journal of the Atmospheric Sciences*, **62 (3)**, 822–837, doi:10.1175/JAS-3335.1.

Flynn, L., C. Long, X. Wu, R. Evans, C. T. Beck, I. Petropavlovskikh, G. McConville, W. Yu, Z. Zhang, J. Niu, E. Beach, Y. Hao, C. Pan, B. Sen, M. Novicki, S. Zhou, and C. Seftor, 2014: Performance of the Ozone Mapping and Profiler Suite (OMPS) products. *Journal of Geophysical Research: Atmospheres*, **119 (10)**, 6181–6195, doi:10.1002/2013JD020467.

Fogt, R. L. and G. J. Marshall, 2020: The Southern Annular Mode: Variability, trends, and climate impacts across the Southern Hemisphere. *Wiley Interdisciplinary Reviews: Climate Change*, **11 (4)**, e652, doi:10.1002/wcc.652.

Fogt, R. L., J. Perlwitz, A. J. Monaghan, D. H. Bromwich, J. M. Jones, and G. J. Marshall, 2009: Historical SAM Variability. Part II: Twentieth-Century Variability and Trends from Reconstructions, Observations, and the IPCC AR4 Models. *Journal of Climate*, **22 (20)**, 5346–5365, doi:10.1175/2009JCLI2786.1.

Gassmann, A. and H.-J. Herzog, 2008: Towards a consistent numerical compressible non-hydrostatic model using generalized Hamiltonian tools. *Quarterly Journal of the Royal Meteorological Society*, **134 (635)**, 1597–1613, doi:10.1002/qj.297.

Gelaro, R., W. McCarty, M. J. Suárez, R. Todling, A. Molod, L. Takacs, C. Randles, A. Darmenov, M. G. Bosilovich, R. Reichle, K. Wargan, L. Coy, R. Cullather, C. Draper, S. Akella, V. Buchard, A. Conaty, A. da Silva, W. Gu, G.-K. Kim, R. Koster, R. Lucchesi, D. Merkova, J. E. Nielsen, G. Partyka, S. Pawson, W. Putman, M. Rienecker, S. D. Schubert, M. Sienkiewicz, and B. Zhao, 2017: The Modern-Era Retrospective Analysis for Research and Applications, Version 2 (MERRA-2). *Journal of Climate*, **Volume 30 (Iss 13)**, 5419–5454, doi:10.1175/JCLI-D-16-0758.1.

Gerber, E. P., L. M. Polvani, and D. Ancukiewicz, 2008a: Annular mode time scales in the Intergovernmental Panel on Climate Change Fourth Assessment Report models. *Geophysical Research Letters*, **35 (22)**, doi:10.1029/2008GL035712.

Gerber, E. P., S. Voronin, and L. M. Polvani, 2008b: Testing the Annular Mode Autocorrelation Time Scale in Simple Atmospheric General Circulation Models. *Monthly Weather Review*, **136 (4)**, 1523–1536, doi:10.1175/2007MWR2211.1.

Gerber, E. P., M. P. Baldwin, H. Akiyoshi, J. Austin, S. Bekki, P. Braesicke, N. Butchart, M. Chipperfield, M. Dameris, S. Dhomse, S. M. Frith, R. R. Garcia, H. Garny, A. Gettelman, S. C. Hardiman, A. Karpechko, M. Marchand, O. Morgenstern, J. E. Nielsen, S. Pawson, T. Peter, D. A. Plummer, J. A. Pyle, E. Rozanov, J. F. Scinocca, T. G. Shepherd, and D. Smale, 2010: Stratosphere-troposphere coupling and annular mode variability in chemistry-climate models. *Journal of Geophysical Research*, **115**, doi:10.1029/2009JD013770.

Gillett, N. P., T. D. Kell, and P. D. Jones, 2006: Regional climate impacts of the Southern Annular Mode. *Geophysical Research Letters*, **33 (23)**, D12 106, doi:10.1029/2006GL027721.

Gillett, N. P., J. F. Scinocca, D. A. Plummer, and M. C. Reader, 2009: Sensitivity of climate to dynamically-consistent zonal asymmetries in ozone. *Geophysical Research Letters*, **36 (10)**, doi:10.1029/2009GL037246.

Gillett, N. P. and D. W. J. Thompson, 2003: Simulation of recent southern hemisphere climate change. *Science*, **302 (5643)**, 273–275, doi:10.1126/science.1087440.

Giorgetta, M. A., R. Brokopf, T. Crueger, M. Esch, S. Fiedler, J. Helmert, C. Hohenegger, L. Kornblueh, M. Köhler, E. Manzini, T. Mauritsen, C. Nam, T. Raddatz, S. Rast, D. Reinert, M. Sakradzija, H. Schmidt, R. Schneck, R. Schnur, L. Silvers, H. Wan,

G. Zängl, and B. Stevens, 2018: ICON–A, the Atmosphere Component of the ICON Earth System Model: I. Model Description. *Journal of Advances in Modeling Earth Systems*, **10 (7)**, 1613–1637, doi:10.1029/2017MS001242.

Grise, K. M., D. W. J. Thompson, and P. M. Forster, 2009: On the Role of Radiative Processes in Stratosphere–Troposphere Coupling. *Journal of Climate*, **22 (15)**, 4154–4161, doi:10.1175/2009JCLI2756.1.

Haase, S. and K. Matthes, 2019: The importance of interactive chemistry for stratosphere–troposphere coupling. *Atmospheric Chemistry and Physics*, **19 (5)**, 3417–3432, doi:10.5194/acp-19-3417-2019.

Hardiman, S. C., N. Butchart, F. M. O'Connor, and S. T. Rumbold, 2017: The Met Office HadGEM3-ES chemistry–climate model: evaluation of stratospheric dynamics and its impact on ozone. *Geoscientific Model Development*, **10 (3)**, 1209–1232, doi:10.5194/gmd-10-1209-2017.

Haynes, P. H., M. E. McIntyre, T. G. Shepherd, C. J. Marks, and K. P. Shine, 1991: On the "Downward Control" of Extratropical Diabatic Circulations by Eddy-Induced Mean Zonal Forces. *Journal of the Atmospheric Sciences*, **48 (4)**, 651–678, doi:10.1175/1520-0469(1991)048<0651:OTCOED>2.0.CO;2.

Hendon, H. H., D. W. J. Thompson, and M. C. Wheeler, 2007: Australian Rainfall and Surface Temperature Variations Associated with the Southern Hemisphere Annular Mode. *Journal of Climate*, **20 (11)**, 2452–2467, doi:10.1175/JCLI4134.1.

Hersbach, H., B. Bell, P. Berrisford, S. Hirahara, A. Horányi, J. Muñoz-Sabater, J. Nicolas, C. Peubey, R. Radu, D. Schepers, A. Simmons, C. Soci, S. Abdalla, X. Abellan, G. Balsamo, P. Bechtold, G. Biavati, J. Bidlot, M. Bonavita, G. Chiara, P. Dahlgren, D. Dee, M. Diamantakis, R. Dragani, J. Flemming, R. Forbes, M. Fuentes, A. Geer, L. Haimberger, S. Healy, R. J. Hogan, E. Hólm, M. Janisková, S. Keeley, P. Laloyaux, P. Lopez, C. Lupu, G. Radnoti, P. Rosnay, I. Rozum, F. Vamborg, S. Villaume, and J.-N. Thépaut, 2020: The ERA5 global reanalysis: Quarterly Journal of the Royal Meteorological Society, 146(730), 1999-2049. *Quarterly Journal of the Royal Meteorological Society*, **146 (730)**, 1999–2049, doi:10.1002/QJ.3803.

Holton, J. R., 2004: *An introduction to dynamic meteorology*, International geophysics series, Vol. 88. 4. ed., Elsevier Academic Press, Burlington MA.

Holz, A., J. Paritsis, I. A. Mundo, T. T. Veblen, T. Kitzberger, G. J. Williamson, E. Aráoz, C. Bustos-Schindler, M. E. González, H. R. Grau, and J. M. Quezada, 2017: Southern Annular Mode drives multicentury wildfire activity in southern South

America. *Proceedings of the National Academy of Sciences*, **114 (36)**, 9552–9557, doi:10.1073/pnas.1705168114.

Karpechko, A. Y., N. P. Gillett, L. J. Gray, and M. Dall'Amico, 2010: Influence of ozone recovery and greenhouse gas increases on Southern Hemisphere circulation. *Journal of Geophysical Research*, **115 (D22)**, 2896, doi:10.1029/2010JD014423.

Karpechko, A. Y., N. P. Gillett, G. J. Marshall, and A. A. Scaife, 2008: Stratospheric influence on circulation changes in the Southern Hemisphere troposphere in coupled climate models. *Geophysical Research Letters*, **35 (20)**, 2896, doi:10.1029/2008GL035354.

Keeble, J., P. Braesicke, N. L. Abraham, H. K. Roscoe, and J. A. Pyle, 2014: The impact of polar stratospheric ozone loss on Southern Hemisphere stratospheric circulation and climate. *Atmospheric Chemistry and Physics*, **14 (24)**, 13 705–13 717, doi:10.5194/acp-14-13705-2014.

Keeble, J., B. Hassler, A. Banerjee, R. Checa-Garcia, G. Chiodo, S. Davis, V. Eyring, P. T. Griffiths, O. Morgenstern, P. Nowack, G. Zeng, J. Zhang, G. Bodeker, D. Cugnet, G. Danabasoglu, M. Deushi, L. W. Horowitz, L. Li, M. Michou, M. J. Mills, P. Nabat, S. Park, and T. Wu, 2020: Evaluating stratospheric ozone and water vapor changes in CMIP6 models from 1850–2100. doi:10.5194/acp-2019-1202.

Kidston, J., A. A. Scaife, S. C. Hardiman, D. M. Mitchell, N. Butchart, M. P. Baldwin, and L. J. Gray, 2015: Stratospheric influence on tropospheric jet streams, storm tracks and surface weather. *Nature Geoscience*, **8 (6)**, 433–440, doi:10.1038/ngeo2424.

Kim, J. and T. Reichler, 2016: Quantifying the uncertainty of the annular mode time scale and the role of the stratosphere. *Climate Dynamics*, **47 (1-2)**, 637–649, doi:10.1007/s00382-015-2860-2.

Lean, J., G. Rottman, J. Harder, and G. Kopp, 2005: SORCE Contributions to New Understanding of Global Change and Solar Variability. **348**, 27–53, doi:10.1007/0-387-37625-9_3.

Leith, C. E., 1975: Climate Response and Fluctuation Dissipation. *Journal of the Atmospheric Sciences*, **32 (10)**, 2022–2026, doi:10.1175/1520-0469(1975)032<2022:CRAFD>2.0.CO;2.

Leuenberger, D., M. Koller, O. Fuhrer, and C. Schär, 2010: A Generalization of the SLEVE Vertical Coordinate. *Monthly Weather Review*, **138 (9)**, 3683–3689, doi:10.1175/2010MWR3307.1.

Levelt, P. F., G. van den Oord, M. R. Dobber, A. Malkki, H. Visser, J. d. Vries, P. Stammes, J. Lundell, and H. Saari, 2006: The ozone monitoring instrument. *IEEE Transactions on Geoscience and Remote Sensing*, **44 (5)**, 1093–1101, doi:10.1109/TGRS.2006.872333.

Li, F., Y. V. Vikhliaev, P. A. Newman, S. Pawson, J. Perlwitz, D. W. Waugh, and A. R. Douglass, 2016: Impacts of Interactive Stratospheric Chemistry on Antarctic and Southern Ocean Climate Change in the Goddard Earth Observing System, Version 5 (GEOS-5). *Journal of Climate*, **29 (9)**, 3199–3218, doi:10.1175/JCLI-D-15-0572.1.

Livezey, R. E. and W. Y. Chen, 1983: Statistical Field Significance and its Determination by Monte Carlo Techniques. *Monthly Weather Review*, **111 (1)**, 46–59, doi:10.1175/1520-0493(1983)111<0046:SFSAID>2.0.CO;2.

Manatsa, D., Y. Morioka, S. K. Behera, T. Yamagata, and C. H. Matarira, 2013: Link between Antarctic ozone depletion and summer warming over southern Africa. *Nature Geoscience*, **6 (11)**, 934–939, doi:10.1038/ngeo1968.

Marshall, G. J., 2007: Half-century seasonal relationships between the Southern Annular mode and Antarctic temperatures. *International Journal of Climatology*, **27 (3)**, 373–383, doi:10.1002/joc.1407.

Marshall, G. J., A. Orr, N. P. M. van Lipzig, and J. C. King, 2006: The Impact of a Changing Southern Hemisphere Annular Mode on Antarctic Peninsula Summer Temperatures. *Journal of Climate*, **19 (20)**, 5388–5404, doi:10.1175/JCLI3844.1.

Masui, T., K. Matsumoto, Y. Hijioka, T. Kinoshita, T. Nozawa, S. Ishiwatari, E. Kato, P. R. Shukla, Y. Yamagata, and M. Kainuma, 2011: An emission pathway for stabilization at 6 Wm^{-2} radiative forcing. *Climatic Change*, **109 (1-2)**, 59–76, doi:10.1007/s10584-011-0150-5.

Maycock, A. C., W. J. Randel, A. K. Steiner, A. Y. Karpechko, J. Christy, R. Saunders, D. W. J. Thompson, C.-Z. Zou, A. Chrysanthou, N. Luke Abraham, H. Akiyoshi, A. T. Archibald, N. Butchart, M. Chipperfield, M. Dameris, M. Deushi, S. Dhomse, G. Di Genova, P. Jöckel, D. E. Kinnison, O. Kirner, F. Ladstädter, M. Michou, O. Morgenstern, F. O'Connor, L. Oman, G. Pitari, D. A. Plummer, L. E. Revell, E. Rozanov, A. Stenke, D. Visioni, Y. Yamashita, and G. Zeng, 2018: Revisiting the Mystery of Recent Stratospheric Temperature Trends. *Geophysical Research Letters*, **45 (18)**, 9919–9933, doi:10.1029/2018GL078035.

McElroy, M. B., R. J. Salawitch, S. C. Wofsy, and J. A. Logan, 1986: Reductions of Antarctic ozone due to synergistic interactions of chlorine and bromine. *Nature*, **321 (6072)**, 759–762, doi:10.1038/321759a0.

McLandress, C., T. G. Shepherd, J. F. Scinocca, D. A. Plummer, M. Sigmond, A. I. Jonsson, and M. C. Reader, 2011: Separating the Dynamical Effects of Climate Change and Ozone Depletion. Part II: Southern Hemisphere Troposphere. *Journal of Climate*, **24 (6)**, 1850–1868, doi:10.1175/2010JCLI3958.1.

McLinden, C. A., S. C. Olsen, B. Hannegan, O. Wild, M. J. Prather, and J. Sundet, 2000: Stratospheric ozone in 3-D models: A simple chemistry and the cross-tropopause flux. *Journal of Geophysical Research: Atmospheres*, **105 (D11)**, 14 653–14 665, doi:10.1029/2000JD900124.

McPeters, R. D., P. K. Bhartia, A. J. Krueger, J. R. Herman, C. G. Wellemeyer, C. J. Seftor, G. Jaross, O. Torres, L. Moy, G. Labow, et al., 1998: Earth probe total ozone mapping spectrometer (TOMS) data products user's guide, Ref. *IEEE Trans. Geosci*.

Miller, R. L., G. A. Schmidt, and D. T. Shindell, 2006: Forced annular variations in the 20th century Intergovernmental Panel on Climate Change Fourth Assessment Report models. *Journal of Geophysical Research*, **111 (D18)**, 1657, doi:10.1029/2005JD006323.

Mohanakumar, K., 2008: *Stratosphere troposphere interactions: An introduction*. Springer, New York.

MOHC (Met Office Hadley Centre) Data, 2020-02-14: Part of the IGAC/SPARC Chemistry-Climate Model Initiative Phase-1 (CCMI-1) Project Database: NCAS British Atmospheric Data Centre. `https://catalogue.ceda.ac.uk/uuid/320ef51584b14993ac04a4bdeef4a719`.

Molina, L. T. and M. J. Molina, 1987: Production of chlorine oxide (Cl2O2) from the self-reaction of the chlorine oxide (ClO) radical. *The Journal of Physical Chemistry*, **91 (2)**, 433–436, doi:10.1021/j100286a035.

Molina, M. J. and F. S. Rowland, 1974: Stratospheric sink for chlorofluoromethanes: Chlorine atom-catalysed destruction of ozone. *Nature*, **249 (5460)**, 810–812, doi:10.1038/249810a0.

Montreal Protocol, 1987: Montreal protocol on substances that deplete the ozone layer. `http://ozone.unep.org/en/treaties-and-decisions/montreal-protocol-substances-deplete-ozone-layer`.

Morgenstern, O., P. Braesicke, F. M. O'Connor, A. C. Bushell, C. E. Johnson, S. M. Osprey, and J. A. Pyle, 2009: Evaluation of the new UKCA climate-composition model – Part 1: The stratosphere. *Geoscientific Model Development*, **2 (1)**, 43–57, doi:10.5194/gmd-2-43-2009.

Müller, R., 2012: *Stratospheric ozone depletion and climate change*. RSC Publ, Cambridge, doi:10.1039/9781849733182.

Navarra, A. and V. Simoncini, 2010: *A Guide to Empirical Orthogonal Functions for Climate Data Analysis*. Springer Netherlands.

Neely, R. R., D. R. Marsh, K. L. Smith, S. M. Davis, and L. M. Polvani, 2014: Biases in southern hemisphere climate trends induced by coarsely specifying the temporal resolution of stratospheric ozone. *Geophysical Research Letters*, **41 (23)**, 8602–8610, doi:10.1002/2014GL061627.

Nowack, P. J., N. L. Abraham, A. C. Maycock, P. Braesicke, J. M. Gregory, M. M. Joshi, A. Osprey, and J. A. Pyle, 2015: A large ozone-circulation feedback and its implications for global warming assessments. *Nature climate change*, **5 (January)**, 41–45, doi:10.1038/nclimate2451.

Osprey, S. M., L. J. Gray, S. C. Hardiman, N. Butchart, A. C. Bushell, and T. J. Hinton, 2010: The Climatology of the Middle Atmosphere in a Vertically Extended Version of the Met Office's Climate Model. Part II: Variability. *Journal of the Atmospheric Sciences*, **67 (11)**, 3637–3651, doi:10.1175/2010JAS3338.1.

Perlwitz, J., S. Pawson, R. L. Fogt, J. E. Nielsen, and W. D. Neff, 2008: Impact of stratospheric ozone hole recovery on Antarctic climate. *Geophysical Research Letters*, **35 (8)**, 2896, doi:10.1029/2008GL033317.

Polvani, L. M., M. Previdi, and C. Deser, 2011a: Large cancellation, due to ozone recovery, of future Southern Hemisphere atmospheric circulation trends. *Geophysical Research Letters*, **38 (4)**, doi:10.1029/2011GL046712.

Polvani, L. M., D. W. Waugh, G. J. P. Correa, and S.-W. Son, 2011b: Stratospheric Ozone Depletion: The Main Driver of Twentieth-Century Atmospheric Circulation Changes in the Southern Hemisphere. *Journal of Climate*, **24 (3)**, 795–812, doi:10.1175/2010JCLI3772.1.

Previdi, M. and L. M. Polvani, 2014: Climate system response to stratospheric ozone depletion and recovery. *Quarterly Journal of the Royal Meteorological Society*, **140 (685)**, 2401–2419, doi:10.1002/qj.2330.

Randel, W. J. and F. Wu, 1999: Cooling of the Arctic and Antarctic Polar Stratospheres due to Ozone Depletion. *Journal of Climate*, **12 (5)**, 1467–1479, doi:10.1175/1520-0442(1999)012<1467:COTAAA>2.0.CO;2.

Renwick, J. and D. Thompson, 2006: The Southern Annular Mode and New Zealand climate. *Water and Atmosphere*, **14**, 24–25.

Rieger, D., M. Bangert, I. Bischoff-Gauss, J. Förstner, K. Lundgren, D. Reinert, J. Schröter, H. Vogel, G. Zängl, R. Ruhnke, and B. Vogel, 2015: ICON–ART 1.0 – a new online-coupled model system from the global to regional scale. *Geoscientific Model Development*, **8 (6)**, 1659–1676, doi:10.5194/gmd-8-1659-2015.

Rienecker, M. M., M. J. Suarez, R. Todling, J. Bacmeister, L. Takacs, H.-C. Liu, W. Gu, M. Sienkiewicz, Koster, R. D. Koster, R. Gelaro, I. Stajner, and J. E. Nielsen, 2008: The GEOS-5 Data Assimilation System— Documentation of Versions 5.0.1, 5.1.0, and 5.2.0. *Technical Report Series on Global Modeling and Data Assimilation, Volume 27*, `https://gmao.gsfc.nasa.gov/pubs/docs/Rienecker369.pdf`.

Rienecker, M. M., M. J. Suarez, R. Gelaro, R. Todling, J. Bacmeister, E. Liu, M. G. Bosilovich, S. D. Schubert, L. Takacs, G.-K. Kim, S. Bloom, J. Chen, D. Collins, A. Conaty, A. da Silva, W. Gu, J. Joiner, R. D. Koster, R. Lucchesi, A. Molod, T. Owens, S. Pawson, P. Pegion, C. R. Redder, R. Reichle, F. R. Robertson, A. G. Ruddick, M. Sienkiewicz, and J. Woollen, 2011: MERRA: NASA's Modern-Era Retrospective Analysis for Research and Applications. *Journal of Climate*, **24 (14)**, 3624–3648, doi:10.1175/JCLI-D-11-00015.1.

Ring, M. J. and R. A. Plumb, 2008: The Response of a Simplified GCM to Axisymmetric Forcings: Applicability of the Fluctuation–Dissipation Theorem. *Journal of the Atmospheric Sciences*, **65 (12)**, 3880–3898, doi:10.1175/2008JAS2773.1.

Sassi, F., B. A. Boville, D. Kinnison, and R. R. Garcia, 2005: The effects of interactive ozone chemistry on simulations of the middle atmosphere. *Geophysical Research Letters*, **32 (7)**, doi:10.1029/2004GL022131.

Schär, C., D. Leuenberger, O. Fuhrer, D. Lüthi, and C. Girard, 2002: A New Terrain-Following Vertical Coordinate Formulation for Atmospheric Prediction Models. *Monthly Weather Review*, **130 (10)**, 2459–2480, doi:10.1175/1520-0493(2002)130<2459:ANTFVC>2.0.CO;2.

Schröter, J., D. Rieger, C. Stassen, H. Vogel, M. Weimer, S. Werchner, J. Förstner, F. Prill, D. Reinert, G. Zängl, M. Giorgetta, R. Ruhnke, B. Vogel, and P. Braesicke, 2018: ICON-ART 2.1: a flexible tracer framework and its application for composition studies in numerical weather forecasting and climate simulations. *Geoscientific Model Development*, **11 (10)**, 4043–4068, doi:10.5194/gmd-11-4043-2018.

Seviour, W. J. M., D. W. Waugh, L. M. Polvani, G. J. P. Correa, and C. I. Garfinkel, 2017: Robustness of the Simulated Tropospheric Response to Ozone Depletion. *Journal of Climate*, **30 (7)**, 2577–2585, doi:10.1175/JCLI-D-16-0817.1.

Shindell, D. T., 2004: Southern Hemisphere climate response to ozone changes and greenhouse gas increases. *Geophysical Research Letters*, **31 (18)**, 1, doi:10.1029/2004GL020724.

Simpson, I. R., P. Hitchcock, T. G. Shepherd, and J. F. Scinocca, 2011: Stratospheric variability and tropospheric annular-mode timescales. *Geophysical Research Letters*, **38 (20)**, doi:10.1029/2011GL049304.

Sinnhuber, B.-M., M. Weber, A. Amankwah, and J. P. Burrows, 2003: Total ozone during the unusual Antarctic winter of 2002. *Geophysical Research Letters*, **30 (11)**, 151, doi:10.1029/2002GL016798.

Solomon, S., 1999: Stratospheric ozone depletion: A review of concepts and history. *Reviews of Geophysics*, **37 (3)**, 275–316, doi:10.1029/1999RG900008.

Solomon, S., R. R. Garcia, F. S. Rowland, and D. J. Wuebbles, 1986: On the depletion of Antarctic ozone. *Nature*, **321 (6072)**, 755–758, doi:10.1038/321755a0.

Son, S.-W., N. F. Tandon, L. M. Polvani, and D. W. Waugh, 2009: Ozone hole and Southern Hemisphere climate change. *Geophysical Research Letters*, **36 (15)**, doi:10.1029/2009GL038671.

Son, S.-W., L. M. Polvani, D. W. Waugh, H. Akiyoshi, R. Garcia, D. Kinnison, S. Pawson, E. Rozanov, T. G. Shepherd, and K. Shibata, 2008: The impact of stratospheric ozone recovery on the Southern Hemisphere westerly jet. *Science (New York, N.Y.)*, **320 (5882)**, 1486–1489, doi:10.1126/science.1155939.

Son, S.-W., E. P. Gerber, J. Perlwitz, L. M. Polvani, N. P. Gillett, K.-H. Seo, V. Eyring, T. G. Shepherd, D. Waugh, H. Akiyoshi, J. Austin, A. Baumgaertner, S. Bekki, P. Braesicke, C. Brühl, N. Butchart, M. P. Chipperfield, D. Cugnet, M. Dameris, S. Dhomse, S. Frith, H. Garny, R. Garcia, S. C. Hardiman, P. Jöckel, J. F. Lamarque, E. Mancini, M. Marchand, M. Michou, T. Nakamura, O. Morgenstern, G. Pitari, D. A. Plummer, J. Pyle, E. Rozanov, J. F. Scinocca, K. Shibata, D. Smale, H. Teyssèdre, W. Tian, and Y. Yamashita, 2010: Impact of stratospheric ozone on Southern Hemisphere circulation change: A multimodel assessment. *Journal of Geophysical Research*, **115 (7)**, D03 103, doi:10.1029/2010JD014271.

Son, S.-W., B.-R. Han, C. I. Garfinkel, S.-Y. Kim, R. Park, N. L. Abraham, H. Akiyoshi, A. T. Archibald, N. Butchart, M. P. Chipperfield, M. Dameris, M. Deushi, S. S. Dhomse, S. C. Hardiman, P. Jöckel, D. Kinnison, M. Michou, O. Morgenstern, F. M. O'Connor, L. D. Oman, D. A. Plummer, A. Pozzer, L. E. Revell, E. Rozanov, A. Stenke, K. Stone, S. Tilmes, Y. Yamashita, and G. Zeng, 2018: Tropospheric jet response

to Antarctic ozone depletion: An update with Chemistry-Climate Model Initiative (CCMI) models. *Environmental Research Letters*, **13 (5)**, 054 024, doi:10.1088/1748-9326/aabf21.

Song, Y. and W. A. Robinson, 2004: Dynamical Mechanisms for Stratospheric Influences on the Troposphere. *Journal of the Atmospheric Sciences*, **61 (14)**, 1711–1725, doi:10.1175/1520-0469(2004)061<1711:DMFSIO>2.0.CO;2.

Staniforth, A. and J. Thuburn, 2012: Horizontal grids for global weather and climate prediction models: a review. *Quarterly Journal of the Royal Meteorological Society*, **138 (662)**, 1–26, doi:10.1002/qj.958.

Staten, P. W., J. J. Rutz, T. Reichler, and J. Lu, 2012: Breaking down the tropospheric circulation response by forcing. *Climate Dynamics*, **39 (9)**, 2361–2375, doi:10.1007/s00382-011-1267-y.

Stenchikov, G., T. L. Delworth, V. Ramaswamy, R. J. Stouffer, A. Wittenberg, and F. Zeng, 2009: Volcanic signals in oceans. *Journal of Geophysical Research: Atmospheres*, **114 (D16)**, doi:10.1029/2008JD011673.

Stenchikov, G., K. Hamilton, A. Robock, V. Ramaswamy, and M. D. Schwarzkopf, 2004: Arctic oscillation response to the 1991 Pinatubo eruption in the SKYHI general circulation model with a realistic quasi–biennial oscillation. *Journal of Geophysical Research: Atmospheres*, **109 (D3)**, doi:10.1029/2003JD003699.

Stenchikov, G. L., I. Kirchner, A. Robock, H.-F. Graf, J. C. Antuña, R. G. Grainger, A. Lambert, and L. Thomason, 1998: Radiative forcing from the 1991 Mount Pinatubo volcanic eruption. *Journal of Geophysical Research: Atmospheres*, **103 (D12)**, 13 837–13 857, doi:10.1029/98JD00693.

Stevens, B., S. Fiedler, S. Kinne, K. Peters, S. Rast, J. Müsse, S. J. Smith, and T. Mauritsen, 2017: MACv2-SP: a parameterization of anthropogenic aerosol optical properties and an associated Twomey effect for use in CMIP6. *Geoscientific Model Development*, **10 (1)**, 433–452, doi:10.5194/gmd-10-433-2017.

Stone, K. A., O. Morgenstern, D. J. Karoly, A. R. Klekociuk, W. J. French, N. L. Abraham, and R. Schofield, 2016: Evaluation of the ACCESS – chemistry–climate model for the Southern Hemisphere. *Atmospheric Chemistry and Physics*, **16 (4)**, 2401–2415, doi:10.5194/acp-16-2401-2016.

Student, 1908: The Probable Error of a Mean. *Biometrika*, **6 (1)**, 1, doi:10.2307/2331554.

Taylor, K. E., D. Williamson, and F. W. Zwiers, 2000: AMIP II Sea Surface Temperature and Sea Ice Concentration Boundary Conditions. *PCMDI Rep.*, **6**.

Thompson, D. W. J., M. P. Baldwin, and S. Solomon, 2005: Stratosphere–Troposphere Coupling in the Southern Hemisphere. *Journal of the Atmospheric Sciences*, **62 (3)**, 708–715, doi:10.1175/JAS-3321.1.

Thompson, D. W. J. and S. Solomon, 2002: Interpretation of recent Southern Hemisphere climate change. *Science (New York, N.Y.)*, **296 (5569)**, 895–899, doi:10.1126/science.1069270.

Thompson, D. W. J., S. Solomon, P. J. Kushner, M. H. England, K. M. Grise, and D. J. Karoly, 2011: Signatures of the Antarctic ozone hole in Southern Hemisphere surface climate change. *Nature Geoscience*, **4 (11)**, 741–749, doi:10.1038/ngeo1296.

Thompson, D. W. J. and J. M. Wallace, 2000: Annular Modes in the Extratropical Circulation. Part I: Month-to-Month Variability*. *Journal of Climate*, **13 (5)**, 1000–1016, doi:10.1175/1520-0442(2000)013<1000:AMITEC>2.0.CO;2.

Tomita, H., M. Tsugawa, M. Satoh, and K. Goto, 2001: Shallow Water Model on a Modified Icosahedral Geodesic Grid by Using Spring Dynamics. *Journal of Computational Physics*, **174 (2)**, 579–613, doi:10.1006/jcph.2001.6897.

Tritscher, I., M. C. Pitts, L. R. Poole, S. P. Alexander, F. Cairo, M. P. Chipperfield, J.-U. Grooß, M. Höpfner, A. Lambert, B. P. Luo, S. Molleker, A. Orr, R. Salawitch, M. Snels, R. Spang, W. Woiwode, and T. Peter, 2021: Polar Stratospheric Clouds Satellite Observations, Processes, and Role in Ozone Depletion. *Reviews of Geophysics*, doi:10.1029/2020RG000702.

Turner, J., S. R. Colwell, G. J. Marshall, T. A. Lachlan-Cope, A. M. Carleton, P. D. Jones, V. Lagun, P. A. Reid, and S. Iagovkina, 2005: Antarctic climate change during the last 50 years. *International Journal of Climatology*, **25 (3)**, 279–294, doi:10.1002/joc.1130.

van der Leun, J. C., X. Tang, and M. Tevini, 1998: *Environmental effects of ozone depletion: 1998 Assessment*. `http://cedadocs.ceda.ac.uk/id/eprint/984`.

Waugh, D. W., L. Oman, P. A. Newman, R. S. Stolarski, S. Pawson, J. E. Nielsen, and J. Perlwitz, 2009: Effect of zonal asymmetries in stratospheric ozone on simulated Southern Hemisphere climate trends. *Geophysical Research Letters*, **36 (18)**, doi:10.1029/2009GL040419.

Waugh, D. W., W. J. Randel, S. Pawson, P. A. Newman, and E. R. Nash, 1999: Persistence of the lower stratospheric polar vortices. *Journal of Geophysical Research: Atmospheres*, **104 (D22)**, 27 191–27 201, doi:10.1029/1999JD900795.

Weimer, M., J. Schröter, J. Eckstein, K. Deetz, M. Neumaier, G. Fischbeck, L. Hu, D. B. Millet, D. Rieger, H. Vogel, B. Vogel, T. Reddmann, O. Kirner, R. Ruhnke, and P. Braesicke, 2017: An emission module for ICON-ART 2.0: implementation and simulations of acetone. *Geoscientific Model Development*, **10 (6)**, 2471–2494, doi:10.5194/gmd-10-2471-2017.

Wilks, D. S., 2006: *Statistical methods in the atmospheric sciences*, International geophysics series, Vol. 91. 2. ed., Academic Press, Amsterdam and Boston.

Wilks, D. S., 2016: "The Stippling Shows Statistically Significant Grid Points": How Research Results are Routinely Overstated and Overinterpreted, and What to Do about It. *Bulletin of the American Meteorological Society*, **97 (12)**, 2263–2273, doi:10.1175/BAMS-D-15-00267.1.

WOUDC Ozonesonde Monitoring Community, World Meteorological Organization-Global Atmosphere Watch Program, and World Ozone And Ultraviolet Radiation Data Centre, 2015: Ozonesonde. World Ozone and Ultraviolet Radiation Data Centre (WOUDC), doi:10.14287/10000008.

Yin, J. H., 2005: A consistent poleward shift of the storm tracks in simulations of 21st century climate. *Geophysical Research Letters*, **32 (18)**, doi:10.1029/2005GL023684.

Young, P. J., A. T. Archibald, K. W. Bowman, J.-F. Lamarque, V. Naik, D. S. Stevenson, S. Tilmes, A. Voulgarakis, O. Wild, D. Bergmann, P. Cameron-Smith, I. Cionni, W. J. Collins, S. B. Dalsøren, R. M. Doherty, V. Eyring, G. Faluvegi, L. W. Horowitz, B. Josse, Y. H. Lee, I. A. MacKenzie, T. Nagashima, D. A. Plummer, M. Righi, S. T. Rumbold, R. B. Skeie, D. T. Shindell, S. A. Strode, K. Sudo, S. Szopa, and G. Zeng, 2013: Pre-industrial to end 21st century projections of tropospheric ozone from the Atmospheric Chemistry and Climate Model Intercomparison Project (ACCMIP). *Atmospheric Chemistry and Physics*, **13 (4)**, 2063–2090, doi:10.5194/acp-13-2063-2013.

Zängl, G., D. Reinert, P. Rípodas, and M. Baldauf, 2015: The ICON (ICOsahedral Non-hydrostatic) modelling framework of DWD and MPI-M: Description of the non-hydrostatic dynamical core. *Quarterly Journal of the Royal Meteorological Society*, **141 (687)**, 563–579, doi:10.1002/qj.2378.

List of Abbreviations

ART	Aerosols and Reactive Trace gases
ACCESS	Australian Community Climate and Earth System Simulator
BS	Bodeker Scientific
CCM	Chemistry-Climate Model
CFC	Chlorofluorocarbon
DJF	December - February
EOF	Empirical Orthogonal Function
ERA5	European Reanalysis, Version 5
FDR	False Discovery Rate
GEOS-FP	Goddard Earth Observing System - Forward Processing
GHG	Greenhouse Gas
HadGEM	Hadley Centre Global Environment Model
IFS	Integrated Forecasting System
ICON	Icosahedral Non-hydrostatic modeling framework
JJA	June - August
Linoz	Linearized Ozone
MAM	March - May
MERRA	Modern-Era Retrospective analysis for Research and Applications
MERRA2	Modern-Era Retrospective analysis for Research and Applications, Version 2
NASA	National Aeronautics and Space Administration

NAT	Nitric Acid Trihydrate
NIWA	National Institute of Water and Atmospheric Research
noPOC	no Polar Ozone Chemistry
ODS	Ozone Depleting Substance
OMI	Ozone Monitoring Instrument
OMPS	Ozone Mapping and Profiling Suite
PC	Principal Component
PCA	Principal Component Analysis
POC	Polar Ozone Chemistry
PSC	Polar Stratospheric Cloud
RCP	Representative Concentration Pathway
SAM	Southern Annular Mode
SH	Southern Hemisphere
SIC	Sea Ice Cover
SLEVE	Smooth Level Vertical
SON	September - November
SST	Sea Surface Temperature
SZA	Solar Zenith Angle
TCO	Total Column Ozone
TOMS	Total Ozone Mapping Spectrometer
UV	ultraviolet
WOUDC	World Ozone and Ultraviolet Radiation Data Centre

List of Figures

List of Tables

Acknowledgements

Mein besonderer Dank gilt zunächst Prof. Dr. Peter Braesicke für die freundliche Betreuung in den letzten Jahren, insbesondere für die vielen Treffen, hilfreiche Diskussionen, stets aufmunternde Worte und die Begutachtung dieser Dissertation.

Darüber hinaus danke ich PD Dr. Michael Höpfner für die Übernahme des Korreferats und die konstruktiven Anregungen in den letzten Wochen dieser Arbeit.

Des Weiteren möchte ich mich bei Dr. Jennifer Buchmüller für die Hilfe bei meinen Modellsimulationen und die zur Verfügung gestellten Python-Skripte bedanken, die mir den Einstieg in die Modellierung erheblich erleichtert haben.

Christopher Diekmann danke ich für die gemeinsame produktive und unterhaltsame Bürozeit mit dem richtigen Maß an Ablenkung und seine Hilfe bei Fragen zum Modell, Auswerteroutinen und organisatorischen Dingen.

Bei meinen Kollegen vom IMK, insbesondere von Ebene 4 und der Modellierungsabteilung, bedanke ich mich für die freundliche Arbeitsatmosphäre, ihre Hilfsbereitschaft, Anregungen zu meiner Arbeit und die schöne gemeinsame Zeit.

Dr. Sören Johansson, Dr. Farahnaz Khosrawi, Christian Scharun und Lukas Leufen danke ich für das Korrekturlesen meiner Arbeit.

Ich bedanke mich bei der Graduiertenschule für Klima und Umwelt (GRACE) für das Ermöglichen meines Auslandsaufenthaltes an der University of Melbourne.

I sincerely thank Dr. Robyn Schofield for hosting me at the University of Melbourne and for the productive discussions. I would also like to thank the colleagues at the School of Earth Sciences for coffee breaks and after work activities that made my stay a great experience.

Meiner Familie und meinen Freunden danke ich herzlichst für ihre Unterstützung, ihr Verständnis und die Ablenkung von der Arbeit. Größter Dank gilt dabei meinem Partner Jonas und meinen Eltern Harald und Anne, die immer ein offenes Ohr für mich hatten und mich auf vielfältige Weise unterstützt haben.